2009-05-28

Synthesis, Integration, and Characterization of Functional Inorganic Nanomaterials

Huanan Duan

Worcester Polytechnic Institute

Follow this and additional works at: https://digitalcommons.wpi.edu/etd-dissertations

Synthesis, Integration, and Characterization of Functional Inorganic Nanomaterials

by

Huanan Duan

A Dissertation

Submitted to the Faculty

of the

WORCESTER POLYTECHNIC INSTITUTE

in partial fulfillment of the requirements for the

Degree of Doctor of Philosophy

in

Materials Science and Engineering

————————————

May 2009

APPROVED:

————————————————————————

Dr. Jianyu Liang, Advisor

Assistant Professor of Mechanical Engineering

————————————————————————

Dr. Richard D. Sisson, Jr., George F. Fuller Professor, Director of Manufacturing and Materials Engineering

ABSTRACT

In the past decade nanomaterials have attracted the interest of scientists and engineers all over the world due to their unique properties. Through their devoted experimental efforts, limited advances have been made on the synthesis of nanomaterials, the integration of nanomaterials into the structures of larger scales, and the property study of nanomaterials to explore possible applications. Despite the huge amount of money, resources, and effort invested in nanomaterials, several challenges still remain as obstacles on the way towards the successful large scale use of nanomaterials to benefit human life and society. For example, the need for low-cost, robust, and highly productive manufacturing methods and the demand for efficient integration of nanomaterials with materials and devices of larger length scales are still left unmet.

The objective of this work was to utilize cost-efficient nanofabrication methods such as template-assisted fabrication, electrodeposition, and chemical vapor deposition to fabricate nanomaterials, integrate nanomaterials with larger structures to form a hierarchical composite, and explore the application of unique nanostructured electrode in lithium-ion batteries. Thus the thesis consists of three main parts: (1) fabrication of one-dimensional inorganic nanomaterials such as metal nanowires, metal nanorods, and carbon nanotubes with good control over shape and dimension; (2) synthesis of hierarchical carbon nanofibers on carbon microfibers and/or glass microfibers; and (3) development of nanostructured anodes to improve high-rate capability of lithium-ion batteries by adapting nanorod arrays as miniature current collectors.

ACKNOWLEDGEMENTS

TABLE OF CONTENTS

CHAPTER I: INTRODUCTION

Now more than ever, nanostructured materials have attracted tremendous interest from scientists and engineers all over the globe. Nanostructured materials exhibit peculiar and interesting properties superior to their bulk counterparts and have the potential to revolutionize many areas of research. As a result, extensive research efforts have been dedicated to studying various aspects of nanomaterials through numerical simulations and experiments.

Compared to well-developed disciplines, nanotechnology is in its infancy. Most of the current experimental work of nanomaterials is concentrated on the synthesis of nanostructures, the integration of nanomaterials into the structures of larger scales, and the property study of novel devices incorporating nanomaterials. This thesis focuses on using methods that are simple, cost-efficient, and easy to scale up to produce unique nanomaterials and design new devices to contribute to these three aspects.

Among the various nanomaterials, one-dimensional (1-D) nanostructures are of particular interest because of their potential applications in nanoscale electronic and optoelectronic devices. In particular, the fabrication of desired 1-D nanomaterials is still a major challenge for nanotechnologists. In the past decade, several major fabrication strategies such as lithography-based methods [1], self-assembly [2,3], vapor phase growth [4,5], solution based growth [5,6], template-assisted synthesis [5,6], and microcontact printing [6] have been explored and are under extensive and intensive study. Yet the journey to seek an easy, low-cost, precise, and highly productive preparation method continues.

After the preparation of nanomaterials, how to manipulate, transfer, and assemble them into functional devices and effectively integrate them with materials and devices of larger length scales remains another major obstacle. Scanning probe microscopy (SPM) techniques, for instance, have been used to manipulate atoms on metal surfaces and to fabricate nanopatterns on metal and semiconductor surfaces [1]. However, this process is extremely time-consuming, not cost efficient, and yields low throughput. An alternative route, instead of dealing with the as-prepared nanomaterials, is to directly grow nanostructures on larger scale

1

functional substrates to make a hierarchical structure. Then the manipulation of nanomaterials can be realized by handling the larger scaled substrate.

Nanomaterials and nanotechnology have the potential to revolutionize many traditional disciplines. They offer solutions to many critical, challenging, and long-existing problems. For instance, nanomaterials are expected to significantly improve the rate capability of lithium-ion (Li-ion) batteries. It is well accepted that the limitations in the rate capability of Li-ion batteries are mainly caused by slow solid-state diffusion of lithium ions in the electrode materials [7,8]. Nanostructured materials are considered as active candidates to tackle this problem because of the potential advantages they offer, such as: (i) short lithium ion transport length due to small particle sizes; (ii) fast surface reactions resulting from large electrode/electrolyte interface area; (iii) good accommodation of structure strains imposed by electrochemical reactions; and (iv) the possibility of operation in systems with low electronic conductivity due to short path lengths for electron transport. Thus, integration of nanomaterials might be the key to the development of the next generation of Li-ion batteries with high energy density and high power/current density.

The advantages of nanomaterials render them a very promising future. The synthesis, integration, and property study of nanomaterials constitute three crucial and interconnected aspects for the advancement of this field. The goal of this project is to explore these cutting-edge frontiers and contribute to the booming nanoscience and nanotechnology fields.

Research Objectives

The goals for this project include: (1) fabricating quality 1-D inorganic nanomaterials such as metal nanowires (NWs), metal nanorods (NRs), and carbon nanotubes (CNTs) with good control over the shape and dimension using an anodized aluminum oxide (AAO) template-assisted fabrication approach; (2) exploring the possibility of integration of nanomaterials to materials with larger dimension scale by synthesizing hierarchical structures of carbon nanofibers (CNFs) and carbon microfibers (CMFs) or glass microfibers (GMFs) and; (3) developing nanostructured electrodes that will improve high-rate capability of Li-ion batteries by adapting nanorod arrays as miniature current collectors and obtaining a better understanding of the role of how the nanorod current collector array affects the structure of

deposited active materials and the electrochemical performance of the as-prepared electrode.

In order to achieve these goals, the following technical objectives have been identified:

Objective 1. To synthesize and study the structures of the ordered metallic NW arrays and CNT arrays using the AAO template assisted fabrication approach;

Objective 2. To synthesize and study the hierarchical structures of CNFs and CMFs or GMFs;

Objective 3. To design and study the electrochemical properties of nanostructured electrodes (in collaboration with Yardney Technical Products, Inc.).

Research Plan

The research plan for this project focuses primarily on using cost-efficient methods such as electrodeposition and chemical vapor deposition (CVD) to study the synthesis, integration, and electrochemical properties of nanomaterials. This corresponds to the technical objectives and consists of three aspects: (1) synthesis of ordered metallic NW arrays and CNT arrays, (2) synthesis of the hierarchical structures of CNFs and CMFs or GMFs, and (3) the design and property study of nanostructured electrodes for Li-ion batteries.

The research plan is given in more detail in the following outline:

1. ***Synthesis of ordered metallic NW/NR arrays and CNT arrays***

   (1) A generic synthetic approach to fabricate Y-junction metal nanowires by AAO templates (submitted to *Electrochemistry Communication*) and (2) AAO-assisted Fabrication of metal NWs/NRs and CNTs (included in Appendix A).

   Linear and Y-junction metal NWs and CNTs were fabricated by AAO assisted electrodeposition and CVD, respectively. For metal NWs, different metal species such as cobalt and copper and different synthesis conditions were studied. CNTs were fabricated using catalyst-loaded AAO templates and catalyst-free AAO templates. A detailed microstructure and morphology study was presented.

2. ***Integration of nanomaterials***

   Synthetic Hierarchical nanostructures: Growth of Carbon Nanofibers on Microfibers by Chemical Vapor Deposition (submitted to *Materials Science and Technology B*)

CNFs were grown on the surface of CMFs and GMFs to fabricate hierarchical structures. A detailed morphology study was presented and the effect of synthesis conditions on the morphology of CNFs was discussed according to vapor-liquid-solid growth mechanisms.

3. ***Electrochemical property study of nanostructured electrodes for Li ion batteries***

(1) Novel growth morphology of cathodically electrodeposited Fe_3O_4 thin films (submitted to *Thin Solid Films*)

Fe_3O_4 thin films with different morphologies were fabricated on planar copper substrates by electrodeposition. The effect of synthesis parameters such as temperature, deposition duration, and electrolyte concentration on the resultant morphology were studied and discussed.

(2) Study of Fe_3O_4-based Cu Nanostructured Electrode for Li-ion Battery (published in *Journal of Power Sources*) and (3) Electrochemical preparation of nanostructured TiO_2 as anode material for Li ion batteries (published in *Proc.* MRS 2008, Boston, MA, 1127-T01-02 and included in Appendix B)

Nanostructured electrodes were fabricated using copper NR arrays as miniature current collectors. The active material of Fe_3O_4 and TiO_2 were loaded by electrodeposition. The electrochemical properties, namely charge/discharge capacity and rate capability, were studied and compared to the electrodes using planar copper foils as current collectors. The effect of the introduction of Cu NR arrays was discussed.

Thesis Organization

This thesis is divided into four chapters. This introductory chapter serves to familiarize the reader with the motivations and goals that have driven this project. Chapter II: Literature Review is a summary of relevant research which has been done in the aforementioned three areas. Chapter III: Publications compiles the journal articles that have either been published or submitted to peer-reviewed journals regarding the three aspects as outlined by the research plan. This thesis closes with conclusions and recommendations for future work in Chapter IV. Appendix A contains supporting information and some interesting experimental results of metal NWs/NRs and CNTs which either lay the foundation of the AAO template-assisted

method or may lead to interesting future research work. Included in Appendix B is a conference preceding paper detailing the fabrication of nanostrucutured TiO_2 electrodes for Li-ion batteries.

Reference

[1] Liu, G.; Xu, S.; Qian, Y. *Acc. Chem. Res*. **2000**, *33*, 457.

[2] Cheng, J. Y.; Ross, C. A.; Smith, H. I.; Thomas, E. L. *Adv. Mater.* **2006**, *18*, 2505.

[3] Ariga, K.; Hill, J. P.; Lee, M. V.; Vinu, A.; Charvet, R.; Acharya, S. Sci. Technol. Adv. Mater. **2008**, *9*, 014109.

[4] Weber, J.; Singhal, R.; Zekri, S.; Kumar, A. *Inter. Mater. Rev.* **2008**, *53*, 235.

[5] Wang, N.; Cai, Y.; Zhang, R.Q. *Mater. Sci. Eng. R.* **2008**, *60*, 1

[6] Gates, B. D.; Xu, Q.; Stewart, M.; Ryan, D.; Willson, C. G.; Whitesides, G. M. *Chem. Rev*. **2005**, *105*, 1171.

[7] Li, J.; Tang, Z.; Zhang, *Z. Electrochem. Commun*. **2005**, *7*, 62.

[8] Bruce, P. G. *Chem. Commun*. **1997**, *19*, 1817.

CHAPTER II LITERATURE REVIEW

In the -famous talk given at the annual meeting of the American Physical Society (APS) in 1959, "There's Plenty of Room at the Bottom," Nobel Prize laureate Richard Feynman envisioned the promise of nanotechnology. Two decades later, the development of the scanning tunneling microscope (STM) by IBM researchers gave scientists and engineers the ability not only to image atoms but also to manipulate atoms and clusters with a precision of a chemical bond. Also in the 1980s, Eric Drexler predicted a fantastic nanotechnology that was beyond Feynman's vision in several of his books. Later, fueled by breakthroughs such as the discovery of carbon nanotubes, production of self-assembled monolayers, and creation of quantum dots, together with advances in theory and modeling, nanotechnology took off.

With the fast advance in nanomaterials and nanotechnology, the debate over the future and the real impact of nanotechnology on human life and society grew heated. On one hand, nanotechnology has the potential to create many new materials and devices with wide-range applications in various fields such as medicine, electronics, and energy production [1,2]. On the other hand, nanotechnology raises many of the same issues as the introduction of a new technology, including concerns about the toxicity, environmental impact [3], their potential influence on global economics. Despite the ongoing debate, extensive research effort has been and will continue being dedicated to studying the synthesis and various properties, including thermal, electrical, mechanical, magnetic, and electrochemical properties, of nanomaterials

2.1 Nanomaterials

So what are nanomaterials? The word nano, which means "dwarf" in Greek, is just a fraction that indicated one billionth of a unit quantity. With major breakthroughs such as the Noble prize winning discovery of bucky balls and carbon fullerene structures, the first electron microscope images of carbon nanotubes, and the invention of inorganic fullerenes and anisotropic nanostructures, nanomaterials have been inspiring a great amount of interest. At present, realizing the importance of nanomaterials and heavy investment in nanotechnology by governments and private sectors has become a global trend. State of the

art technology centers with excellent processing and characterization and device fabrication facilities are being developed. The total amount of global funding invested in nanotechnology has increased by a factor of 9.45 from 1997 to 2005 and the United States shows a similar trend [4].

A large number of reviews and text books on the subjects of nanoscience and nanotechnology have been published, endorsing it as the leading science and technology of the 21st century [4-15]. The change of the dimension can lead to dramatic property change in nanomaterials. For example, when within the length range of quantum confinement the change in the dimensions in material result in changes of the total energy and the occupation of the outermost energy level [4]. Thus engineering the nanostructured materials could realize peculiar and fascinating physical and chemical properties superior to their bulk counterparts [16]. For example, quantum dots show Coulomb blockade [17-19] and strongly size-dependent optical and electrical properties [20], carbon nanotubes can have high electrical conductivity and mechanical strength [21-23], and thin polymer films can have glass-transition temperatures higher or lower than thick films [24,25].

Nanomaterials can be divided into zero-dimensional (nanocrystals, quantum dots), one-dimensional (1-D, nanowires, nanotubes), and two-dimensional nanomaterials (nanofilms, nanowalls). In particular, 1-D inorganic nanostructures which include nanotubes, nanorods, nanowires, nanobelts, and nanoribbons have become the focus of intensive research because they provide the ideal systems for investigating the dependence of electrical transport, optical and mechanical properties on size and dimension [26-29]. These structures have a potential broad impact on the research fields of medical sensing, drug delivery, microelectronics, bio-microelectromechanics (MEMS), communications, energy storage, and computation technology.

2.2 Nanofabrication of 1-D nanomaterials

Nanofabrication is the design and manufacture of materials with structural or chemical restrictions on the nanometer scale along one or more of the dimensions. It, together with characterization techniques, constitutes the cornerstone of the development of nanoscience

and nanotechnology. In the past couple of decades, developments in the semiconductor industry have offered tremendous advancements in microelectronic devices and information technologies. Microfabrication which makes devices on the micrometer scale by photolithography-based techniques has grown into its mature stage and large-scale commercial implementation of nanofabrication is sitting on the launch pad. According to the International Technology Roadmap of Semiconductors (ITRS), if the industry is to keep its pace on miniaturization by Moore's law, the gate size of a field emission transistor will be reduced to 25 nm by 2010 [30].

Strategies used to fabricate and assemble nanoscale materials and devices can be classified as "top-down" and "bottom-up". "Top-down" strategy begins with large homogeneous objects and seeks to shrink them down to the nanoscale. The "bottom-up" strategy uses the interactions between small components such as molecules or colloidal particles to arrange themselves into more complex and discrete nanoscale structures. The "bottom-up" synthesis method is considered a promising technique for addressing challenges related to the traditional "top-down" methods. Both top-down and bottom-up methods have been used to fabricate 1-D nanostructures. An exhaustive review of all the fabrication techniques is beyond the scope of this chapter. Here, recent development of several commonly used approaches, namely lithography based growth, vapor phase growth, solution based growth, and template-assisted synthesis is briefly reviewed.

2.2.1 Lithography based growth

Lithography is a collective term for related series of processes including resist coating, exposure, and development. The conventional lithographic approaches have achieved great success and help the microelectronics industry maintain a continuous growth by doubling the number of transistors on a single chip every 18 months [31]. Extensive literature exists on lithography based processes [32-35].
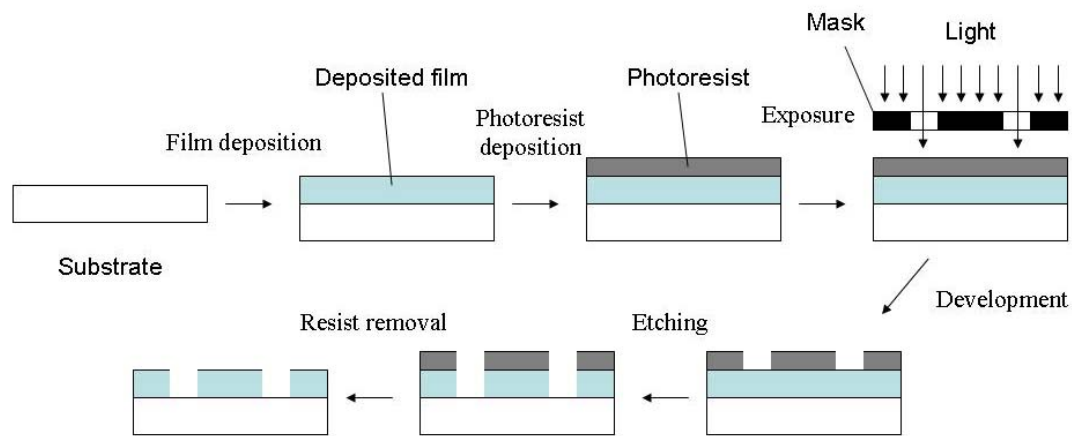
Fig. 2.1 The schematic of lithography

Fig. 2.1 depicts a schematic process of conventional lithography. The work piece, an unpatterned film or substrate, is first spin-coated with a uniform layer of resist dissolved in a certain organic liquid solvent. The resist thickness is typically a few thousand angstroms to a micron, depending on the spinning speed and the resist viscosity. A soft-bake of the resist is necessary to remove the resist solvent and promote adhesion. Selected areas of the resist are then exposed to a radiation source, often through a mask. Upon sufficient exposure, the polymer chains in the resist are either broken (positive resist), or become cross-linked (negative resist, poorer resolving power). The exposed resist often goes through a post-exposure bake to promote homogeneity, before developed to form a positive or negative image of the mask. By choosing the right developer, temperature and developing time, one can obtain straight, round-off or undercut depth profiles in the resist.

Pattern transfer can be realized in two general processes: from the resist to an unpatterned film by wet or dry etching; or post-deposition onto patterned resist by lift-off and/or electrodeposition. Wet etching uses chemical or electrochemical processes to dissolve the materials. In dry etching, physical processes such as ion milling and sputter etching use ion bombardment to remove the unwanted materials; chemical processes such as plasma etching use active species to react with surface material and form volatile products; a combination of both processes, such as reactive ion etching, takes advantage of both principles. At the end of the process, the remaining resist is stripped away.

The lithography resolution limit is ultimately determined by the radiation wavelength. To

satisfy the ever-increasing demand for fabricating features at length scales below 100 nm, great efforts have been made to obtain a higher resolution. One strategy is to employ a radiation source with shorter wavelengths than conventional ultra-violet photos such as electron-beams (E-beam), extreme ultra-violet (EUV) light, focused ion beams, and X-rays. A comparison of these nanolithography techniques is given in Table 2.1 [36]. Alternative techniques such as near-field photolithography [37-42] are able to circumvent the diffraction limit and achieve feature sizes as small as 50 nm [39]. Nevertheless, lithography-based technologies suffer from limitations such as high capital and operating costs, low throughput, restriction to fabrication on planar substrates, corrosive etchants, high-energy radiation, and relatively high temperatures.

Table 2.1 Comparison of primary nanolithography techniques [36,43]

Technique	Radiation sources	Features	
		Dimension features	Other features
Optical/ Photo lithography	UV light	Resolution of 100 nm and min. inter-level alignment of 30 nm	Throughput of 10^{10} features s^{-1}
E-Beam and direct writing	Electron beam	Resolution of 10 nm and min. inter-level alignment of 10 nm	Max. working area of 1×1 μm^2 and throughput of 10^4 features s^{-1}
E-beam and etching	Electron beam	Resolution of 20 nm	Max. working area of 750×750 μm^2
X-ray lithography	X-ray	Resolution of 88 nm	Max. working area of 5×5 μm^2
Focused ion beam lithography	Ion beam	Resolution of 30 nm and min. inter-level alignment of 10 nm	Throughput of $10\text{-}10^2$ features s^{-1}
EUV lithography	EUV light	Resolution of 30 nm and min. inter-level alignment of 10 nm	Max. working area of 26×33 mm^2 and throughput of 10 features s^{-1}

2.2.2 Vapor phase growth

Vapor phase growth is a popular and extensively used mechanism for the synthesis of 1-D nanostructures. Two important mechanisms of vapor phase growth are vapor-liquid-solid (VLS) and vapor-solid (VS) growth. In both mechanisms, control of the supersaturation level determines the structural growth morphology.

Vapor-liquid-solid mechanism

In the past few years, the VLS mechanism has become widely used to generate 1-D inorganic nanostructures such as oxides (ZnO, SnO_2, ITO, MgO) [44-46], element semiconductors (Si, Ge) [47,48], III-V semiconductors (GaN, GaAs, InAs, InP) [49-52], II-VI semiconductors (ZnS, ZnSe, CdS, CdSe) [53-56], and recently CdS/Si coaxial nanowires [57]. Briefly, 1-D growth is induced by the dissolution of gaseous reactants into liquid droplets of catalyst material, followed by nucleation and growth of single crystalline nanostructures. The primary steps in a typical VLS growth process are shown schematically in Fig. 2.2. As the gaseous reactants dissolve into the metal catalysts, alloying occurs and the metal liquid alloy forms at the eutectoid temperature. Nanowire nucleation begins once the liquid droplet is supersaturated with the source element. Once the source element nanocrystal nucleates at the liquid-solid interface, further condensation/dissolution of the source element into the system will increase the amount of its precipitation from the alloy, leading to nanowire growth. It is also determined that there is a linear relationship between the initial catalyst particle size and the final nanowire diameter [47]. Gudiksen and Lieber demonstrated this linear correlation by showing that GaP nanowires of selective diameter can be synthesized by controlling the diameter of gold catalyst nanoparticles [58].
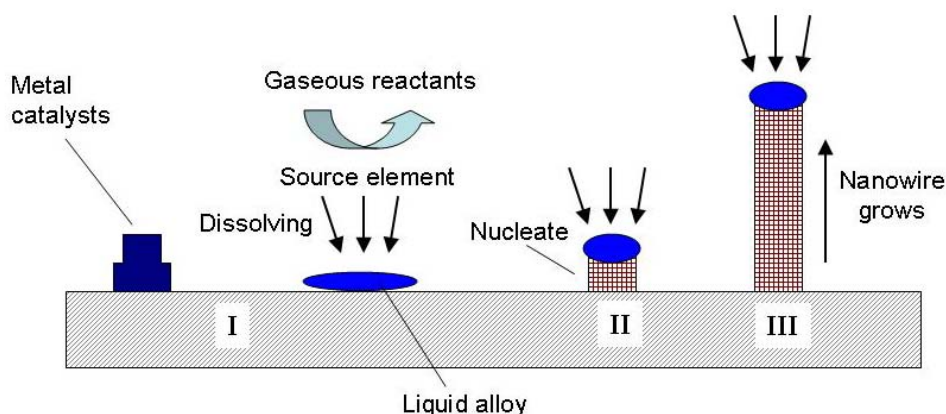
Fig. 2.2 Schematic illustration of vapor-liquid-solid nanowire growth mechanism including three stages (I) alloying, (II) nucleation, and (III) axial growth [47].

Other VLS methods include pulsed laser deposition (PLD), chemical vapor deposition (CVD), metal-organic chemical vapor deposition (MOCVD) and physical vapor deposition (PVD). A brief comparison of these methods is given in Table 2.2.

Table 2.2 The comparison of some VLS methods

Method	Description	Examples
PLD	Target material exposed to a laser beam is vaporized and subsequently deposited on a substrate. Usually used for catalyst preparation, followed by VLS.	Single crystal Si and Ge nanowires [59].
CVD	A catalyst is heated to high temperatures in a vacuum furnace, then chemical precursors in gaseous form flow through the tube reactor for a period of time.	Single-walled Carbon nanotubes [60] and CNTs [61].
MOCVD	Similar to CVD except catalyst-free.	ZnO nanowires grown on a Si substrate [62,63].
PVD	Nanostructures are deposited onto a substrate by physical means.	CdS nanowires grown by PVD of Cd S powders [64].

Vapor-solid mechanism

Vapor-solid growth has also been used widely to produce nanostructures, including oxide nanowires, whiskers of oxide, and metals with micrometer diameters [8,14]. In a typical VS process, the vapor species is generated by evaporation, chemical reduction or other gaseous reactions. These species are then transported and condensed onto the surface of a solid substrate in a temperature zone lower than that of the source material. 1-D growth will proceed without the need of a metal nanoparticle catalyst if the supersaturation in the solid phase is kept at a specific low level to control the nucleation and the subsequent growth process.

2.2.3 Solution based growth

Solution based growth (in aqueous or non-hydrolytic media) has been demonstrated as a promising alternative approach for mass production of metal, semiconductor, and oxide nanomaterials [8,14,15]. It mainly includes solution-liquid-solid (SLS), solvothermal, and hydrothermal growth mechanisms. The primary advantage of solution based methods as opposed to the vapor phase option is the ability to perform the growth at lower temperatures, lower cost, and higher yield on a wide variety of substrates. In addition, this technique is able to assemble nanocrystals with other functional materials to form hybrid nanostructures with multiple functions and thus has great potential for applications in nanoelectronic and biological systems.

Solution-liquid-solid methods

Buhro et al. [65-68] developed a low temperature SLS method similar to the VLS process for the synthesis of crystalline nanowires of III-V semiconductors (InP, InAs, GaAs). In this method, the precursors were delivered and reacted in the solution rather than the vapor phase. As shown in Fig. 2.3, a typical procedure consists of a solution dispersion of small liquid flux droplets and a solution phase that feeds the elements of the crystal phase into the flux droplets. Pseudo-one-dimensional growth of the crystal phase from the flux droplets occurs after the elements get supersaturated in the droplets. A metal (In, Sn, Bi) with a low melting point is usually used as a catalyst, and the desired material is generated through the decomposition of organometallic precursors dissolved in hydrocarbon solvents. The products

obtained are generally single-crystalline.
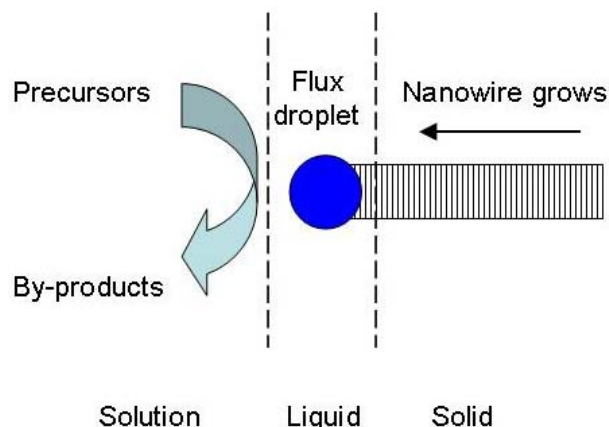
Fig. 2.3 Schematic illustration showing the growth of nanowire through the SLS mechanism [65].

Solvothermal and hydrothermal methods

Solvothermal and hydrothermal methods are successfully employed as solution routes to produce 1-D nanostructures such as Ge nanowires [69], CeS nanowires [70], ZnO nanowires [71,72], α-MnO$_2$ nanowires [73], and ZnS [74] and TiO nanostructures [75]. In these processes, water or other organic solvents is mixed with metal precursors and crystal growth regulating or templating agents, such as amines. This solution mixture is placed in an autoclave and maintained at relatively high temperatures and pressures to carry out the crystal growth and the assembly process.

2.2.4 Template-assisted synthesis

Template-assisted synthesis represents a convenient and versatile method to generate 1-D nanostructures. In this technique, a template with small holes within the host material serves as a scaffold against which nanostructures with complimentary morphologies are synthesized by filling the empty spaces. Broadly speaking, any material that can act as a "structural director" can be employed as the template including nanowires [76,77], nanorods [78], CNTs [79,80], DNA [81], and so-called "soft templates" such as some surfactants and organic dopants [82,83]. In this project the template is defined as a "hard template" such as an anodic aluminum oxide (AAO) membrane, nanochannel glass (NCG) [84,85], and porous

polymer membranes [86,87] in which the template contains nanoscale channels within the host material.

AAO templates have attracted increasing attention as a template for nanofabrication due to its simplicity and low cost [88,89]. It has been known for more than five decades that alumina exhibits porous structure under certain electrochemical anodization conditions [90,91]. A variety of electrolyte systems and a wide range of concentrations along with different temperatures and anodization regimes have been studied. So far, the smallest pore diameter reported is about 7 nm, using a sulfuric acid solution [92], while the largest, using a phosphoric acid solution, is about 300nm [93]. Pore densities as high as 10^{11} pores cm^{-2} can be obtained, and typical membrane thickness can range from 10 to 100 μm [88,94,95]. The cell size of the hexagonal pattern was found be to proportional to the anodization voltage [96], and the relationship between anodization voltage (V) and interpore distance (a) was expressed in the following equation:

$$a = d + 2\alpha V \tag{1}$$

where d is the diameter of the pore and α is a constant with value around 1.2 nm V^{-1} [90,91]. Moreover, different mechanisms such as mechanical stress [97-99] and cellular growth [100], have been proposed to describe the formation process of the self-ordered hexagonal pore array. The methods for fabricating nanopore arrays of alumina are well-established, and AAO membranes are commercially available (Whatman Anapore, Anotech Separations).

After the synthesis of templates, the nanoscale channels can be filled by electrochemical deposition, sol-gel, or a dip-coating method with a desired material. The 1-D nanostructures are released from the templates by removal of the host AAO [88,101,102].

Electrochemical deposition

Electroplating is widely used to deposit metals. In the mid of 1990's, the use of AAO template assisted electrochemical deposition to prepare metal nanostructures was proposed [88]. In this technique, the AAO template coated with a metallic conductive layer serves as a cathode for electrodeposition. When a voltage is applied between the cathode and anode, the cations in the electrolyte solutions are attracted to and get reduced near the cathode, which results in nanowire growth in the pores of the template. The length of the nanowires depends

on the length of the nanochannels and the electrodeposition duration. The AAO template-assisted fabrication approach has been proved to be a well-controlled approach to fabricate ordered inorganic nanomaterial arrays with narrow diameter distribution. Diameter of the nanomaterial arrays is limited by the pore size of the template which can be further controlled by the anodization conditions and the wet etching steps after anodization. Nanomaterials created through this technique include nanowires (Bi [103], Ni [104], Fe [105], Co [106], NiFe [107]), tubes (carbon [108] and Cu [109]), dots (Co [110], Au [111], Fe [112]), rods (Ga_2O_3-Al_2O_3 [113]), and superconducting materials (Sn [114]).

Sol-gel deposition

The sol-gel process involves the transition of a system of colloidal particles (the sol) into a solid phase (the gel). First the hydrolysis of a solution of precursor molecules forms a suspension of colloidal particles. Then the templates are immersedinto the solution and the condensation of the colloidal particles within the nanochannels yields a new gel phase. Finally post heat treatment turns the gel phase into solid nanostructures with good crystallinity. The main advantages of sol-gel techniques include low temperature of processing, versatility and easy chemical doping. Metal oxide nanowires ($LiCoO_2$ [115], $LiMnO_2$ [116], $LiNiO_3$ [117], TiO_2 [118]), nanotubes (In_2O_3 and Ga_2O_3 [119]), and element nanowires (Zr [120]) have been synthesized by this method.

Dip-coating deposition

The dip-coating process is similar to sol-gel deposition except that the template is put into a precursor solution instead of the sol solution. Silver nanotubes are synthesized by dipping the AAO template in $AgNO_3$ solution followed by drying, thermal decomposition, and subsequent dissolution of the AAO template [121].

2.3 Integration of carbon nanomaterials to materials with larger dimension scale

Carbon nanostructures have emerged as a new and attractive class of materials with unique electrical, mechanical, physical, and chemical properties [122,123]. They are actively studied for applications such as nanoelectronic devices [124-126], lithium ion battery electrode material [127], field emission displays [128], storage materials for hydrogen and

other gases [129], and probe tips for atomic force microscopy (AFM) [130]. A lot of research has focused on carbon nanotube (CNT) preparation techniques [131-135], theoretical simulation to understand the physics of carbon nanostructures [136-139], and CNT post-treatments such as purification, thermal annealing, and surface modification [140-142]. There is now a pressing need to integrate multicomponent nanoscale entities into multifunctional systems and to connect these nanosystems to the micro/macro world. Although a few innovative routes to the integration of CNTs into multidimensional and multicomponent systems have recently been devised [143-145], the effective connection of carbon nanostructures with materials and devices of larger length scales has been one of the long-standing obstacles in nanotechnology and still remains a big challenge.

On the other hand, the multifunctional systems incorporating carbon-based hierarchical structures are expected to provide advantageous properties for many applications. For example, inspired by the remarkable hierarchical hairy structure of the feet of geckos and many insects, researchers are working on creating new types of adhesives by mimicking this structure using CNTs-based hierarchical structures [146-148]. Studies of the carbon-based hierarchical structures as catalyst support for platinum particles for proton exchange membrane fuel cells show that they may improve the platinum utilization by securing the electronic route from platinum to the supporting electrode [149]. Thostenson demonstrated that by covering individual carbon fibers (CFs) with a sheath of CNTs and embedding this structure in a polymer matrix, the nanocomposite reinforcement resulted in local stiffening near the fiber/matrix interface and improved the interfacial shear strength [150]. S. Lim et al grew CNFs on activated CFs and used this composite to improve the efficiency of SO_x or NO_x removal [151]. Similar carbon hierarchical structures were studied for drinking water purification by selective chemosorption of chromate and heteropolymolybdate [152].

2.4 Application of nanomaterials as anode material for Li ion batteries

2.4.1 Nanostructured electrode for Li ion batteries

The Li-ion battery is one of the great successes of modern material electrochemistry [153]. A conventional Li-ion battery consists of a negative electrode (generally graphite), a

17

positive electrode (generally the lithium metal oxide, $LiCoO_2$), and a lithium ion conducting electrolyte (for example a solution of $LiPF_6$ in ethylene carbonate-diethylcarbonate). Although such batteries are commercially successful because they have high specific energy, energy density, and cycle life, they are reaching the limits in performance using the current electrode and electrolyte materials. In addition, they suffer from several inherent challenges such as the low discharge rate capability of graphite, limited volumetric and gravimetric energy density, safety, life span limitation by Li-alloying agglomeration, and the capacity loss due to the growth of passivation layers [154]. For applications in consumer electronics and power sources in hybrid and electric vehicles, further breakthroughs in materials are highly demanded.

It is now well established that limitations in the rate capability of Li-ion batteries are mainly caused by slow solid-state diffusion of Li^+ within the electrode materials [155,156]. Nanomaterials offer a promising alternative electrode material with remarkable properties. The potential advantages of nanostructured electrodes for Li-ion batteries include: 1) enabling new reactions not possible with bulk materials; 2) decreasing the particle size resulting in a short lithium ion transport length; 3) increasing the electrode/electrolyte contact area leading to a higher charge/discharge rate; 4) better accommodation of the strain of structure change in active materials; and 5) short path lengths for electronic transport permitting operation with low electronic conductivity of at high power [157,158]. The major obstacles associated with nanoelectrodes are: 1) increased electrode/electrolyte interface area leading to significant undesired electrode/electrolyte reactions, safety concerns and poor calendar life; 2) inferior packing of nanoparticles resulting in lower volumetric energy densities; and 3) the difficulty and expense in synthesizing the electrode [157].

Therefore there is a vigorous research effort in the use of nanomaterials to improve the rate capabilities of solid-state electrodes. Carbon nanobeads and tin-filled carbon nanotubes have been synthesized and studied for high-rate applications [159,160]. SnO_2 nanofiber based electrodes exhibited high capacities (>700 mAh g^{-1}) at a very high discharge current (~10 C) and still retained the ability to be discharged and recharged through as many as 800 cycles [161-163]. Manganese oxide and titanium oxide nanocomposites with conducting carbon

showed good discharge-charge performances as cathode and anode materials under large current density [164]. A honeycomb carbon anode containing an array of monodispersed nanopores delivered 50 times the capacity of a thin-film control anode at high discharge rates (10C) [165]. A nano/micro hierarchical Fe_2O_3/Ni wire electrode gave a high specific charge/discharge capacity of 780 mAh g^{-1} with good cycle performance in a high charge/discharge rate of 13 A g^{-1} [158]. Various nanoforms of TiO_2, including nanocrystalline anatase, amorphous TiO_2 and TiO_2 nanotubes, also received attention as high-rate Li-ion anode materials and indeed demonstrated improved property at high current densities [166-171].

2.4.2 Anode materials based on "conversion reactions"

A conventional Li-ion battery is based on the classical swing action of lithium ions between positive electrodes (generally lithium metal oxide, $LiCoO_2$) and negative electrodes (generally graphite). Recently, some nanostructured compounds such as CoO, CuO, NiO, Co_3O_4, and MnO, which are not suitable for the electrode in their usual macro-scale form, are under intensive investigation. For these materials, the charge/discharge process involves a novel reactivity mechanism, the so called "conversion reaction", as summarized in Eq. 1:

$$M_xN_y + yz\ e^- + yz\ Li^+ \leftrightarrow x\ M^0 + y\ Li_zN \qquad (2)$$
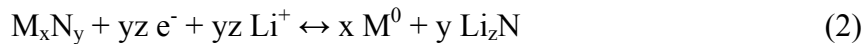
where M represents the metal cation and N, the non-metal anion. This mechanism differs from the classical lithium insertion/deinsertion process or Li-alloying reactions. The full electrochemical reduction of the compound M_xN_y involves multiple electrons per metal cation and will lead to the formation of composite materials consisting of nanometer-scale metallic clusters dispersed in an amorphous Li_2O matrix [172]. The highest specific capacity of the electrode material is attained by utilizing all the possible oxidation states of the transition metal during the redox cycle. This type of reaction is proven not to be unique to oxides and has been reported for sulphides, nitrides, fluorides, and phosphides [173]. One of the main advantages of this conversion reaction is the superior capacity compared with intercalation electrodes. Another attractive aspect is that such conversion reactions offer numerous opportunities to "tune" the voltage and capacity of the cell due to the fact that the cell potential is directly linked to the strength of the M-N bonding [154,157].

On the other hand, several issues have to be addressed to make full use of the materials

based on conversion reaction, as identified by N. G. Renganathan [154]: (1) poor kinetics that result in a large polarization, and hence a poor energy efficiency, (2) poor capacity retention upon cycling, (3) higher potentials, and hence a lower cell voltage, (4) irreversible capacity loss on the first cycle, and (5) low coulombic efficiency. To address these problems, different approaches have been explored such as studying different materials, coating the material surfaces with conducting materials such as carbon, using thin-film material instead of bulk material, and designing nanostructured electrodes. Some of the results are summarized in the Table 2.3.

Table 2.3 Anode materials based on conversion reactions

Material	Major results	Reference
RuO_2	Displays a 100% reversible conversion process involving $4e^-$. Coulombic efficiency of > 98%, a capacity of 1,110 mAh g^{-1} in the voltage range of 0.05-4.3 V and 99% Coulombic efficiency, a capacity of 730 mAh g^{-1} at 0.8-4.3 V.	[174,175]
α-Fe_2O_3 nanoparticles	With nanometer-scale haematite particles (20 nm), 1 Li per formular unit can be inserted in the corundum structure without phase transformation, among which 0.6 Li is reversibly inserted and the remaining 0.4 Li is irreversibly inserted.	[176,177]
α-Fe_2O_3 nanoparticles	A capacity of 1000 mAh g^{-1} at a rate of 100 mA g^{-1} is delivered with no overall fade after 50 cycles. A capacity of 700 mAh g^{-1} is obtained at a rate of 700 mA g^{-1}. Electron transport to and within the particles are the main factors limiting the rate.	[178]
Fe_2O_3 nanoflake	A stable capacity of 680 $\pm$ 20 mAh g^{-1} is obtained with no noticeable capacity fading up to 80 cycles, when cycled in the range of 0.005-3.0 V at 65 mA g^{-1} (0.1 C rate). A coulombic efficiency of >98% is shown after the 15th cycle.	[179]
Nanoparticles	A capacity of 700 mAh g^{-1} is demonstrated with 100%	[172]

of CuO, NiO, CoO, and FeO	capacity retention up to 100 cycles and at high recharging rates.	
Co_3O_4	Nanosized Co_3O_4 demonstrated a capacity more than 900 mAh g^{-1}. When starting from a highly divided oxide and using a low current, the discharge plateau is associated with the formation of α-CoO, subsequently leading to metallic cobalt upon further reduction. Alternatively, $Li_xCo_3O_4$ is formed when using materials with a large crystallite size and applying a high discharge rate, later similarly decomposing into divided metal.	[180,181]
Ni_3S_2	The nanostructured electrode exhibits a sustained reversible capacity at a rate of 2C with a loss of only 18% after 20 cycles and a outstanding rate capability (rate of 16C).	[182]
FeF_3-C nanocomposites	A reversible specific capacity of ~ 600 mAh g^{-1} was realized from 4.5 to 1.5 V at 70 ^{o}C. Approximately one-third of the capacity evolved in a reaction between 3.5 and 2.8 V related to the cathodic reduction reaction of Fe^{3+} to Fe^{2+}. The remainder of the specific capacity occurred in a two-phase conversion reaction at 2 V resulting in the formation of a finer Fe:LiF nanocomposites.	[183]
TiF_3 and VF_3	The reversible Li storage capacities are as high as 500 -600 mAh g^{-1}.	[184]
CoP_3	It provides a reversible capacity of 400 mAh g^{-1} at an average potential of 0.9 V vs Li/Li$^+$. Initial uptake of Li forms highly dispersed cobalt clusters embedded in a matrix of Li_3P; extraction of Li from this ion-conductive matrix on charge yields nano-particles of LiP, with little change evident in the oxidation state of the Co site.	[185]
NiP_2	A reversible capacity of 1000 mAh g^{-1} is obtained at an	[186]

average potential of 0.9 V vs Li^+/Li^o. It sustains 90% of its capacity over 15 cycles and can deliver its full capacity at 0.5C.	

Reference

[1]   Alivisatos, P.; Barbara, P. F.; Castleman, A. W.; Chang, J.; Dixon, D. A.; Kline, M. L.; McLendon, G. L.; Miller, J. S.; Ratner, M. A.; Rossky, P. J.; Stupp, S. I.; Thompson, M. I. *Adv. Mater.* **1998**, *10*, 1297.

[2]   Thiaville, A.; Miltat, J. *Science* **1999**, *284*, 1939.

[3]   Buzea, C.; Pacheco, I.; Robbie, K. *Biointerphases* **2007**, *2*, MR17.

[4]   Kuchibhatla, S.; Karakoti, A.S.; Bera, D.; Seal, S. *Prog. Mater. Sci.* **2007**, *52*, 699.

[5]   Wang, Z. L.; Hui, C. *Electron microscopy of nanotubes*; Kluwer Academic Publishers: Norwell, MA, 2003.

[6]   Baraton, M. I. *Synthesis, functionalization and surface treatments of nanoparticles*; American Scientific Publishers: Valencia, CA, 2003.

[7]   Yang, P. editor. *The chemistry of nanostructured materials*; World Scientific Publishing Co. Pte. Ltd.: River Edge, NJ, 2003.

[8]   Rao, C. N. R.; Deepak, F. L.; Gundiah, G.; Govindaraj, A. *Prog Solid State Chem.* **2003**, 31, 5.

[9]   Xia, Y. N.; Yang, P. D.; Sun, Y. G.; Wu, Y. Y.; Mayers, B. *Adv. Mater.* **2003**, *15*, 353.

[10] Suryanarayana, C. *Adv. Eng. Mater.* **2005**, *7*, 983.

[11] Gleiter, H. *Acta Mater.* **2000**, *48*, 1.

[12] Bera, D.; Deshpande, S.; Drake, C.; Seal, S. *Int. Mater. Rev.* **2007**, *317*, 29.

[13] Cavaleiro, A.; De Hosson, J. T. M. *Nanostructured coatings*; Springer Science New York, NY, 2006.

[14] Weber, J.; Singhal, R.; Zekri, S.; Kumar, A. *Inter. Mater. Rev.* **2008**, 53, 235.

[15] Wang, N.; Cai, Y.; Zhang, R. Q. *Mater. Sci. Eng. R.* **2008**, *60*, 1.

[16] Nalwa, H. S. *Handbook of Nanostructured Materials and Nanotechnology*; Academic Press: New York, NY, 2000**.**

[17] Feldheim, D. L.; Keating, C. D. *Chem. Soc. Rev.* **1998**, *27*, 1.

[18] Klein, D. L.; Roth, R.; Lim, A. K. L.; Alivisatos, A. P.; McEuen, P. L. *Nature* **1997**, *389*, 699.

[19] Kran, J. M.; van Rutenbeek, J. M.; Fisun, V. V.; Yanson, I. K.; Jongh, L. J. *Nature* **1995**, *375*, 767.

[20] Alivisatos, A. P. *Science* **1996**, *271*, 933.

[21] Bockrath, M.; Cobden, D. H.; McEuen, P. L.; Chopra, N. G.; Zettl, A.; Thess, A.; Smalley, R. E. *Science* **1997**, *275*, 1922.

[22] Venema, L. C.; Wildoer, J. W. G.; Janssen, J. W.; Tans, S. J.; Tuinstra, H. L. J. T.; Kouwenhoven, L. P.; Dekker, C. *Science* **1999**, *283*, 52.

[23] Bockrath, M.; Liang, W.; Bozovic, D.; Hafner, J. H.; Lieber, C. M.; Tinkham, M.; Park, H. *Science* **2001**, *291*, 283.

[24] Singh, L.; Ludovice, P. J.; Henderson, C. L. *Thin Solid Films* **2004**, *449*, 231.

[25] Torres, J. A.; Nealey, P. F.; de Pablo, J. J. *Phys. Rev. Lett.* **2000**, *85*, 3221.

[26] Wang, Z. L. *Adv. Mater.* **2000**, 12, 1295.

[27] Hu, J.; Odom, T. W.; Lieber, C. M. *Acc. Chem. Res.* **1999**, *32*, 1295.

[28] Xia, Y. N.; Yang, P. D.; Sun, Y. G.; Wu, Y. Y.; Mayers, B.; Gates, B.; Yin, Y. D.; Kim, F.; Yan, H. Q. *Adv. Mater.* **2003**, *15*, 353.

[29] Craighead, H. G. *Science* **2000**, *290*, 1532.

[30] International Technology Roadmap for Semiconductors web site. *http://public.itrs.net.*

[31] The National Technology Roadmap for Semiconductor Industry Association, **1999**.

[32] Sheats, J. R.; Smith, B.W. *Microlithography Science and Technology*; Marcel Dekker: NewYork, **1998**.

[33] Xia, Y.; Whitesides, G. M. Annu. Rev. Mater. Sci. 1998, 28, 153.

[34] Liu, G.; Xu, S.; Qian, Y. *Acc. Chem. Res*. **2000**, *33*, 457.

[35] Tseng, A. A. *Small* **2005**, *6*, 594.

[36] Ventra, M. D.; Evoy, S.; Heflin, J. R. *Introduction to Nanoscale Science and Technology*; Springer Science Business Media, Inc.: **2004**.

[37] Rogers, J. A.; Paul, K. E.; Jackman, R. J.; Whitesides, G.M. *Appl. Phys. Lett*. **1997**, *70*, 2658.

[38] Aizenberg, J.; Roger, J. A.; Paul, K. E.; Whitesides, G. M. *Appl. Phys. Lett*. **1997**, *71*, 3773.

[39] Alkaisi, M. M.; Blaikie, R. J.; McNab, S. J. *Microelectron. Eng*. **2000**, *53*, 237.

[40] Kuwahara, M.; Nakano, T.; Tominaga, J.; Lee, M. B.; Atoda, N. *Microelectron. Eng*. **2000**, *53*, 535.

[41] Blaikie, R. J.; Melville, D. O. S.; Alkaisi, M. M. *Microelectron. Eng*. **2006**, *83* , 723.

[42] Kley, E.; Clausnitzer, T. *Proceedings of SPIE* **2003**, *5184*, 115.

[43] Wei, M.; Zhi, D.; MacManus-Driscoll, J. L. *Nanotechnology* **2005**, *16*, 1364.

[44] Calestani, D.; Zha, M.; Salviati, G.; Lazzarini, L.; Zanotti, L.; Comini, E.; Sberveglieri, G. *J. Cryst. Growth.* **2005**, *275*, e2083.

[45] Chen, Y. Q.; Jiang, J.; Wang, B.; Hou, J. G. *J. Phys. D.* **2004**, *37D*, 3319.

[46] Yin, Y.; Zhang, G.; Xia, Y. *Adv. Funct. Mater.* **2002**, *12*, 293.

[47] Wu, Y.; Yang, P. *J. Am. Chem. Soc.* **2001**, *123*, 3165.

[48] Wu, Y.; Cui, Y.; Huynh, L.; Barrelet, C. J.; Bell, D. C.; Lieber, C. M. *Nano Lett.* **2004**, *4*, 433.

[49] Shin, H.; Thomson, D. B.; Schlesser, R.; Davis, R. F.; Sitar, Z. *J. Cryst. Growth* **2002**, *241*, 404.

[50] Wacaser, B. A.; Deppert, K.; Karlsson, L. S.; Samuelson, L.; Seifert, W. *J. Cryst. Growth* **2006**, *287*, 504.

[51] Park, H. D.; Prokes, S. M.; Cammarata, R. C. *Appl. Phys. Lett.* **2005**, *87*, 063110.

[52] Bhunia, S.; Kawamura, T.; Watanabe, Y.; Fujikawa, S.; Tokushima, K. *Appl. Phys. Lett.* **2003**, *83*, 3371.

[53] Lu, H. Y.; Chu, S. Y.; Chang, C. C. *J. Cryst. Growth* **2005**, *280*, 173.

[54] Chan, S. K.; Cai, Y.; Sou, I. K.; Wang, N. *J. Cryst. Growth* **2005**, *278*, 146.

[55] Gao, T.; Wang, T. *J. Phys. Chem. B* **2004**, *108B*, 20045.

[56] Shan, C. X.; Liu, Z.; Hark, S. K. *Nanotechnology* **2005**, *16*, 3133.

[57] Fu, X. L.; Li, L. H.; Tang, W. H. *Solid State Commun.* **2006**, *138*, 139.

[58] Gudiksen, M. S.; Lieber, C. M. *J. Am. Chem. Soc.* **2000**, *122*, 8801.

[59] Morales, A. M.; Lieber, C. M. *Science* **1998**, *279*, 208.

[60] Cassell, A. M.; Raymakers, J. A.; Kong, J.; Dai, H. *J. Phys. Chem. B* **1999**, *103*, 6484.

[61] Lee, C. J.; Park, J. *Appl. Phys. Lett.* **2000**, *77*, 3397.

[62] Zeng, Y. J.; Ye, Z. Z.; Xu, W. Z.; Zhu, L. P.; Zhao, B. H. *Appl. Surf. Sci.* **2005**, *250*, 280.

[63] Xu, W.; Ye, Z.; Zhu, L.; Zeng, Y.; Jiang, L.; Zhao, B. *J. Cryst. Growth* **2005**, *277*, 490.

[64] Wu, X. C.; Tao, Y. R. *J. Cryst. Growth* **2002**, *242*, 309.

[65] Trentler, T. J.; Hickman, K. M.; Geol, S. C.; Viano, A. M.; Gibbons, P. C.; Buhro, W. E. *Science* **1995**, *270*, 1791.

[66] Trentler, J. J.; Goel, S. C.; Hickman, K. M.; Viano, A. M.; Chiang, M. Y.; Beatty, A. M.; Gibbons, P. C.; Buhro, W. E. *J. Am. Chem. Soc.* **199 7**, *119*, 2172.

[67] Markowitz, P. D.; Zach, M. P.; Gibbons, P. C.; Penner, R. M.; Buhro, W. E. *J. Am. Chem.*

Soc. **2001**, *123*, 4502.

[68] Lourie, O. R.; Jones, C. R.; Bartlett, B. M.; Gibbons, P. C.; Ruoff, R. S.; Buhro, W. E. *Chem. Mater.* **2000**, *12*, 1808.

[69] Heath, J. R.; LeGoues, F. K. *Chem. Phys. Lett.* **1993**, *208*, 263.

[70] Wang, Q. Q.; Xu, G.; Han, G. R. *J. Solid State Chem.* **2005**, *178*, 2680.

[71] Vayssieres, L. *Adv. Mater.* **2003**, *15*, 464.

[72] Sun, Y.; Fuge, G. M.; Ashfold, M. N. R. *Chem. Phys. Lett.* **2004**, *396*, 21.

[73] Gao, Y.; Wang, Z.; Wan, J.; Zou, G.; Qian, Y. *J. Cryst. Growth* **2005**, *279*, 415.

[74] Yue, G. H.; Yan, P. X.; Yan, D.; Fan, X. Y.; Wang, M. X.; Qu, D. M.; Liu, J. Z. *Appl. Phys. A* **2006**, *84A*, 409.

[75] Zhang, Y. X.; Li, G. H.; Jin, Y. X.; Zhang, Y.; Zhang, J.; L. Zhang, D. *Chem. Phys. Lett.* **2002**, *365*, 300.

[76] Yin, Y.; Lu, Y.; Sun, Y.; Xia, Y. *Nano Lett.* **2002**, *2*, 427.

[77] Gates, B.; Wu, Y.; Yin, Y.; Yang, P.; Xia, Y. *J. Am. Chem. Soc.* **2001**, *123*, 11500.

[78] Song, J. H.; Kim, F.; Kim, D.; Yang, P. *Chem. Eur. J.* **2005**, *11*, 910.

[79] Govindaraj, A.; Staishkumar, B. C.; Nath, M. N.; Rao, C. N. R. *Chem. Mater.* **2000**, *12*, 202.

[80] Fullam, S.; Cottell, D.; Rensmo, H.; Fitzmaurice, D. *Adv. Mater.* **2000**, *12*, 1430.

[81] Mbindyo, J. K. N.; Reiss, B. D.; Martin, B. R.; Keating, C. D.; Natan, M. J.; Mallouk, T. E. *Adv. Mater.* **2001**, *13*, 249.

[82] Dietz, M. L.; Seifert, S.; Trasobares, S.; Miller, D. J.; Zaluzec, N. J.; Firestone, M. A. *Small* **2005**, *1*, 754.

[83] Zhu, Y. J.; Wang, W. W.; Qi, R. J.; Hu, X. L. *Angew Chem. Int. Ed.* **2004**, *43*, 1410.

[84] Berry, A. D.; Tonucci, R. J.; Fatemi, M. *Appl. Phys. Lett.* **1996**, *69*, 2846.

[85] Yeh, W. J.; Cheng, B.; Justus, B. L. *Physica C* **2003**, *388C-389C*, 433.

[86] Ursache, A.; Goldbach, J. T.; Russell, T. P.; Touminen, M. T. *J. Appl. Phys.* **2005**, *97*, 10J322.

[87] Thurn-Albrecht, T.; Schotter, J.; Kastle, G. A.; Emley, N.; Shibauchi, T.; Krusin-Elbaum, L.; Guarini, K.; Black, C. T.; Touminen, M. T.; Russell, T. P. *Science* **2000**, *290*, 2126.

[88] Martin, C. R. *Science* **1994**, *266*, 1961.

[89] Masuda H.; Fukuda, K. *Science* **1995**, *268*, 1466.

[90] Keller, F.; Hunter, M. S.; Robison, D. L. *J. Electrochem. Soc.* **1953**, *100*, 411.

[91] Franklin, R. W. *Nature*, **1957**, *187*, 1470.

[92] Zhang, Z.; Gekhtman, D.; Dreselhaus, M. S.; Ying, Y. *Chem. Mater.* **1999**, *11*, 1659.

[93] Masuda, H.; Yada, K.; Osaka, A. *Jpn. J. Appl. Phys. Part 2* **1998**, *37*, 1340.

[94] Martin, C. R. *Chem. Mater.* **1996**, *8*, 1739.

[95] Hulteen, J. C.; Martin, C. R. *J. Mater. Chem.* **1997**, *7*, 1075.

[96] Parkhutik, V. P.; Shershulsky, V. I. *J. Phys. D: Appl. Phys.* **1992**, *25*, 1257.

[97] Jessensky, O.; Muller, F.; Gosele, U. *J. Electrochem. Soc.* **1998**, *145*, 3735.

[98] Li, A. P.; Muller, F.; Bir. A.; Nielsch, K.; Gosele, U. *J. Appl. Phys.* **1998**, *84*, 6023.

[99] Nielsch, K.; Choi, J.; Schwirn, K.; Wehrspohn, R. B.; Gosele, U. *Nano Lett.* **2002**, *2*, 677.

[100] Zhang, L.; Cho. H. S.; Li, F.; Metzger, R. M.; Doyle, W. D. *J. Mater. Sci. Lett.* **1998**, *17*, 291.

[101] Almawlawi, D.; Liu, C. Z.; Moskovits, M. *J. Mater. Res.* **1994**, *9*, 1014.

[102] Zheng, M.; Zhang, L.; Zhang, X.; Zhang, J.; Li, G. *Chem. Phys. Lett.* **2001**, *334*, 298.

[103] Cornelius, T. W.; Brotz, J.; Chtanko, N.; Dobrev, D.; Miehe, G.; Neumann, R.; Molares, M. E. T. *Nanotechnology* **2005**, *16*, S236.

[104] Zhang, M.; Menon, L.; Zeng, H.; Liu, Y.; Bandyopadhyay, S.; Kirby, R. D.; Sellmyer, D. J. *Phys. Rev. B* **2000**, *62*, 12282.

[105] Yang, S.; Zhu, H.; Yu, D.; Jin, Z.; Tang, S.; Du, Y. *J. Magn. Magn. Mater.* **2000**, *222*, 97.

[106] Sun, M.; Zangari, G.; Metzger, R.M. *IEEE Trans. Magn.* **2000**, *36*, 3005.

[107] Khan, H. R.; Petrikowski, K. *J. Magn. Magn. Mater.* **2000**, *215-216*, 526.

[108] Zhou, D.; Anoshkina, E. V.; Chow, L.; Chai, G. *Carbon* **2006**, *44*, 1013.

[109] Li, N.; Li, X.; Yin, X.; Wang, W.; Qiu, S. *Solid State Commun.* **2004**, *132*, 841.

[110] Rastei, M. V.; Meckenstock, R.; Bucher, J. P.; Devaux, E.; Ebbesen, T. *Appl. Phys. Lett.* **2004**, *85*, 2050.

[111] Ghanem, M. A.; Bartlett, P. N.; de Groot, P.; Zhukov, A. *Electrochem. Commun.* **2004**, *6*, 447.

[112] Liu, K.; Nogues. J.; Leighton, C.; Masuda, H.; Nishio, K.; Roshchin, I. V.; Schuller, I. K. *Appl. Phys. Lett.* **2002**, *81*, 4434.

[113] Luo, Y.; Hou, Z.; Jin, D.; Gao, J.; Zheng, X. *Mater. Lett.* **2006**, *60*, 393.

[114] Tian, M.; Wang, J.; Snyder, J.; Kurtz, J.; Liu, Y.; Schiffer, P.; Mallouk, T. E.; Chan, M. H. W. *Appl. Phys. Lett.* **2003**, *83*, 1620.

[115] Zhou, Y.; Shen, C.; Li, H. *Solid State Ionics* **2002**, *146*, 81.

[116] Zhou, Y. K.; Huang, J.; Li, H. L. *Appl. Phys. A* **2003**, *76A*, 53.

[117] Yang, Z.; Huang, Y.; Dong, B.; Li, H. L. J. *Solid State Chem.* **2005**, *178*, 1157.

[118] Lin, Y.; Wu, G. S.; Yuan, X. Y.; Xie, T.; Zhang, L. D. *J. Phys. Condens, Matter.* **2003**, *15*,

2917.

[119] Cheng, B.; Samulski, E. T. *J. Mater. Chem.* **2001**, *11*, 2901.

[120] Xu, H.; Qin, D. H.; Yang, Z.; Li, H. L. *Mater. Chem. Phys.* **2003,** *80*, 524.

[121] Qu, L.; Shi, G.; Wu, X.; Fan, B. *Adv. Mater.* **2004**, *16*, 1200.

[122] Dai, H.; Hafner, J. H.; Rinzler, A. G.; Colbert, D. T.; Smalley, R. *Nature* **1996**, *384*, 147.

[123] Forro, L.; Schnonenberger, C. *Carbon Nanotubes Synthesis, Structure, Properties and Applications*; Springer: New York, NY, 2001.

[124] Hertel, T.; Martel, R.; Avouris, P. *J. Phys. Chem. B* **1998**, *102*, 910.

[125] Bower, C.; Zhu, W.; Shalom, D.; Lopez, D.; Chen, L. H.; Gammel, P. L.; Jin, S. *Appl. Phys. Lett.* **2002**, *80*, 3820.

[126] Teo, K. B.; Chhowalla, M.; Amaratunga, G. A.; Miline, W. I.; Legagneux, P.; Pirio, G.; Gangloff, L.; Pribat, D.; Semet, V.; Binh, V. T. *J. Vac. Sci. Technol. B* **2003**, *21*, 693.

[127] Gao, B.; Kleinhammes, A.; Tang, X.; Bower, C.; Fleming, L.; Wu, Y.; Zhou, O. *Chem. Phys. Lett.* **1999**, *307*,153.

[128] Saito, Y.; Hamaguchi, K.; Hata, K.; Tohji, K.; Kasuya, A.; Nishina, Y.; Uchida, K.; Tasaka, Y.; Ikazaki, F.; Yumura, M. *Ultramicroscopy* **1998**, *73*, 1.

[129] Gadd, G. E.; Blackfold, M.; Moricca, S.; Webb, N.; Evans, P. J.; Smith, A. M.; Jacobsen, G.; Leung, S.; Day, A.; Hua, Q. *Science* **1997**, *277*, 933.

[130] Wong, S. S.; Harper, J. D.; Lansbury, P. T.; Lieber, C. M. *J. Am. Chem. Soc.* **1998**, *120,* 603.

[131] Ebbesen, T. W.; Ajayan, P. M. *Nature* **1992**, *358*, 220.

[132] Thess, A.; Lee, R.; Nikolaev, P.; Dai, H.; Petit, P.; Robert J.; Xu, C.; Lee, Y. H.; Kin, S. G.; Rinzler, A. G.; Colbert, D. T.; Scuseria, G. E.; Tomanek, D.; Fischer, J. E.; Smalley, R. E. *Science* **1996**, *273*, 483.

[133] Dresselhouse, M. S.; Dresselhouse, G.; Avouris, P. *Carbon nanotubes: synthesis, structure, properties and application*; Springer: New York, NY, 2001.

[134] Ren, F.; Huang, Z. P.; Xu, J. W.; Wang, J. H.; Bush, P.; Siegal, M. P.; Provencio, P. N. *Science* **1998**, *282*, 1105.

[135] Boskovic, B. O.; Stolojan, V.; Khan, R. U. A.; Haq, S.; Silva, S. R. P. *Nat. Mater.* **2002**, *1*, 165.

[136] Maiti, A.; Andzelm, J.; Svizhenko, A.; Anantram, M. P.; Panhuis, M. *Phys. Status Solid B*

2002, *233*, 49.

[137] Efremenko, I.; Sheintuch, M. *Langmuir* **2005**, *21*, 6282.

[138] Margulis, I. A.; Muryumin, E. E.; Tomilin, O. B. *Physica B* **2004**, *353*, 314.

[139] Natsuki, T.; Endo, M. *Carbon* **2004**, *42*, 2147.

[140] Li, C.; Liu, H.; Tseng, S.; Lin, Y.; Chen, S.; Li, J.; Wu, K.; Juang, J. *Diam. Relat. Mater.* **2006**, *15*, 2010.

[141] Han, J.; Lee, S. H.; Berdinsky, A. S.; Kim, Y. W.; Yoo, J.; Park, C.; Choi, J. J.; Jung, T.; Han, I. T. Kim, J. M. *Diam. Relat. Mater.* **2005**, *14*, 1891.

[142] Tzeng, S.; Hung, K.; Ko, T. *Carbon* **2006**, *44*, 859.

[143] Yang, J.; Dai, L.; Vaia, R. A. *J. Phys. Chem. B* **2003**, *107*, 12387.

[144] Hou, H. Q.; Reneker, D. H. *Adv. Mater.* **2004**, *16*, 69.

[145] Cao, A.; Veedu, Y. V. P.; Li, X. S.; Yao, Z. L.; Ghasemi-Nejhad, M. N.; Ajayan, P. M. *Nat. Mater.* **2005**, *4*, 540.

[146] Sitti, M.; Fearing, R. S. *J. Adhesion Sci. Tech.* **2003**, *17*, 1055.

[147] Yurdumakan, B.; Raravikar, N.R.; Ajayan, P.M.; Dhinojwala, A. *Chem. Commun.* **2005**, *30*, 3799-3801.

[148] Spolenak, R.; Gorb, S.; Arzt, E. *Acta Biomaterialia* **2005**, *1*, 5.

[149] Wang, C.; Waje, M.; Wang, X.; Tang, J. M.; Haddon, R. C.; Yan, Y. *Nano Lett.* **2004**, *4*, 345.

[150] Thostenson, E. T.; Li, W. Z.; Wang, D. Z.; Ren. Z. F.; Chou, T. W. *J. App. Phys.* **2002**, *91*, 6034.

[151] Lim, S.; Yoon, S.; Shimizu, Y.; Jung, H.; Mochida, I. *Langmuir* **2004**, *20*, 5559.

[152] Su, D. S.; Chen, X.; Weinberg, G.; Klein-Hofmann, A.; Timpe, O.; Hamid, S. B. A.; Schlogl, R. *Angew Chem. Int. Ed.* **2005**, *44*, 5488.

[153] Scrosati, B. *Nature* **1995**, *373*, 557.

[154] Malini, R.; Uma, U.; Sheela, T.; Ganesan, M.; Renganathan, N. G. *Ionics* **2008**, online first.

[155] Li, J.; Tang, Z.; Zhang, Z. *Electrochem. Commun.* **2005**, *7*, 62.

[156] Bruce, P. G. *Chem. Commun.* **1997,** *19*, 1817.

[157] Arico, A. S.; Bruce, P.; Scrosati, B.; Tarascon, J. M.; Schalkwijk, W. V. *Nat. Mater.* **2005,** *4*, 366.

[158] Hosono, E.; Fujihara, S.; Honma, I.; Ichihara, M.; Zhou, H. *J. Electrochem. Soc.* **2006,** *153*, A1273.

[159] Wang, H.; Abe, T.; Maruyama, S.; Iriyama, Y.; Ogumi, Z.; Yoshikawa, K. *Adv. Mater.*

2005, *17*, 2857.

[160] Kumar, T. P.; Ramesh, R.; Lin, Y. Y.; Fey, G. T. *Electrochem. Commun.* **2004,** *6*, 520.

[161] Li, N.; Martin, C. R.; Scrosati, B. *J. Power Sources* **2001,** *97-98*, 240.

[162] Li, N.; Martin, C. R.; Scrosati, B. *Electrochem. Solid-State Lett.* **2000,** *3*, 316.

[163] Li, N.; Martin, C. R. *J. Electrochem. So.* **2001,** *148*, A164.

[164] Kawaoka, H.; Hibino, M.; Zhou, H.; Honma, I. *Solid State Ionics* **2005,** *176*, 621.

[165] Li, N.; Mitchell, D. T.; Lee, K. P.; Martin, C. R. *J. Electrochem. Soc.* **2003,** *150*, A979.

[166] Subramanian, V.; Karki, A.; Gnanasekar, K.I.; Eddy, F. P.; Rambabu, B. *J. Power Sources* **2006**, *159*, 186.

[167] Hibino, M.; Abe, K.; Mochizuki, M.; Miyayama, M. *J. Power Sources* **2004,** *126*, 139.

[168] Wagemaker, M.; Kentgens, A. P. M.; Mulder, F. M. *Nature* **2002,** *418*, 397.

[169] Zhou, Y. K.; Cao, L.; Zhang, F. B.; Li, H. L. *J. Electrochem. Soc.* **2003,** *150*, A1246.

[170] Guerfi, A.; Charest, P.; Kinoshita, K.; Perrier, M.; Zaghib, K. *J. Power Sources* **2004,** *126*, 163.

[171] Armstrong, A. R.; Armstrong, G.; Canales, J.; Bruce, P. G. *J. Power Sources* **2005,** *146*, 501.

[172] Poizot, P.; Laruelle, S.; Grugeon, S.; Dupont, L.; Tarascon, J. M. Nature 2000, 407, 496.

[173] Nazri, G.A.; Pistoia, G. *Lithium Batteries Science and Technology*; Kluwer Academic/Plenum: Boston, MA, 2004.

[174] Balaya, P.; Li, H.; Kienle, L.; Maier, J. *Adv. Funt. Mater*. **2003**, *13*, 621.

[175] Maier J. Nat. Mater. **2005**, 4, 805.

[176] Larcher, D.; Masquelier, C.; Bonnin, D.; Chabre, Y.; Masson, V.; Leriche, J. B.; Tarascon, J. M. *J. Electrochem. Soc*. **2003**, *150*, A133.

[177] Larcher, D.; Bonnin, D.; Cortes, R.; Rivals, I.; Personnaz, L.; Tarascon, J. M. *J. Electrochem. Soc*. **2003**, *150*, A1643.

[178] Jiao, F.; Bao, J.; Bruce, P. G. *Electrochem. Solid State Lett*. **2007**, *10*, A 264.

[179] Reddy, M. V.; Yu, T.; Sow, C.; Shen, Z. X.; Lim, C. T.; Rao, G. V. S.; Chowdari, B. V. R. *Adv. Funct. Mater*. **2007**, *17*, 2792.

[180] Laruelle, S.; Grugeon, S.; Poizot, P.; Dolle, M.; Dupont, L.; Tarascon, J. M. *J. Electrochem. Soc*. **2002**, *149*, A627.

[181] Yuan, Z.; Huang, F.; Feng, C.; Sun, J.; Zhou, Y. *Mater Chem Phys*. **2003**, *79*, 1.

[182] Wang, Q.; Gao, R.; Li, J. *Appl. Phys. Lett*. **2007**, *90*, 143107.

[183] Badway, F.; Cosandey, F.; Pereira, N.; Amatucci, G. G. *J. Electrochem. Soc*. **2003**, *150*, A1318.

[184] Li, H.; Richter, G.; Maier, J. *Adv. Mater.* **2003**, *15*, 736.

[185] Pralong, V.; Souza, D. C. S.; Leung, K. T.; Nazar, L. F. *Electrochem. Comm.* **2002**, *4*, 516.

[186] Gillot, F. Boyanov, S.; Dupont, L.; Doublet, M. L.; Morcrette, M.; Monconduit, L.; Tarascon, J. M. *Chem. Mater.* **2005**, *17*, 6327.

CHAPTER III: PUBLICATIONS

This section is structured as a collection of papers – each presented as a subsection outlined in the research plan.

PAPER # 1: A GENERIC SYNTHETIC APPROACH TO FABRICATE Y-JUNCTION METAL NANOWIRES BY AAO TEMPLATES-ASSISTED AC ELECTRODEPOSITION

(submitted to *Electrochemistry Communication*)

ABSTRACT

In this communication, we report a generic synthetic approach to fabricate Y-junction metal nanowires by AC electrodeposition using a hierarchically designed AAO template. Y-junction Co NWs and Y-junction Cu NWs were synthesized as examples. A morphology study showed that the diameters of the stem and branches of the Y-junction NWs were about 40 nm and 20 nm respectively, which was defined by the nanochannels in the template. Structural analysis indicated that Co NWs had a mixture of FCC and HCP structures, whereas Cu NWs had an FCC structure with a <110> texture. The present method can be extended to other metallic systems and thus provides a simple and efficient way to fabricate Y-junction metal NWs.

1. Introduction

Metal nanowires (NWs) have attracted vigorous research interests in recent years. Among the numerous synthesis methods studied so far, fabrication inside rationally designed anodic aluminum oxide (AAO) templates has been proved to be an economic and versatile method to produce nanostructures with great efficiency and precision. The AAO templates have many desirable characteristics such as a wide-range of narrowly distributed pore size, a well-developed fabrication process, easy to remove, good mechanical and thermal stability, and chemical inertness [1-3]. Since the pioneered work by T.M. Whitney [4], AAO

template-assisted fabrication has achieved great success in the synthesis of linear metal nanowires. Especially in some applications such as nanoelectronics where Y-junction nanowires are desirable, AAO template-assisted fabrication offers a simple and efficient method for preparation of Y-junction metal NWs. Although in the past few years a few reports were available on the formation of Y-junciton carbon nanotubes [5,6], only limited progress has been made on the synthesis of metallic Y-junction or branched nanowires [7-10]. A typical synthesis process is as following: first the AAO templates are separated from the Al substrate; after the removal of the barrier layer, the templates are coated with a thin layer of noble metal to make an electrode; then target metal is deposited into the templates by direct current (DC) electrodeposition. To our knowledge, no study has been reported using alternate current (AC) electrodeposition to fabricate metallic Y-junction NWs even though this method was proven to be a simple fabrication process to make linear metal nanowires [11-16].

In this communication, we report a generic synthetic approach to fabricate Y-junction metal nanowires by AC electrodeposition using AAO templates with well-controlled Y-junction channels. Examples of Y-junction Co NWs and Y-junction Cu NWs were presented and their morphology and structure were characterized by scanning electron microscopy (SEM), transmission electron microscopy (TEM), selected area electron diffraction (SAED), and X-ray diffraction (XRD).

2. Experimental

2.1. Materials preparation

Co NWs were synthesized by electrodeposition assisted by a hierarchically designed AAO template. Fig. 1 provides a schematic of the synthesis steps. The AAO templates were obtained by a well-established two-step anodization process [17-19]. Briefly, the first anodic oxidation of aluminum (99.999% pure, Electronic Space Products International) was carried out in a 0.3 M oxalic acid solution at 40 V and 10 $^\circ$C for 16–20 h. The porous alumina layer formed during this first anodization step was completely dissolved by a mixture solution of 6% phosphoric acid and 1.8% chromic acid at 70 $^\circ$C. The sample was then subjected to a second anodization where initially the anodization was performed under the same conditions as in the first anodization to produce the primary stem pores, and then the anodizing voltage

was reduced by a factor of $1/\sqrt{2}$ to create the Y-branched pores. The as-prepared AAO templates were wet etched in 0.5% H_3PO_4 for half an hour to thin the barrier layer and widen the pores. The length of the stem and the branches was adjusted by varying the time of the second anodization step.
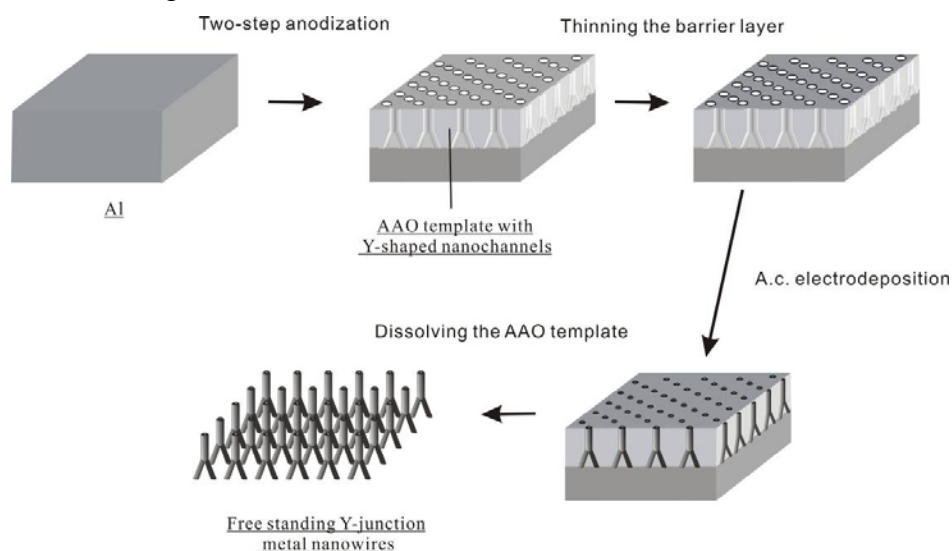

Fig. 1 Schematic of the process to synthesize Y-junction metal NWs.

Cobalt nanowires were electrochemically deposited by AC electrolysis in this nanoporous template with Y-junction nanochannels using 14 Vrms at 100 Hz for 30 min in an electrolyte solution consisting of 240 g l^{-1} of $CoSO_4 \cdot 7H_2O$ (Alfa Aesar), 40 g l^{-1} of HBO_3 (Alfa Aesar), and 1 g l^{-1} of ascorbic acid (Alfa Aesar) [17-19]. Graphite was used as the counter electrode. After Co deposition, AAO could be fully removed by etching with a 2 M NaOH solution to obtain free standing Y-junction Co NWs.

The synthesis of copper nanowires was adapted from G.A. Gelves's work [15,16]. Electrodeposition of the Y-junction Cu NWs was carried out in an aqueous solution consisting of 0.50 M $CuSO_4$ (Alfa Aesar) and 0.285 M H_3BO_3 by applying a continuous 200 Hz sine wave at 10Vrms for 10 min between the anodized Al and the graphite counter electrode.

2.2 Materials characterization

XRD patterns were recorded on a Rigaku Miniflex diffractometer using a Cu Kα X-ray source (1.5405 Å). The structure and morphology were characterized by SEM using a JEOL JSM-7000F microscope and by TEM using a Phillips CM 12 operated at an accelerating voltage of 120 kV. TEM samples were prepared as follows: first the Y-junction NWs were

liberated from the AAO template by dissolving the template in 2 M NaOH for 1 hour. After rinsing with DI water and dispersing the NWs in ethonal by sonication, a few drops of the dispersed solution were placed onto a carbon-coated Cu grid and dried in air.

The dimensions of the Y-junction AAO channels and the Y-junction metal NWs were analyzed using the image processing software of Image J. The dimensions were measured at ten different spots from multiple SEM and TEM images and the average and standard deviations were reported.

3. Results and discussion

The top-view SEM image (Fig. 2a) shows that these pores form a highly ordered hexagonal pattern. Careful examination of the cross-section images (Fig. 2b) by the image processing software Image J reveals that the diameters of the stems and branches of the Y-junction channels are 39.2 $\pm$ 4.2 and 19.6 $\pm$ 4.4 nm, respectively. It is notable that while the diameters of the branches are usually half that of the stems when the branches are formed at $1/\sqrt{2}$ of the voltage for the formation of the stems, the lengths of the stems and the branches of the Y-junction channels can be independently adjusted by controlling the anodization duration for each segment.
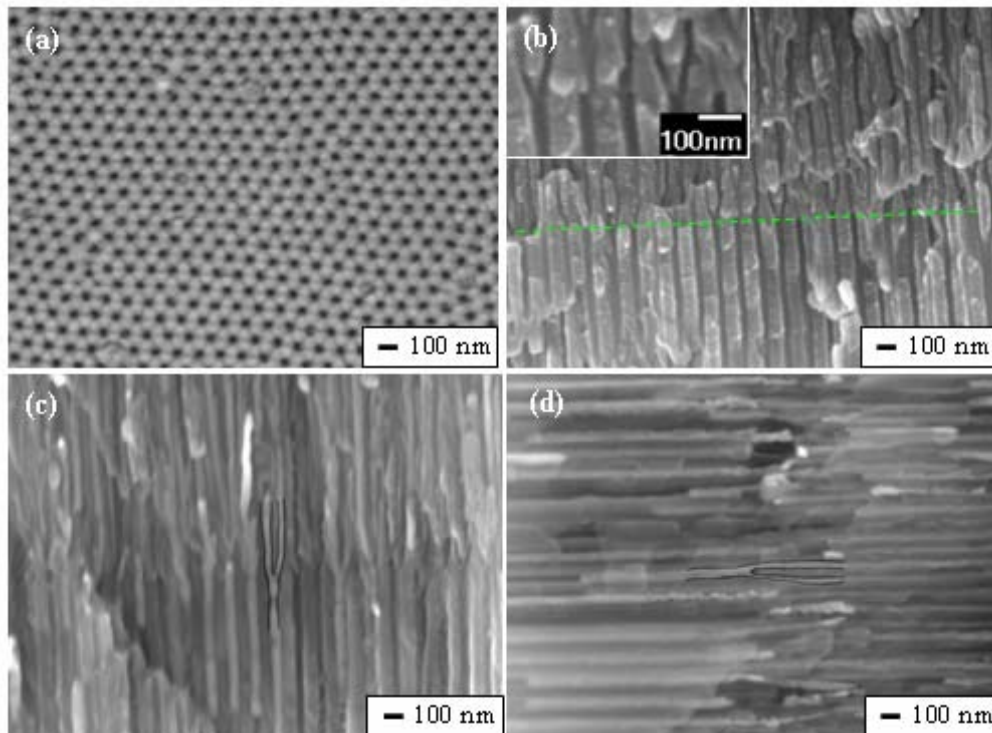
Fig. 2 SEM images of (a), (b) AAO templates with Y-junction nanochannels before electrodeposition, and after electrodeposition of (c) Co and (d) Cu.

Typical SEM images of the cross-section view of the Y-junction Co NWs and Y-junction Cu NWs are shown in Fig. 2c and d. Clearly, the NWs are parallel to each other and well contained in the Y-branched nanochannels. Statistical measurement by Image J shows that for Y-junction Co NWs, the diameters of the stems and branches are 39.3 nm $\pm$ 5.6 nm and 20.9 nm $\pm$ 4.8 nm, respectively; while for Y-junction Cu NWs the diameters of the stems and branches are 40.3 nm $\pm$ 4.6 nm and 21.9 nm $\pm$ 4.2 nm, respectively. Obviously, they are in close agreement to the dimension of the Y-junction AAO nanochannels.
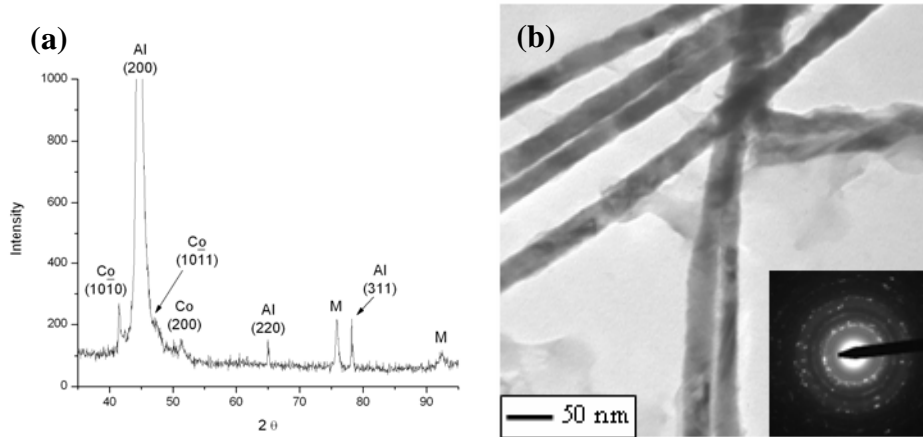

Fig. 3 (a) XRD pattern for the Y-junction Co NWs embedded in AAO template. (b) TEM of the Y-junction Co NWs. Inset: SAED patterns for (b).

The XRD pattern for the Y-junction Co NWs embedded in the AAO template is shown in Fig. 3a. It shows that the Co NWs consist of a mixture of face-center-cubic (FCC) and hexagonal-close-packed (HCP) structures. The peak near 76° could be a combination of the diffraction from the (110) plane of the HCP structure and the (220) plane of the FCC structure, and that near 92.5° could be a combination of the diffraction from the (112) plane of the HCP structure and the (311) plane of the FCC structure. The coexistence of FCC and HCP structures has been observed in the electrodeposited straight Co NWs in previous studies using DC, AC, or pulsed deposition techniques [20-23]. It suggests a complex growth mechanism because HCP Co NWs and FCC Co NWs are generally believed to be obtained by two distinct mechanisms, namely, two-dimensional layer-by-layer growth and three-dimensional nucleation/growth [24,25]. The growth mechanism can be affected by the

synthesis conditions such as pH value of the electrolyte [24], frequency of the power source [26], and the deposition potential [27].

Fig. 3b shows a bright-field TEM image of Y-junction Co NWs after the AAO template has been completely dissolved. Obviously, the Y-junction Co NWs have well-defined stems and branches. SAED was performed to investigate the crystalline structures of the Y-junction Co NWs. The broken ring SAED patterns suggest that the structures are polycrystalline in nature. The patterns are complicated due to the change of the growth direction at the junction as well as the coexistence of HCP and FCC structures as shown in XRD results.
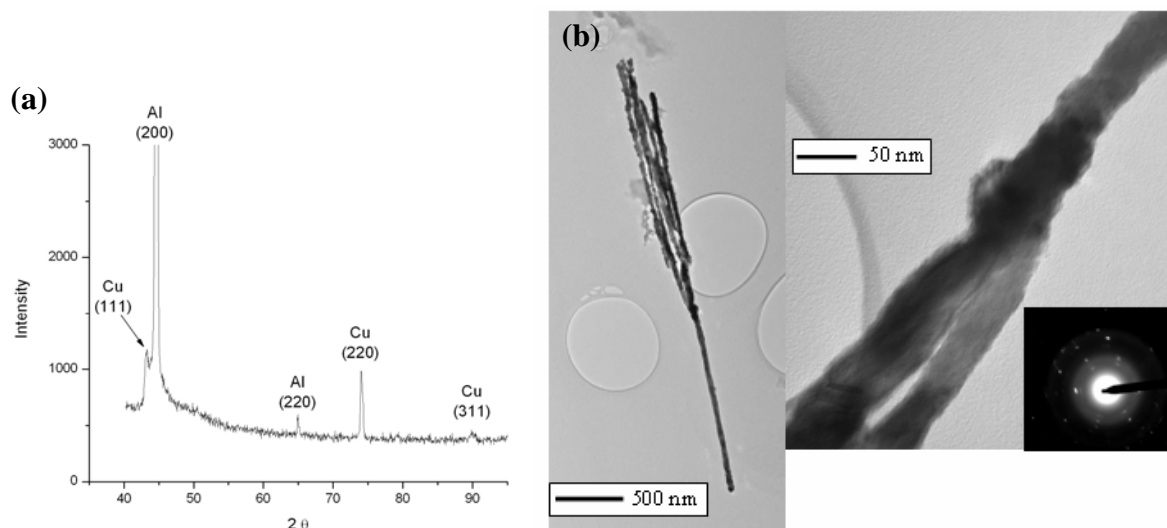

Fig. 4 (a) XRD pattern for the Y-junction Cu NWs embedded in AAO template. (b) TEM of the Y-junction Cu NWs. Inset: SAED patterns for (b) taken along the $[1\bar{1}1]$ zone axis perpendicular to the long axis of the NWs.

The XRD pattern for the Y-junction Cu NWs embedded in the AAO template (Fig. 4a) shows that all the peaks, except the peaks near 45° and 65° associated with the Al substrate, correspond to FCC Cu. The strongest peak in Fig. 4a for Cu (220) suggests that the Cu NWs exhibit a <110> texture, which is interesting because for bulk FCC structures the most energetically favorable texture is <111>. For electrodeposited metal NWs by DC technique, the texture was found to be affected by synthesis conditions such as electrolyte composition, overpotential, and temperature [28,29]. Possible reasons include that: (1) the adsorbed H ions on the cathode may stabilize the (110) face [30]; and that (2) the relative high potential may induce the thermodynamic to kinetic phase transition from [100] to [110] in the nucleation process [28].

Fig. 4b depicts the TEM images of Y-junction Cu NWs. Analysis by Image J shows that the stem and branches of individual Y-junction Cu NWs have diameters of 42.8 $\pm$ 7.4 nm and 35.8 $\pm$ 5.3 nm, respectively. Similar analysis of TEM images of Y-junction Co NWs shows that the diameters of the stem and branches are 42.2 nm $\pm$ 4.0 nm and 28.1 nm $\pm$ 4.2 nm, respectively. Clearly, the diameters of the stems and branches of both metal NWs are larger compared to the results estimated by SEM images. The dimension increase of the metal NWs may be due to the surface oxidation during the template removal or TEM sample preparation process [31]. The spotty diffraction rings in Fig. 4b (inset) show the polycrystalline nature of the Cu NWs.

4. Conclusions

In summary, by using a hierarchically designed AAO template, we developed a generic synthetic approach to fabricate Y-junction metal nanowires by AC electrodeposition. For the Y-junction Co NWs and Y-junction Cu NWs fabricated in this communication, a morphology study shows that well-defined Y-junctions were synthesized, and the dimensions of the NWs were defined by the template. Structure analysis indicated that the Co NWs were a mixture of FCC and HCP structures, and Cu NWs had FCC structure with a <110> texture. The present method can be extended to other metallic systems and thus provides a simple and efficient way to fabricate Y-junction metal NWs. Future work includes studying the effects of the synthesis parameters such as potential, frequency, and temperature on the crystal structure of the fabricated metal NWs.

Acknowledgment

References

[1] H. Masuda, F. Hasegwa, S. Ono, J. Electrochem. Soc. 144 (1997) 127.

[2] A. P. Li, F. Muller, A. Birner, K. Nielsch, U. Gosele, J. Appl. Phys. 84 (1998) 6023.

[3] O. Jessensky, F. Muller, U. Gosele, Appl. Phys. Lett. 72 (1998) 1173.

[4] T. M. Whitney, J. S. Jiang, P. C. Searson, C. L. Chien, Science 261 (1993) 1316.

[5] J. Li, C. Papadopoulos, J. Xu, Nature 402 (1999) 253.

[6] G. Meng, Y. J. Jung, A. Cao, R. Vajtai, P. M. Ajayan, Proc. Natl. Acad. Sci. 102 (2005) 7074.

[7] T. Gao, G. Meng, J. Zhang, S. Sun, L. Zhang, Appl. Phys. A: Mater. Sci. Process. 74 (2002) 403.

[8] J. Choi, G. Sauer, K. Nielsch, R. B. Wehrspohn, U. Gosele, Chem. Mater. 15 (2003) 776.

[9] Y. Tian, G. Meng, S. K. Biswas, P. M. Ajayan, S. Sun, L. Zhang, Appl. Phys. Lett. 85 (2004) 967.

[10] S. Mahima, R. Kannan, I. Komath, M. Aslam, V.K. Pillai, Chem. Mater. 20 (2008) 601.

[11] A. J. Yin, J. Li, W. Jian, A. J. Bennett, J. M. Xu, Appl. Phys. Lett. 79 (2001) 1039.

[12] X. Y. Zhang, G. H. Wen, Y. F. Chan, R. K. Zheng, X. X. Zhang, N. Wang, Appl. Phys. Lett. 83 (2003) 3341.

[13] N. J. Gerein, J. A. Haber, J. Phys. Chem. B 109 (2005) 17372.

[14] R. L. Wang, S. L. Tang, B. Nie, X. L. Fei, Y. G. Shi, Y. W. Du, Solid State Comm. 142 (2007) 639.

[15] G. A. Gelves, B. Lin, U. Sundararaj, J. A. Haber, Adv. Funct. Mater. 16 (2006) 2423.

[16] G. A. Gelves, Z. T. Murakami, M. M. J. Krantz, J. A. Haber, J. Mater. Chem. 16 (2006) 3075.

[17] J. Liang, H. Chik, A. Yin, J. M. Xu, J. Appl. Phys. 91 (2002) 2544.

[18] J. Liang, H. Chik, J. M. Xu, IEEE J. Sel. Top. Quantum Electron. 8 (2002) 998.

[19] J. Li, C. Papadopoulos, J. M. Xu, M. Moskovits, Appl. Phys. Lett. 75 (1999) 367.

[20] F. Li, T. Wang, L. Ren, J. Sun, J. Phys.: Condens. Matter. 16 (2004) 8053.

[21] G. Tourillon, L. Pontonnier, J. P. Levy, V. Langlais, Electrochem. Solid-State Lett. 3 (2000) 20.

[22] G. J. Strijkers, J. H. J. Dalderop, M. A. A. Broeksteeg, H. J. M. Swagten, W. J. M. de Jonge, J. Appl. Phys. 86 (1999) 5141.

[23] N. R. Pradhan, H. Duan, J. Liang, G. S. Iannacchione, Nanotechnology 19 (2008) 485712.

[24] H. Pan, H. Sun, C. Poh, Y. Feng, J. Lin, Nanotechnology 16 (2005) 1559.

[25] M. Tian, J. Wang, J. Kurtz, T. E. Mallouk, M. H. Chan, Nano Lett. 3 (2003) 919.

[26] J. Zhang, G. A. Jones, T. H. Shen, S. E. Donnely, G. Li, J. Appl. Phys. 101 (2007) 054310.

[27] X. W. Wang, G. T. Fei, P. Tong, X. J. Xu, L. D. Zhang, J. Crystal Growth 300 (2007) 421.

[28] J. A. Switzer, H. M. Kothari, E. W. Bohannan, J. Phys. Chem. B 106 (2002) 4027.

[29] H. Pan, B. Liu, J. Yi, C. Poh, S. Lim, J. Ding, Y. Feng, C. H. A. Huan, J. Lin, J. Phys. Chem. B 109 (2005) 3094.

[30] E. Budevski, G. Staikov, W. Lorenz, J. Electrochemical Phase Formation and Growth: An introduction to the initial stage of metal deposition, VCH: New York, 1996 (Chapter 6).

[31] N. J. Gerein, J. A. Haber, J. Phys. Chem. B 109 (2005) 17372.

PAPER # 2: SYNTHETIC HIERARCHICAL NANOSTRUCUTRES: GROWTH OF CARBON NANOFIBERS ON MICROFIBERS BY CHEMICAL VAPOR DEPOSITION

ABSTRACT

Hierarchical structures were synthesized by thermally decomposing acetylene to grow carbon nanofibers (CNFs) on carbon microfibers and glass microfibers using catalytic chemical vapor deposition. A sulfonated silane intermediary was used to uniformly disperse Ni-Co (1:1) catalysts on the microfibers. The CNFs were grown on glass microfibers and carbon microfibers at 600 ^{o}C and 800 ^{o}C, respectively. An acetylene and nitrogen mixture (volume ratio 1:9) was used as a carbon source. The nanofiber morphology and structure were analyzed by scanning electron microscopy and high resolution transmission electron microscopy. As-prepared CNFs grown on both substrates typically have two types of morphology, coil-like with no distinct orientation and relatively straight and long CNFs. The diameter of CNFs on carbon fibers is 176 ± 5.8 nm compared to 71.82 ± 26.38 nm on glass fibers. CNFs grow more densely on carbon microfibers than on glass microfibers, which is affected by different surface chemistry and growth temperature. This hierarchical nanostructure with CNFs anchored to the carbon fibers and/or glass fibers offers a method to integrate nanoscale entities with materials or devices with larger length scales and may find applications as electrodes in fuel cells, sensors, supports for catalysts, and reinforcing components for composite materials.

1. Introduction

Carbon nanostructures have emerged as a new and attractive class of materials with unique electrical, mechanical, physical, and chemical properties [1,2]. They are actively studied for applications such as nanoelectronic devices [3-5], Li battery electrode material [6], field emission displays [7], storage materials for hydrogen and other gases [8], and probe tips

for atomic force microscopy (AFM) [9]. A lot of research work has focused on carbon nanotube (CNT) preparation techniques [10-14], theoretical simulation to understanding the physics of carbon nanostructures [15-18], and CNT post-treatments such as purification, thermal annealing, and surface modification [19-21]. However, the effective integration of carbon nanostructures with materials and devices of larger length scales to fully exploit the benefit of carbon nanostructures remains a major obstacle. Synthesis of hierarchical structures by anchoring carbon nanostructures to micron-scaled substrates offers a straightforward pathway to connect the nanostructures to the higher hierarchy.

In addition, the carbon-based hierarchical structures are expected to provide advantageous properties for many applications. For example, as catalyst support of Pt particles for proton exchange membrane fuel cells, they may improve the Pt utilization by securing the electronic route from Pt to the supporting electrode [22]. Thostenson demonstrated that by covering individual carbon fibers (CFs) with a sheath of CNTs and embedding this structure in a polymer matrix, the nanocomposite reinforcement resulted in local stiffening near the fiber/matrix interface and improved the interfacial shear strength [23]. S. Lim et al grew carbon nanofibers (CNFs) on activated CFs and used this composite to improve the efficiency of SO_x and NO_x removal [24]. Similar carbon hierarchical structures were studied for drinking water purification by selective chemisorptions of chromate and heteropolymolybdate [25].

Catalytic chemical vapor deposition (CCVD) is a popular fabrication method to synthesize carbon nanostructures. It is known that the properties of synthesized carbon materials, such as surface structure, morphology (fibers or tubes), diameter, length, shape, and texture, can be varied by controlling the catalyst precursor and synthesis parameters including the temperature schedule, carbon source, and gas flow rate [26]. CCVD has been successfully employed to grow CNTs and CNFs on many planar substrates such as silicon, silica and alumina [27-30]. More recently, a few studies on growing CNTs or CNFs on substrates with micron-scaled features including carbon paper, steel mesh, and primary CNTs by CCVD for various purposes have been reported [31-34].

In the present work, we demonstrate successful CNF growth on individual carbon microfibers as well as individual glass microfibers by CCVD technique. The growth

41

conditions and their influence on the nanofiber morphology are discussed. As-grown three-dimensional carbon-carbon and carbon-glass hierarchical structures may find applications in electrodes for fuel cells, sensors, supports for catalysts, and reinforcing components for composite materials.

2. Experimental

2.1 Synthesis of CNFs

CNFs were synthesized by decomposing acetylene on catalytic Co/Ni particles deposited on the CF fabrics (Ernest F. Fullam Inc., Latham, New York) or glass fibers (GFs) (Corning Inc., Corning, New York). The fabrication process is depicted in Fig. 1.
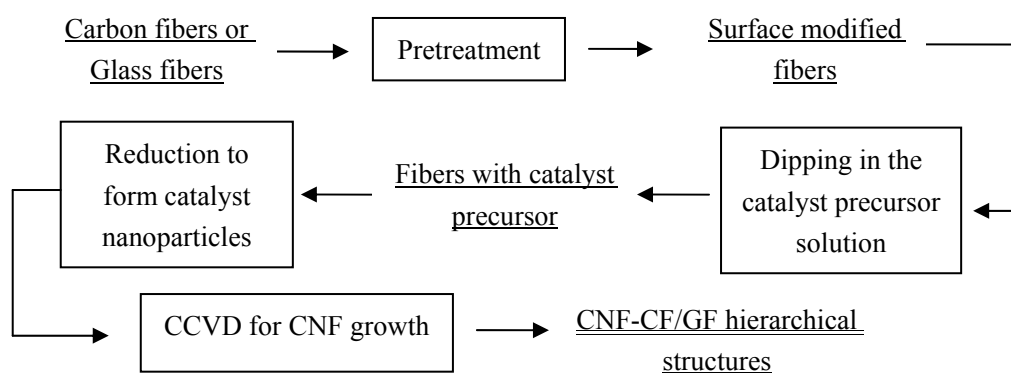
Fig. 1 The fabrication of hierarchical CNF-CF/GF structures.

As shown in Fig. 1, prior to catalyst deposition, the CFs and GFs were pre-treated by immersing them in ethanol for 30 min. This treatment helps to improve the homogeneity of the catalytic Co/Ni particle size on the fibers [32]. Ni-Co catalysts were then deposited by solution dipping. First, 2(4-chlorosulfonylphenyl) ethyl trichlorosilane 50 vol% in dichloromethane (United Chemical Technologies) was diluted by 6 vol% water in ethanol to obtain a final silane concentration of 1 vol% [35]. This solution was stirred for 2 hours at room temperature. Then Co and Ni sulfates with a 1:1 molar ratio were added to the solution and stirred for another 30 min. to form a saturated solution. CFs and GFs were soaked in the catalyst solution for 10 sconds to load the catalyst precursor. The extra solution on the fibers was wiped off with a lint free tissue.

After the CFs and GFs were loaded with the catalyst precursor, they were placed in a ceramic boat and loaded into the center of the CVD chamber. CNFs were grown by CCVD.

The samples were first heated in Ar to 400 $^{\circ}$C at a rate of 10 $^{\circ}$C min^{-1} and kept at 400 $^{\circ}$C for 10 min to decompose the sulfonated silanes. Then the catalyst precursors were reduced at 550 $^{\circ}$C for 2.5 min by carbon monoxide to obtain metallic catalyst nanoparticles. After catalyst reduction, the system was heated in Ar up to 600 $^{\circ}$C and 800 $^{\circ}$C for GFs and CFs, respectively. CNFs were grown by pyrolysis of 10 vol% acetylene in N_2 at those high temperatures for 5 min. Finally, the system was cooled to room temperature in an Ar atmosphere.

2.2 Characterization

The morphology of the as-prepared hierarchical structure was observed by a field emission scanning electron microscope (FE-SEM, JOEL LEO 982) operated at 5 keV. The microstructures of the CNFs was characterized by a high-resolution transmission electron microscope (HRTEM, JOEL, JEM2100) operated at 200 kV. The specimens for the TEM analysis were prepared by dispersing the samples in ethanol using ultrasonic treatment at room temperature. The diameters of the CNFs on both microfiber substrates were obtained by using the image processing software of Image J to analyze the SEM images of CNFs at 40,000X magnification or higher [36]. The dimensions were determined by measuring the diameter at five different locations on each of ten randomly selected carbon nanofibers from every sample and the average and standard deviations were reported.

3. Results and discussion

3.1 Growth of CNFs on the CF surface

Fig. 2 shows the typical SEM images of the CFs before CNF growth and the as-prepared CNFs grown on the CFs. Clearly, the CF surface is covered by a dense layer of coil-like CNFs without any distinct orientation, which doubled the diameter of the CFs. Though the lack of orientation makes the length measurement difficult, the observed length of CNFs is at least tens of micrometers after 5-min growth, which suggests a high growth rate. Fig. 2c is a typical SEM image of as-prepared CNFs at higher magnification. Analysis by Image J shows that the mean diameter of the CNFs is 176 nm with a standard deviation of 5.8 nm. Thus the as-prepared CNFs are rather uniform in diameter, which implies uniform distribution of the catalyst particles on the carbon surfaces after the catalyst impregnation. Moreover, as shown in Fig. 2c, the surface of each single CNF is smooth. Amorphous carbon covering the CNF

surface [32] has not been observed in any of the CNFs, indicating that the selection of experimental conditions can be efficient to prevent amorphous carbon from forming.
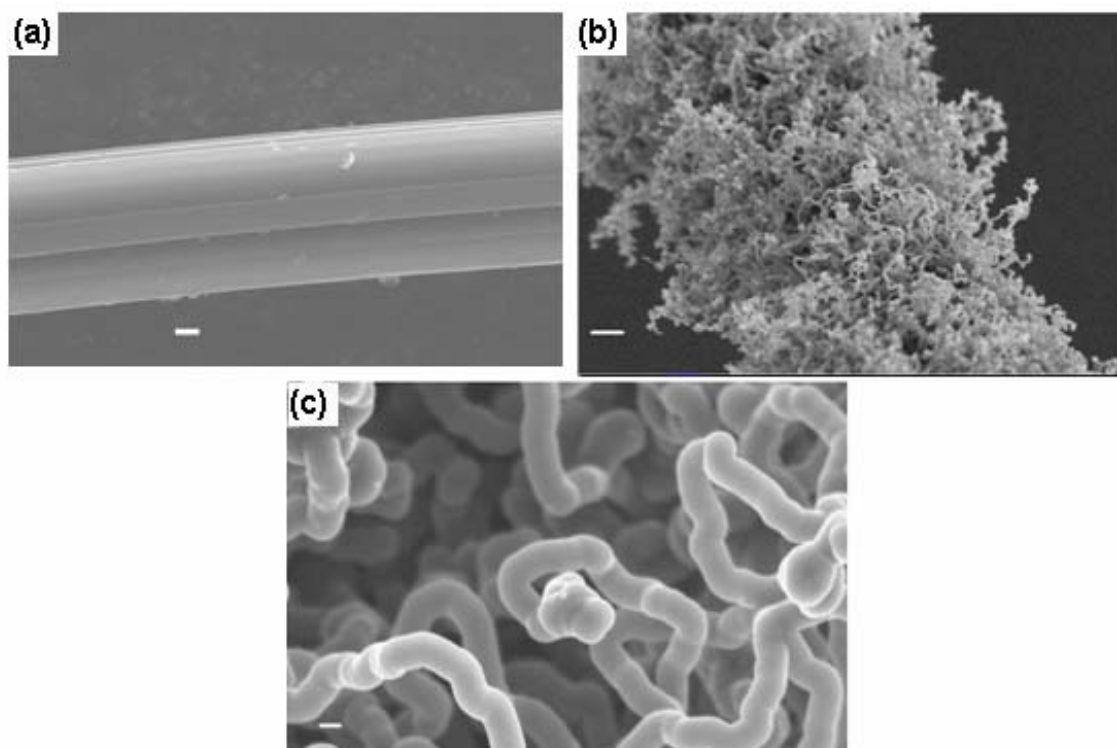

Fig. 2 (a) SEM image of CF before CNF growth, (b) and (c) SEM images of CNFs grown on the surface of CFs, scale bar: (a)1 μm, (b)2 μm, and (c)100 nm.

The CNFs were detached from the CF substrate and dispersed in the ethanol by 10-min sonication for the TEM study. Fig. 3 depicts the TEM images of CNFs grown on the surface of CFs. It confirms that there is no amorphous carbon on the surface of the as-prepared CNFs. In addition, it is interesting to note that the CNFs exhibit two different types of microstructures. In the first type, as shown in Fig. 3a and b, the spiral shaped twisted CNFs wind a lot without showing a distinct growth direction. Careful examination of Fig. 3 shows that the coiled CNFs are not well ordered and the graphite sheets exist in a distorted "herring-bone" arrangement, which is consistent to previous studies on CNFs of similar morphology [37,38]. In contrast, in the second type, as shown in Fig. 3c, fibers that are relatively straight and long without frequent direction change have been observed, which suggests a smooth growth process. An HRTEM image (Fig. 3d) shows that the nanofibers are better ordered than the coiled CNFs and the graphite sheets tend to be aligned in a direction parallel to the fiber growth axis.
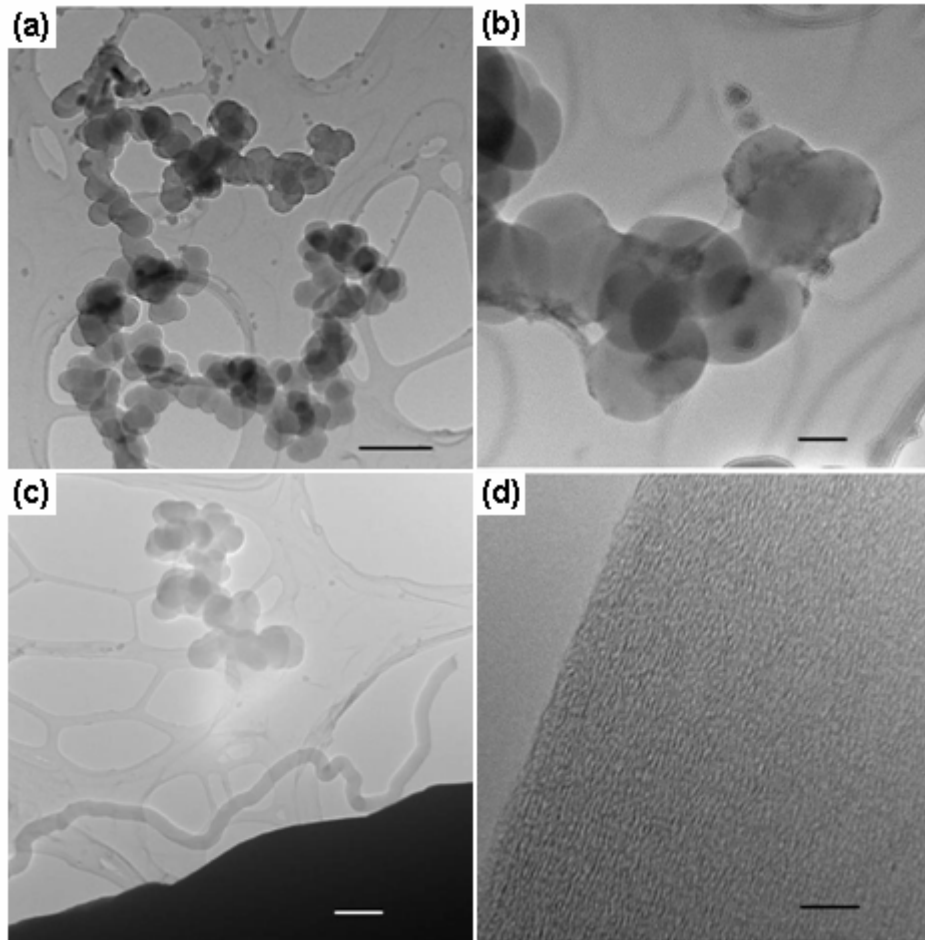
Fig. 3 TEM micrographs of carbon nanofibers grown on the surface of CFs with microstructure of (a), (b) type 1 and (c), (d) type 2, scale bar: (a) 500 nm, (b) 100 nm, (c) 500 nm, and (d) 5 nm.

According to the quasi-Vapor Liquid Solid (VLS) growth mechanism [26], CVD growth of CNFs involves the following steps: (1) carbon atoms are produced through acetylene decomposition; (2) the freshly formed carbon atoms near the catalyst particles immediately dissolve into the catalyst particles; (3) when saturation reaches within the catalyst particles, carbon in the form of graphite sheets precipitates along different precipitating planes of the catalyst particles to form CNFs. The arrangement of the graphite sheets in CNFs is generally believed to be controlled by the orientation of the precipitating planes of the metal particles.

A simplified model for the two different graphite sheet arrangements, i.e. parallel and herring-bone arrangements, is shown in Fig. 4. If carbon precipitates along a pair of adjacent planes at the same rates, straight herring-bone structured CNFs (Fig. 4a) will form with the graphite platelets aligned at an angle to the filament axis. If the graphite precipitates along the

lateral planes of the catalyst particles at the same rates, parallel structured CNFs (Fig. 4b)will be obtained with the platelets aligned in a direction parallel to the filament axis [39]. However, when the carbon precipitates along different planes of the catalyst particles at different rates, the CNF may bend to the direction with the lower precipitation rate. The growth direction of the CNFs changes during growth, producing the spiral shaped CNF structures (Fig. 4 c and d). Possible reasons causing varying deposition and precipitation rates for different catalyst planes include: (1) different catalytic ability for different crystal planes [40,41], (2) asymmetrical shaped catalyst particles which lead to different diffusion path lengths for the carbon atoms to traverse [42], and (3) a nonuniform carbon supply. In the current study, the coexistence of both distorted herring-bone and parallel nanofibers suggests a complex growth mechanism.
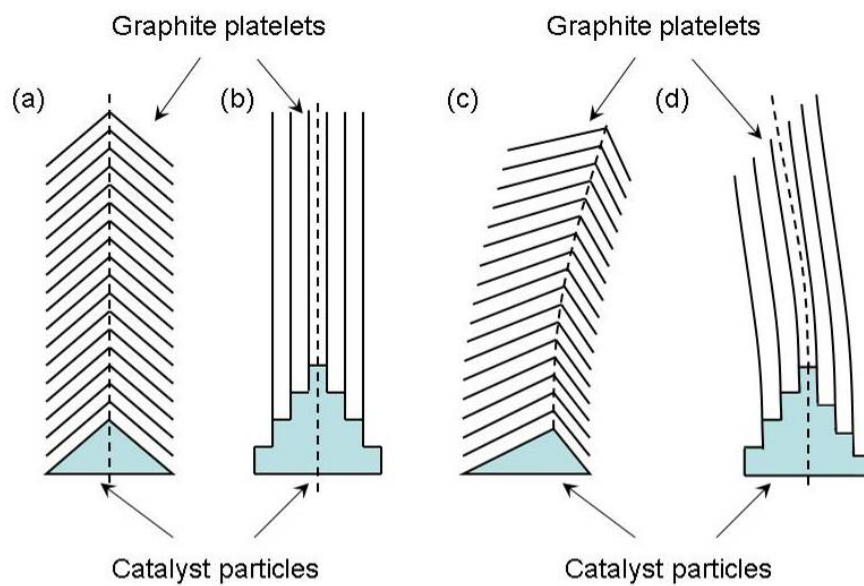

Fig. 4 Schematic of the structures of straight and distorted herring-bone (a, c) and parallel (b, d) type carbon nanofibers.

3.2 Growth of CNFs on the GF surface

To study how the change of surface chemistry will affect CNF growth, GFs were selected as a non-carbon substrate with micro-scaled features in our fabrication approach. GFs, one of the most versatile industrial materials, are widely used in the manufacture of structural composites, printed circuit boards, and a wide range of special-purpose products [43]. Since carbon nanostructures had previously been successfully grown on silica [44], we

chose to test the behavior of GFs as a CNF support. We adopted the same surface treatments and the same synthesis process as CF substrates except decreased the growth temperature to 600 °C to avoid the melting of glass.

Typical CNFs grown on the surface of GFs are shown in Fig. 5. CNFs also demonstrated two distinct types of morphology, e.g. the winded ones by pulsed growth and the straight ones by smooth growth. However, the layer of CNFs on GFs is less dense compared to the CNFs on CFs. As analyzed by Image J, the mean diameter of the CNFs is 71.82 nm with a standard deviation of 26.38 nm. Obviously, CNFs grown on the GFs are thinner and less uniform in size compared with the CNFs grown on carbon substrates. This implies smaller particle size and less uniform distribution of metal catalysts on the glass support due to different surface chemistry and a different growth temperature.
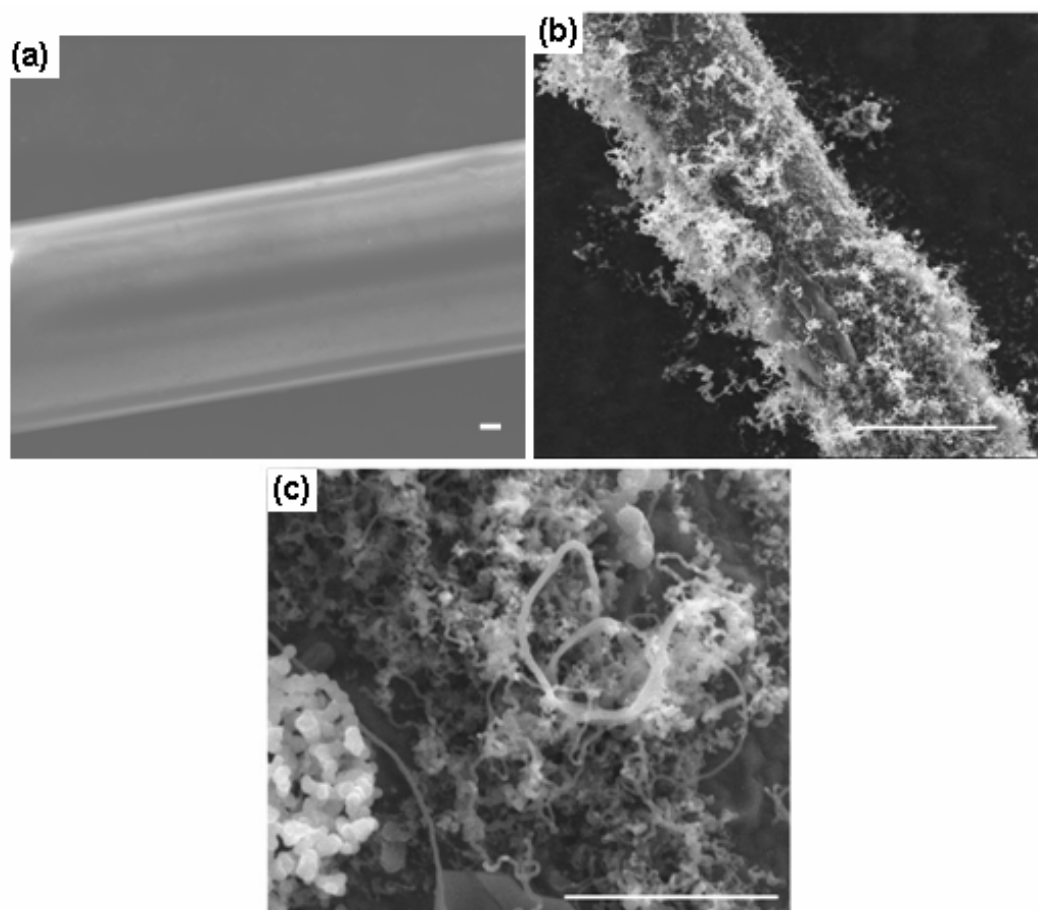

Fig. 5 (a) SEM image of GF before CNF growth, (b) and (c) SEM images of CNFs grown on the surface of GFs, scale bar: (a) 1 μm, (b) 10 μm, and (c) 2 μm.

We hypothesize that glass, consisting of more than 60% SiO_2, cannot effectively turn the

orientation of the CH$_3$ group in ethanol towards the glass surface to become more hydrophilic like carbon does during the pretreatment in ethanol [45]. Another reason may be the relatively weak catalytic effect of Ni-Co nanoparticles when they are on glass substrate. Though there is no report directly comparing impact of surface chemistry of carbon and glass, R.L. Vander Wal et al pointed out that Ni is far less catalytically active when supported on SiO$_2$ than supported on TiO$_2$ [28]. Moreover, silica may not serve as a negative charge donator to make a strong interaction between the Ni-Co alloy particles and the silica substrate.

4. Conclusions

In this article, we demonstrate the successful CNF growth on individual CFs and GFs to form a three-dimensional hierarchical structure using a CCVD technique. CNFs grown on both CFs and GFs demonstrated coexistence of two types of morphology. One is winded fibers implying frequent orientation change. The other one is relatively straight and long fibers with graphene sheets parallel to each other. This observation indicates the complex growth mechanisms. CNFs grown on CMF substrate appear to be thicker and more uniform than those on GMF substrates probably due to different catalyst-substrate interaction and different growth temperature. The as-grown three-dimensional carbon-carbon and carbon-glass hierarchical structures provide an effective means to connect nanoscale entities to the higher hierarchy. They may find applications in the fields of fuel cells, sensors, supports for catalysts, and reinforcing components for composite materials.

Reference

[1] H. Dai, J.H. Hafner, A.G. Rinzler, D.T. Colbert, R. Smalley, Nature 384 (1996) 147-150.

[2] L. Forro, C. Schnonenberger, in: M.S. Dresselhouse, G. Dresselhouse, P. Avouris (Eds), Carbon nanotubes: synthesis, structure, properties and application, Springer, New York, 2001.

[3] T. Hertel, R. Martel, P. Avouris, J. Phys. Chem. B 102 (1998) 910-915.

[4] C. Bower, W. Zhu, D. Shalom, D. Lopez, L.H. Chen, P.L. Gammel, S. Jin, Appl. Phys. Lett. 80 (2002) 3820-3822.

[5] K.B. Teo, M. Chhowalla, G.A. Amaratunga, W.I. Miline, P. Legagneux, G. Pirio, L. Gangloff, D. Pribat, V. Semet, V.T. Binh, W.H. Bruenger, J. Eichholz, H. Hanssen, D. Friendrich, S.B. Lee, D.G. Hasko, H. Ahmed, J. Vac. Sci. Technol. B 21 (2003) 693-697.

[6] B. Gao, A. Kleinhammes, X. Tang, C. Bower, L. Fleming, Y. Wu, O. Zhou, Chem. Phys. Lett. 307 (1999) 153-157.

[7] Y. Saito, K. Hamaguchi, K. Hata, K. Tohji, A. Kasuya, Y. Nishina, K. Uchida, Y. Tasaka, F. Ikazaki, M. Yumura, Ultramicroscopy 73 (1998) 1-6.

[8] G.E. Gadd, M. Blackfold, S. Moricca, N. Webb, P.J. Evans, A.M. Smith, G. Jacobsen, S. Leung, A. Day, Q. Hua, Science 277 (1997) 933-936.

[9] S.S. Wong, J. D. Harper, P.T. Lansbury, C.M. Lieber, J. Am. Chem. Soc. 120 (1998) 603-604.

[10] T.W. Ebbesen, P.M. Ajayan, Nature 358 (1992) 220–222.

[11] A. Thess, R. Lee, P. Nikolaev, H. Dai, P. Petit, J. Robert, C. Xu, Y.H. Lee, S.G. Kim, A.G. Rinzler, D.T. Colbert, G.E. Scuseria, D. Tomanek, J.E. Fischer, R.E. Smalley, Science 273 (1996) 483–487.

[12] H. Dai, in: M.S. Dresselhouse, G. Dresselhouse, P. Avouris (Eds), Carbon nanotubes: synthesis, structure, properties and application, Springer, New York, 2001, p. 29–54.

[13] F. Ren, Z.P. Huang, J.W. Xu, J.H. Wang, P. Bush, M.P. Siegal, P.N. Provencio, Science 282 (1998) 1105–1107.

[14] B.O. Boskovic, V. Stolojan, R.U.A. Khan, S. Haq, S.R.P. Silva, Nat. Mater. 1 (2002) 165–168.

[15] A. Maiti, J. Zelm, A. Svizhenko, M.P. Anantram, M. Panhuis, Phys. Status Solidi B233 (2002) 49-58.

[16] I. Efremenko, M. Sheintuch, Langmuir 21 (2005) 6282-6288.

[17] VI. A. Margulis, E.E. Muryumin, O.B. Tomilin, Physica B 353 (2004) 314-323.

[18] T. Natsuki, M. Endo, Carbon 42 (2004) 2147-2151.

[19] C. Li, H. Liu, S. Tseng, Y. Lin, S. Chen, J. Li, K. Wu, J. Juang, Diam. Relat. Mater. 15 (2006) 2010-2014.

[20] J. Han, S.H. Lee, A.S. Berdinsky, Y.W. Kim, J. Yoo, C. Park, J.J. Choi T. Jung, I.T. Han, J.M. Kim, Diam. Relat. Mater. 14 (2005) 1891-1896.

[21] S. Tzeng, K. Hung, T. Ko, Carbon 44 (2006) 859-865.

[22] C. Wang, M. Waje, X. Wang, J.M. Tang, R.C. Haddon, Y. Yan, Nano Lett. 4 (2004) 345-348.

[23] E.T. Thostenson, W.Z. Li, D.Z. Wang, Z.F. Ren. T.W. Chou, J. App. Phys. 91 (2002) 6034-6037.

[24] S. Lim, S. Yoon, Y. Shimizu, H. Jung, I. Mochida, Langmuir 20 (2004) 5559-5563.

[25] D.S. Su, X. Chen, G. Weinberg, A. Klein-Hofmann, O. Timpe, S.B.A. Hamid, R. Schlogl, Angew Chem. Int. Ed. 44 (2005) 5488-5492.

[26] K.P. Jong, J W. Geus, Catal. Rev. Sci. Eng. 42 (2000) 481-510.

[27] R.L. Ver Wal, T.M. Ticich, V.E. Curtis, Carbon 39 (2001) 2277-89.

[28] X.J. Dai, C. Skourtis, J. Appl. Phys. 103 (2008) 124305.

[29] J.M. Simmons, B.M. Nichols, M.S. Marcus, O.M. Castellini, R.J. Hamers, M.A. Eriksson, Small 7 (2006) 902-909.

[30] A. Cao, P.M. Ajayan, G. Ramanath, R. Baskaran, K. Turner, Appl. Phys. Lett. 84 (2004) 109-11.

[31] X. Sun, R. Li, B. Stansfield, J.P. Dodelet, S. Desilets, Chem. Phys. Lett. 394 (2004) 266–70.

[32] L. Qu, Y. Zhao, L. Dai, Small 8-9 (2006) 1052–1059.

[33] K. Otsuka, Y. Abe, N. Kanai, Y. Kobayashi, S. Takenaka, E. Tanabe, Carbon 42 (2004)727-736.

[34] W. Xia, X. Chen, S. Kundu, X. Wang, G .Grundmeier, Y. Wang, M. Bron, W. Schuhmann, M. Muhler, Surf. Coat. Tech. 201 (2007) 9232-9237.

[35] X. Sun, B. Stansfield, J.P. Dodelet, S. Desilets, Chem. Phys. Lett. 363 (2002) 415–421.

[36] http://rsb.info.nih.gov/ij/

[37] G. Zheng, K. Kouda, H. Sano, Y. Uchiyama, Y. Shi, H. Quan, Carbon 42 (2004) 635-640.

[38] O.C. Carneiro, N.M. Rodriguez, R.T.K. Baker, Carbon 43 (2005) 2389-2396.

[39] N. Krishnankutty, C. Park, N.M. Rodriguez, R.T.K. Baker, Cata. Today 37 (1997) 295-307.

[40] M. Kawaguchi, K. Nozaki, S. Motojima, H. Iwanaga, J. Crystal Growth 3-4 (1992) 309-313.

[41] Y. Wen, Z. Shen, Carbon 39 (2001) 2369-2386.

[42] S.P. Sharma, S.C. Lkkad, Surf. Coat. Tech. 203 (2009) 1329-1335.

[43] F.T. Wallenberger, Proc. Of the Norbert Kreidl Symposium (Triensberg, Liechtenstein),

1994, p 63-78.

[44] S. Takenaka, S. Kobayashi, H. Ogihara, K. Otsuka, J. Catal. 217 (2003) 79-87.

[45] X. Sun, R. Li, G. Lebrun, B. Stanfield, J.P. Dodelet, Int. J. Nanosci. 1 (2002) 223-234.

PAPER # 3: NOVEL GROWTH MORPHOLOGY OF CATHODICALLY ELECTRODEPOSITED Fe_3O_4 THIN FILMS

ABSTRACT

We report on the electrodeposition of Fe_3O_4 thin films in the Fe^{3+}-triethanolamine system by galvanostatic deposition. It was observed that both the deposition rate and the surface morphology of the Fe_3O_4 thin films were dependent upon the deposition temperature, Fe^{3+} ion concentration, and deposition time. Fe_3O_4 thin films deposited in electrolyte with high Fe^{3+} concentration at high temperature ($>80\ ^oC$) exhibited a dense and uniform morphology and were composed of globular or polyhedral crystallites, while the Fe_3O_4 deposited at low temperatures ($<70\ ^oC$) were loose and flake-like. Based on the empirical observations, a hypothetical growth mechanism is proposed.

Keywords: galvanostatic electrodeposition, Fe_3O_4, thin film, morphology, Fe^{3+}-triethanolamine complex.

Fe_3O_4 is the first known magnetic material and has been investigated extensively due to its technological applications in recording media, corrosion and catalysis. The renewed interests in Fe_3O_4 in past few years lie on its potential applications in magnetic memory and giant magnetoresistance (GMR) sensors [1-3]. More recently, Fe_3O_4 was studied as an electrode material for Li ion batteries because theoretically it can react with eight Li ions per formula unit at a potential of 1.5 V versus Li^+/Li^0 and thus have a high specific capacity [4-6].

Fe_3O_4 thin films have been grown on polycrystalline and single-crystal substrates by a variety of deposition techniques such as laser ablation [7-11], molecular beam epitaxy (MBE) [12-14], oxidizing Fe thin films [15-17], evaporation [18,19], and sputtering [20,21]. Although these vacumm-based methods provide good control over film thickness, morphology, crystallinity, and purity, they require costly equipment. Often the deposition involves prolonged evacuation of the vacuum system and heating of both the target and

substrate, which consumes considerable amounts of energy. The aqueous solution-based electrodeposition approach can be performed at a relatively low temperature and low cost, and is easy to control. Moreover, electrochemical deposition is a versatile process and can be used to fabricate not only Fe_3O_4 thin films, but Fe_3O_4 nanoparticles [22] and Fe_3O_4 nanowire arrays [23-25].

There are two basic approaches to grow Fe_3O_4 films by electrodeposition, i.e. anodic deposition in Fe^{2+} systems and cathodic deposition in Fe^{3+} systems. The majority of the previous work was conducted in the Fe^{2+} systems [23,24,26-30] where Fe^{2+} ion were complexed with organic compounds such as acetate anion and were electrochemically oxidized to form Fe_3O_4 in inert atmosphere at elevated temperature. A problem with this method is that the complexed Fe^{2+} tends to get oxidized by molecular oxygen in the air, so special attention must be paid to exclude molecular oxygen. Recently, based on the hydrothermal method by Sapieszko and Matijevic [31], cathodic reduction of Fe^{3+} complexed with triethanolamine (TEA) was proposed to deposit Fe_3O_4. In this approach, it is not necessary to eliminate molecular oxygen from the deposition environment [32]. This method was further used by J.M. Tarascon's group to fabricate Fe_3O_4 electrode for Li ion batteries [5,6]. However, no systematic study has been reported regarding factors affecting the Fe_3O_4 deposition in the Fe^{3+}-TEA system such as temperature, Fe^{3+}-TEA concentration, and time.

In addition, the morphology of electrodeposited Fe_3O_4 fabricated by different researchers is not consistent. Chung et al. reported a porous nano-sized cellular Fe_3O_4 thin film on a Pt substrate at room temperature [27]. Martinez et al. observed an adherent and homogeneous Fe_3O_4 film consisting of polyhedral crystals at 90 ^{o}C [29]. Magnetite deposits with particle size around 82 nm were obtained by Franger at room temperature [22]. Chatman et al. found that the electrolyte composition could change the magnetite morphology from angular crystallite to round and columnar crystallites at temperatures between 60 ^{o}C to 85 ^{o}C [28]. Globular, pyramidal, and needle-shaped morphologies were reported for Fe_3O_4 deposited at 60 ^{o}C to 90 ^{o}C [5,32]. Here we report a systematic investigation of the Fe_3O_4 deposition, the morphology and the deposition rate in the Fe^{3+}-TEA systems with Fe^{3+} concentration ranging from 0.02 M to 0.08 M at various temperatures. The microstructure and morphology of the Fe_3O_4 deposits were obtained using a field-emission gun scanning electron microscope

(SEM).

Experimental

Fe$_3$O$_4$ was deposited in an alkaline solution of Fe$_2$(SO$_4$)$_3$·5H$_2$O (Acros Organics, 97% purity) stabilized by TEA (Sigma Aldrich, reagent grade). NaOH (Fisher Scientific, A.C.S. grade) was used to adjust the pH value of the deposition bath. All chemicals were used without further purification. The solution was made by adding Fe^{3+} solution dropwise into a mixture of stirred TEA and NaOH solutions at 60 $^{\circ}$C. The compositions of the final solutions tested in this study before complexion reactions are given in Table 1.

Table 1. Composition of the investigated complex solutions

Solutions	C (Fe^{3+})/ mol l^{-1}	C (TEA)/ mol l^{-1}	C (NaOH)/ mol l^{-1}
1	0.02	0.1	1
2	0.04	0.1	1
3	0.06	0.1	1
4	0.07	0.1	1
5	0.08	0.1	1

Fe$_3$O$_4$ electrodeposition on Cu electrodes was performed galvanostatically at a current density of -5 mA cm^{-2} using a two-electrode set-up. A Keithley Model 228A served as the power source. The working electrode was a planar Cu disc (1.3 cm in diameter, from Yardney Lithion, Inc., used as received) with a geometric area of 1.33 cm^2. The Cu disc was cleaned with acetone, diluted HCl solution (1:9 in vol. ratio with water), and deionized (DI) water before deposition. The backside of the disc was insulated with nail polish. This nail polish coating was removed with acetone and isopropanol after deposition. The counter electrode was a graphite sheet. All the depositions were conducted with stirring in air unless otherwise specified. After rinsing the Fe$_3$O$_4$ deposits with DI water and drying them in air, the structure and morphology was characterized without further treatment. The weight of the deposited iron oxide films was measured by a METTLER H54AR Analytical Balance with an accuracy of 0.01 mg, and the deposition rates were estimated by measuring the weight of deposits per unit area as a function of time.

Fe$_3$O$_4$ thin films were examined using a Bruker axs D8 Focus X-ray diffractometer (XRD) and a JEOL JSM-7000F field-emission gun scanning electron microscope (SEM) equipped with Oxford INCA Energy 250 energy-dispersive X-ray spectrometer (EDS).

Results and discussion

Preparation of Fe^{3+}-TEA Solutions.— TEA has been used as a complexing agent for Fe^{2+} and Fe^{3+} ions for decades [33,34]. The poly-valent iron ions, which normally are converted into insoluble hydrated iron oxides in strongly alkaline solutions, tend to react with the basic TEA to form metal salts with liberation of water [34]. Both the pH value and the metal to ligand ratio are critical to forming a stable complex solution. In the present work, we kept the NaOH and TEA concentrations constant and employed solutions with Fe^{3+} concentrations that were varyied from 0.02 to 0.08 mol l^{-1}. When the Fe^{3+} concentration was less than 0.07 M, and Fe^{3+} solution was added dropwise to the NaOH and TEA solution mixture a small amount of local precipitation formed which eventually dissolved with stirring to give clear and pale greenish final solutions. However, when the Fe^{3+} concentration was increased to 0.08 M, a small amount of brown precipitate was observed in the final solution which did not dissolve even after stirring for several hours.

The effect of temperature and concentration on the deposition rate.— Fig. 1 shows the Fe$_3$O$_4$ deposition rates in different Fe^{3+} solutions at 60 $^{\rm o}$C and 80 $^{\rm o}$C, respectively. The depositions were carried out at a constant current density of -5 mA cm^{-2}. For all the deposition conditions tested, the weight gain per unit electrode area exhibits a good linear trend with respect to the deposition duration. The disposition rate is strongly affected by temperature. In solution 5, for instance, the deposition rate at 80 $^{\rm o}$C is more than two times greater than that at 60 $^{\rm o}$C.

As shown in Fig. 1, the deposition rate is strongly dependent on the Fe^{3+} ion concentration as well. At 80 $^{\rm o}$C, the minimum Fe^{3+} ion concentration is 0.02 M to obtain a considerable amount of Fe$_3$O$_4$ deposits. Above 0.02 M, more concentrated solutions result in greater deposition rates. In solution 5, which contains 0.08 M Fe^{3+}, the deposition rate is estimated to be 0.32 mg cm^{-2} min^{-1}, which is about two and three times greater than that in solutions containing 0.07 M and 0.04 M Fe^{3+} respectively. From this we can conclude that

high Fe^{3+} concentration and high deposition temperature are necessary to achieve fast Fe_3O_4 deposition, which is desirable for large-scale Fe_3O_4 deposition.
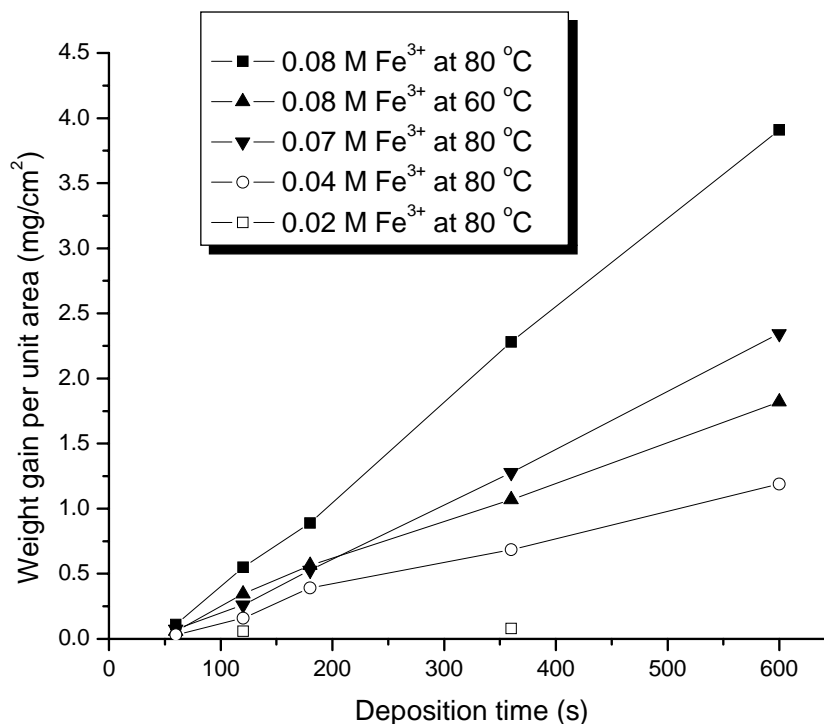

Fig. 1 The Fe_3O_4 deposition rates in different solutions at 60 ^{o}C and 80 ^{o}C.

The effect of temperature on the deposit morphology.— Fig. 2 demonstrates the morphology evolution of the Fe_3O_4 films deposited in solution 5 at a constant current of -5 mA cm^{-2} for 120 s at 60 ^{o}C, 70 ^{o}C, 80 ^{o}C, and 90 ^{o}C, respectively. Clearly, the morphology differs significantly at different deposition temperatures. The deposits at lower temperatures such as 60 ^{o}C and 70 ^{o}C are usually loose and have a flake-like morphology, while those at higher temperatures such as 80 ^{o}C and 90 ^{o}C are denser and have a particle-like morphology. Specifically, after 120 s deposition at 60 ^{o}C (Fig. 2a and b), a very thin layer of flake-like porous Fe_3O_4 film formed continuously and uniformly over the Cu substrate, which looks similar to the morphology of Fe_3O_4 films deposited on Pt substrates at room temperature by Chung et al [27]. When the deposition temperature was 70 ^{o}C (Fig. 2c and d), thicker but still loose deposits were obtained due to an increased deposition rate at a higher temperature. Severe cracking observed in Fig. 2c and d may be attributed to the shrinkage of the loose deposits during drying as suggested by other studies [35,36]. At 80 ^{o}C (Fig. 2e and f), globular particles began to form and the final deposits turned out to be dense and crack-free, and consisted of a mixture of flakes and particles. No flakes formed during deposition at 90

56

^{o}C (Fig. 2g and h), and the magnetite deposits exhibited well-defined crystal morphology with crystal size in the range of 100 nm to 500 nm. This trend of getting better-defined crystallites at higher deposition temperature agrees well with the previously reported morphology results [5,28,29,32].
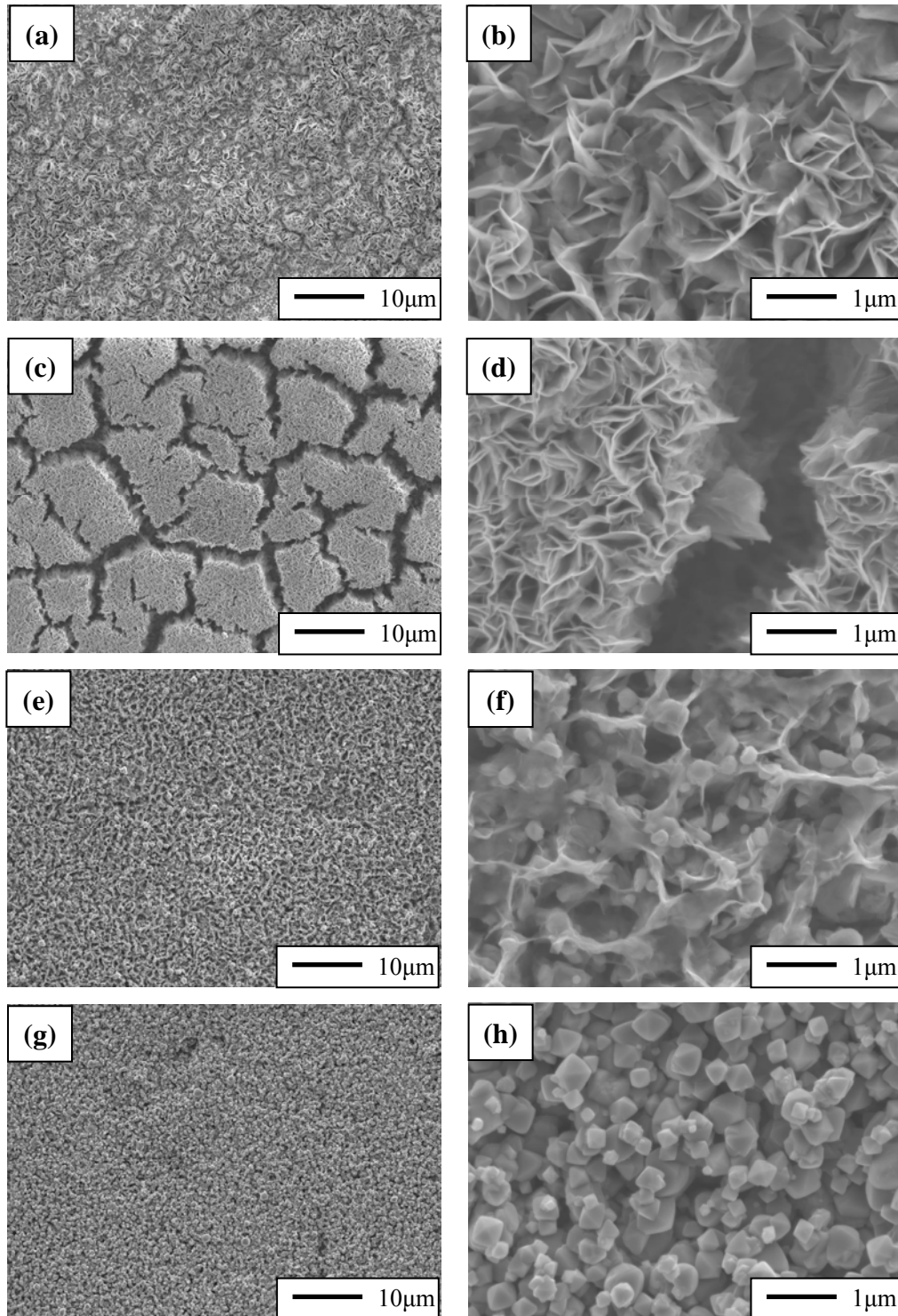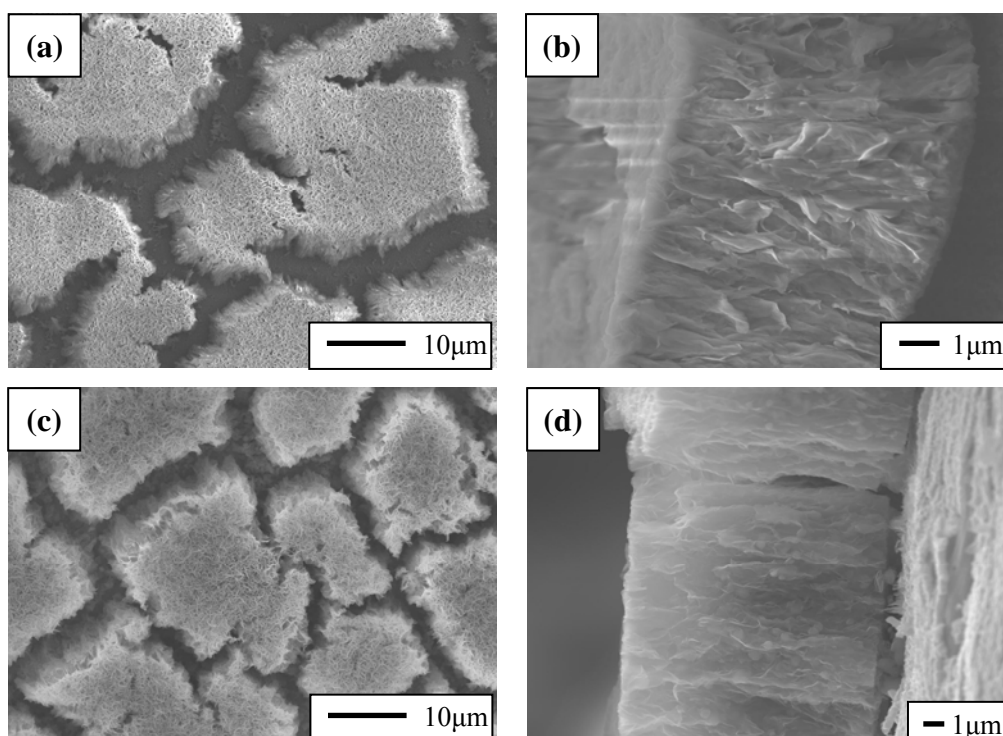

Fig. 2 SEM images of the Fe_3O_4 films deposited on the planar Cu substrates at (a), (b) 60 ^{o}C, (c), (d) 70 ^{o}C, (e), (f) 80 ^{o}C, and (g), (h) 90 ^{o}C. The films were deposited at a current density

The effect of deposition time on the deposit morphology.—The morphology of Fe$_3$O$_4$ films that resulted from extending the electrodeposition time to 360 s, is depicted in Fig 3. Fig. 3a and c show similar cracking morphology for the deposits obtained at 60 $^{\circ}$C and 70 $^{\circ}$C. At 60 $^{\circ}$C as the deposition time increased, cracks began to occur and the continuous film formed at the beginning of the deposition (Fig. 2a and b) was broken down into islands. Each of these islands looked similar and was composed of porous magnetite flakes as shown in Fig. 3b. When the deposition time was increased further to 720 s (morphology not shown), the cracking morphology stayed the same and the films got thicker. Cross-sectional views (Fig. 3b and d) indicated that the film synthesized at 70 $^{\circ}$C was about two times thicker than that at 60 $^{\circ}$C. Dense and crack-free deposits could only be obtained at higher temperatures. Fig. 3e and f together with Fig. 2g and h suggests that at 90 $^{\circ}$C, the morphology of the magnetite deposits remained unchanged as the deposition duration was increased from 120s to 360s and that the polyhedral Fe$_3$O$_4$ particles tended to grow as the deposition proceeded.

(e)

— 1μm

(f)

— 1μm
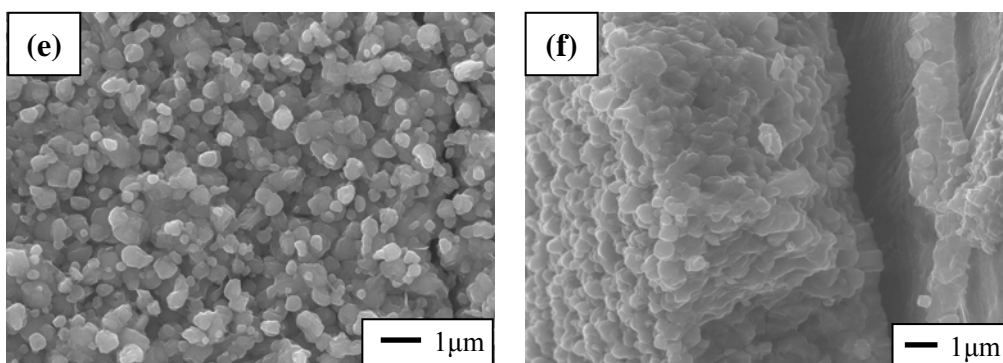
Fig. 3 SEM images of the Fe$_3$O$_4$ films deposited at (a) (b) 60 ^{o}C and at (c) (d) 70 ^{o}C, and (e) (f) 90 ^{o}C for 360s. The film was deposited at a current density of -5 mA cm^{-2} in solution 5.

The effect of the deposition duration on the morphology of the deposits in solution 5 at 80 ^{o}C and a constant current of -5 mA cm^{-2} was studied for up to 360 s. As shown in Fig. 4a and b, after 60 s deposition, a thin and continuous film is formed on the Cu substrate. The film is composed of Fe$_3$O$_4$ flakes with wall thickness of *ca.* 40 nm (Fig. 4a), and the thickness of the Fe$_3$O$_4$ film is *ca.* 1 μm (Fig. 4b). When the deposition duration is extended to 120 s (Fig. 2e and f) and 180 s (Fig. 4c and d), the deposits remained continuous and consisted of a mixture of flakes and particles. The cross-sectional view shown in Fig. 4d indicates that magnetite flakes only existed in the top layer of the film and the lower part of the film contained densely packed particles. When the deposition duration is prolonged to 360s as shown in Fig. 4e and f, the top layer of the flakes, marked as A, became relatively thin. Underneath this thin layer there was a layer of globular crystallites (B) with particle size up to 800 nm, and at the bottom (C) the small globular crystallites aggregated and grew into a more dense film with particle size larger than 1 μm.
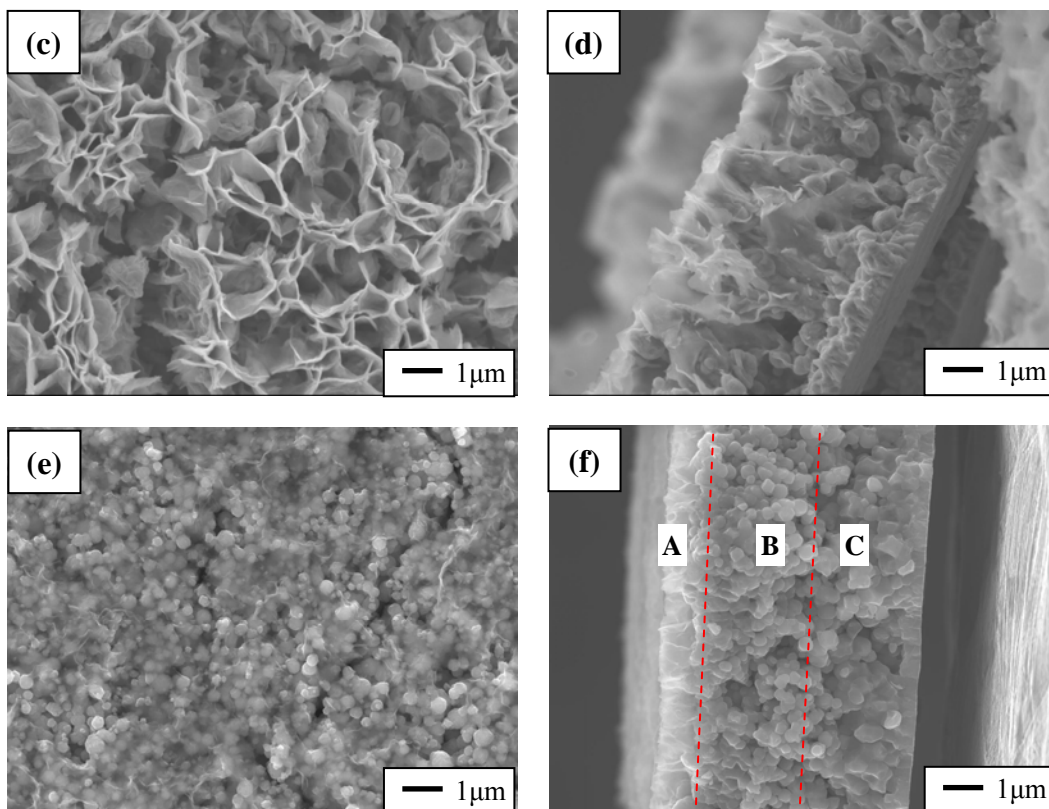

(a)

— 1μm

(b)

— 1μm
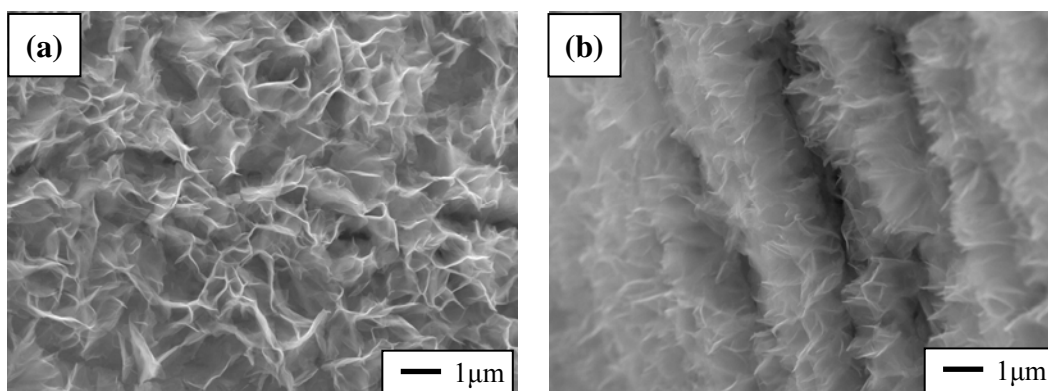
Fig. 4 SEM images of the Fe$_3$O$_4$ films deposited at 80 ^{o}C for different times. The films were deposited at a current density of -5 mA cm^{-2} in solution 5 for (a) (b) 60s, (c) (d) 180s, and (e) (f) 360s.

Microstructure study.— Fig. 5 summarizes the typical XRD patterns of the as-prepared Fe$_3$O$_4$ film deposited at a current density of -5 mA cm^{-2} for different durations in solution 5 at 80 ^{o}C. Obviously, the intensity of Fe$_3$O$_4$ diffraction peaks increased as the electrodeposition time increased from 60s to 600s. When the deposition time was 600 s in particular, the peaks other than the three peaks originating from the Cu substrate, match well with planes of (220), (311), (333), (440), and (533) of Fe$_3$O$_4$ (ICDD card No. 19-0629), with the (311) reflection being the strongest. The strong and sharp Fe$_3$O$_4$ peaks suggest good crystallinity of the Fe$_3$O$_4$ film deposited under the present conditions. To assess the degree of preferred orientation, peak intensities of the deposits were compared to those expected for a randomly ordered powder sample. This analysis suggests that there is minimal preferential orientation.
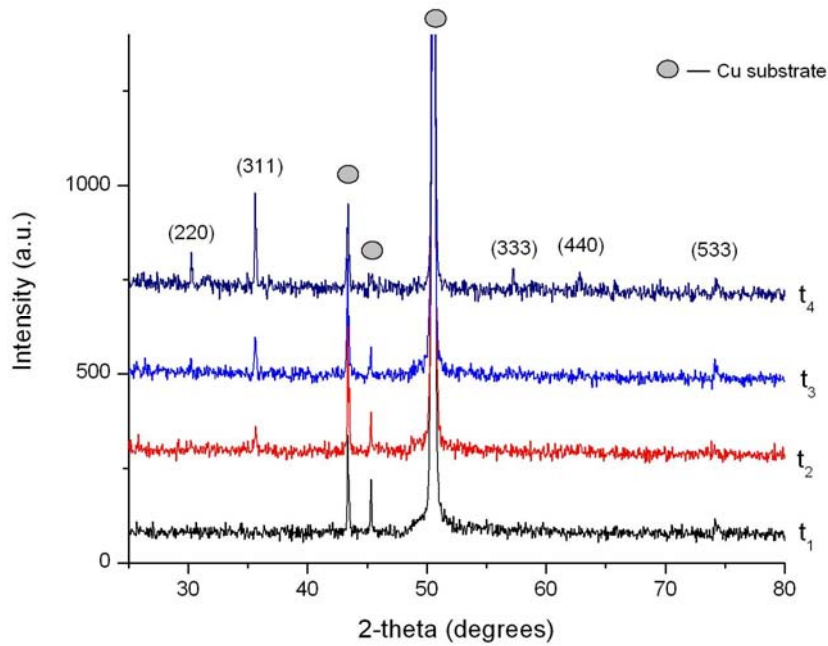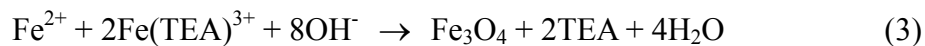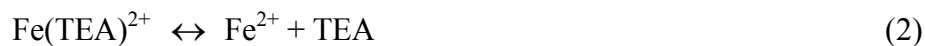
60

Fig. 5 XRD patterns of Fe3O4 electrodeposited on Cu plate for several deposition times at 80 $^{\circ}$C ($t_1 = 60$, $t_2 = 120$, $t_3 = 360$, and $t_4 = 600s$).

Growth mechanism speculation.— It is known that the electrodeposition of Fe_3O_4 in the current system includes two basic steps: (a) the electrochemical reduction of Fe^{3+}-TEA complex and (b) the chemical decomposition of Fe^{2+}-TEA and the precipitation of Fe_3O_4 as outlined in Eqs. (1)- (3) [32,36,37].

$$Fe(TEA)^{3+} + e^{-} \leftrightarrow Fe(TEA)^{2+} \tag{1}$$

$$Fe(TEA)^{2+} \leftrightarrow Fe^{2+} + TEA \tag{2}$$

$$Fe^{2+} + 2Fe(TEA)^{3+} + 8OH^{-} \rightarrow Fe_3O_4 + 2TEA + 4H_2O \tag{3}$$

Generally, the temperature affects the number of magnetite nuclei, ion activity, and ion diffusivity in both steps. In the current study, we observed that in addition to temperature the deposition time also affects the morphology of the thin film deposits

Based on the observations in this study and inspired by the structure-zone diagram by Thornton [38,39], the effect of temperature and time on the Fe_3O_4 growth in Fe^{3+}-TEA solutions is speculated and summarized in Fig. 6. At low temperatures such as 60 $^{\circ}$C and 70 $^{\circ}$C, the ion diffusion is insufficient and the resultant structure is dominated by open boundaries [39]. The deposit exhibits a flake-like loose structure and contains longitudinal porosity. With long deposition time, such a structure tends to shrink during sample drying and

forms islands as shown in Fig. 4a, c. At high temperature i.e. 90 ^{o}C, both the ion mobility and the number of magnetite nuclei are increased, and the structure appears to be determined by the preferential growth of favorably oriented crystal faces [39]. As a result, the deposited thin film transforms to dense and crack-free morphology with tightly packed well-faceted crystallites (Fig. 2g, h). As the deposition proceeds, the crystallites tend to aggregate and grow into particles with bigger particle size; the magnetite film becomes thicker but remains crack-free (Fig. 3e, f). At intermediate temperature such as 80 ^{o}C, loose flake-like deposits forming at the beginning of the deposition constitute the top layer, underneath which dense deposits consisting of globular particles form with long deposition time as shown in Fig. 4.
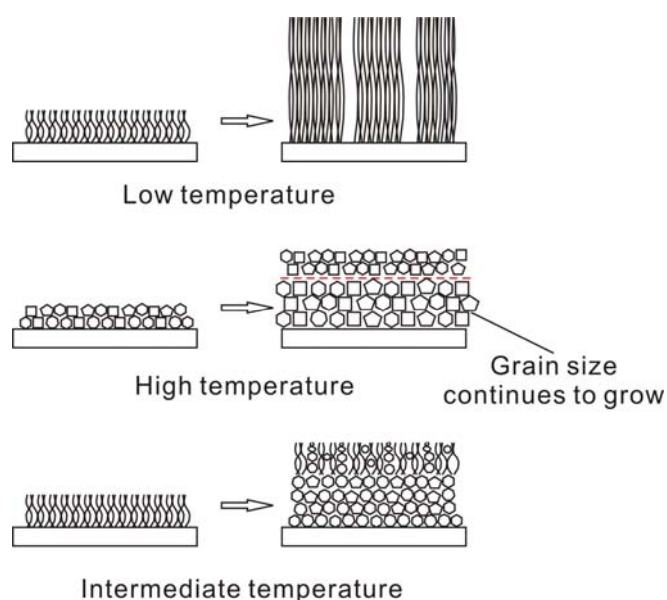
Fig. 6 Summary of Fe_3O_4 growth in the Fe^{3+}-TEA systems at different temperatures.

Conclusions

In this paper, we report the electrodeposition of Fe_3O_4 thin films in the Fe(III)-triethanolamine system. It was found that both temperature and Fe^{3+} ion concentration play an important role in the Fe_3O_4 deposition. Fe_3O_4 films prepared in electrolyte with high Fe^{3+} concentration at high temperature (>80 ^{o}C) had a dense and uniform morphology and were composed of globular or polyhedral crystallites, while the Fe_3O_4 deposited at low temperatures (<70 ^{o}C) were loose, amorphous, and flake-like. Prolonging deposition duration at low temperature leads to severe cracking, while prolonging deposition duration at high temperatures resulted in thick and dense magnetite deposit layers. XRD results indicated that

the magnetite film prepared at high temperature and in concentrated solution was well-crystallized. Electrodeposition techniques provide an easy and efficient way to fabricate high-quality Fe_3O_4 thin films.

Acknowledgement

References

[1] S. Soeya, J. Hayakawa, H. Takahashi, K. Ito, C. Yamamoto, A. Kida, H. Asano, and M. Matsui, *Appl. Phys. Lett.*, **80**, 823 (2002).

[2] Z. Zhang and S. Satpathy, *Phys. Rev. B*, **44**, 13319 (1991).

[3] V.I. Anisimov, I.S. Elfimov, N. Hamada, and K. Terakura, *Phys. Rev. B*, **54**, 4387 (1996).

[4] S. Ito, K. Nakaoka, M. Kawamura, K. Ui, K. Fujimoto, and N. Koura, *J. Power Source*, **146**, 319 (2005).

[5] S. Mitra, P. Poizot, A. Finke, and J.M. Tarascon, *Adv. Funt. Mater.*, **16**, 2281 (2006).

[6] P.L. Taberna, S. Mitra, P. Poizot, J.M. Tarascon, *Nature Mater.*, **5**, 567 (2006).

[7] G.Q. Gong, A. Gupta, G. Xiao, W. Qian, and V.P. Dravid, *Phys. Rev. B*, **56**, 5096 (1997).

[8] R. J. Kennedy and P. A. Stampe, *J. Phys. D*, **32**, 16 (2003).

[9] X.W. Li, A. Gupta, G. Xiao, and G.Q. Gong, *J. Appl. Phys.*, **83**, 7049 (1998).

[10] S.B. Ogale, K. Ghosh, r.P. Sharma, R.L. Greene, R.Ramesh, and T. Venkatesan, *Phys. Rev. B*, **57**, 7823 (1998).

[11] J. Tang, K.Y Wang, and W. Zhou, *J. Appl. Phys.*, **89**, 7690 (2001).

[12] J.F. Aanderson, M. Kuhn, U. Diebold, K. Shaw, P. Stoyanov, and D. Lind, *Phys. Rev. B*, **56**, 9902 (1997).

[13] K. A. Shaw, E. Lochner, and D. M. Lind, *J. Appl. Phys.*, **87**, 1727 (2000).

[14] R.F.C. Farrow, P.M. Rice, M.F. Toney, R.F. Marks, J.A. Hendstrom, R. Stephenson, M.J. Carey, and A.J. Kellock, *J. Appl. Phys.*, **93**, 5626 (2003).

[15] W. Weiss and M. Ritter, *Phys. Rev. B*, **59**, 5201 (1999).

[16] R.L. Kurtz, J. Karunamuni, and R.L. Stockbauer, *Phys. Rev. B*, **60**, 16342 (1999).

[17] Yueli Liu, Lei Liao, Chunu Pan, Jinchai Li, Ying Dai, and Wen Chen, *J. Phys. Chem. C*, **112**, 902 (2008).

[18] T. Furubayashi, *J. Appl. Phys.*, **93**, 8026 (2003).

[19] Chueh, M. Lai, J. Liang, L. Chou, and Z. Wang, *Adv. Funct. Mater.*, **16**, 2243 (2006).

[20] H. Liu, E. Y. Jiang, H. L. Bai, R. K. Zheng, and X. X. Zhang, *J. Phys. D*, **36**, 2950 (2003).

[21] S. Soeya, J. Hayakawa, H. Takahashi, K. Ito, C. Yamamoto, A. Kida, H. Asano, and M. Matsui, *Appl. Phys. Lett.*, **80**, 823 (2002).

[22] S. Franger, P. Berthet, J. Berthon, *J. Solid State Electrochem.*, **8**, 218 (2004).

[23] D. Carlier, C. Terrier, C. Arm, and J.-Ph. Ansermet, *Electrochem. Solid-State Lett.*, **8**, C43 (2005).

[24] C. Terrier, M. Abid, C. Arm, S. Serrano-Guisan, L. Gravier, and J.-Ph. Ansermet, *J. Appl. Phys.*, **98**, 086102 (2005).

[25] D. S. Xue, L. Y. Zhang, A. B. Gui, X. F. Xu, *Appl. Phys. A*, **80**, 439 (2005).

[26] M. P. Nikiforov, A. A. Vertegel, M. G. Shumsky, and J. A. Switzer, *Adv. Mater.*, **12**, 1351 (2000).

[27] K. W. Chung, K. B. Kim, S-H. Han, and H. Lee, Electrochem. *Solid-State Lett.*, **8**, A259 (2005).

[28] S. Chatman, A. J. Noel, and K. M. Poduska, *J. Appl. Phys.*, **98**, 113902 (2005).

[29] L. Martinez, D. Leinen, F. Martin, M. Gabas, J. R. Ramos-Barrado, E. Quagliata, and E. A. Dalchiele, *J. Electrochem. Soc.*, **154**, D126 (2007).

[30] C. L. Teng and M. P. Ryan, *Electrochem. Solid-State Lett.*, **10**, D108 (2007).

[31] R. S. Sapieszko and E. Matijevic, *J. Colloid Interface Sci.*, **74**, 405 (1980).

[32] H.M. Kothari, E.A. Kulp, S.J. Limmer, P. Poizot, E.W. Bohannan, and J.A. Switzer, *J. Mater. Res.*, **21**, 293 (2006).

[33] D.S. Polcyn and I. Shain, *Anal. Chem.*, **38**, 376 (1966).

[34] F.C. Bersworth, Patent 2544649, Mar. **13**, (1951).

[35] J. Georgieva, S. Armyanov, E. Valova, I. Poulios, S. Sotiropoulos, *Electrochem. Acta,* **51**, 2076 (2006).

[36] I. Zhitomirski, L. Gal-Or, A. Khon, M.D. Spang, *J. Mater. Sci.* **32**, 803 (1997).

[37] Thornton J.A., *J. Vac. Sci. Technol.* **11**, 666 (1974).

[38] Thornton J.A., *J. Vac. Sci. Technol.* **12**, 830 (1975).

PAPER # 4: STUDY OF Fe$_3$O$_4$-BASED Cu NANOSTRUCUTRED ELECTRODE FOR Li-ION BATTERY

ABSTRACT

Fe$_3$O$_4$-based Cu nanostructured electrodes for Li-ion cells are fabricated by a two-step electrochemical process. Cu-nanorod arrays acting as current collectors are first prepared on a thin copper disk by alumina template assisted electrodeposition. The active material of Fe$_3$O$_4$ is electrochemically deposited onto Cu nanorod arrays by potentiostatic deposition. X-ray diffraction identifies textured growth for both the Cu nanorods and Fe$_3$O$_4$. Scanning electron microscopic observation further reveals that the active material are deposited between Cu nanorods, and a 30 second deposition of Fe$_3$O$_4$ is sufficient to fill up the inter-rod space under the currently employed conditions. Longer electroplating time leads to the coalescence of Fe$_3$O$_4$ particles and the formation of bulky Fe$_3$O$_4$ islands on the top of the Cu nanorods. Electrochemical properties of the nanostructured electrodes are studied by conventional charge/discharge tests. The results show that the rate capabilities of the nanostructured electrodes are better compared to those of the planar electrodes and the coalescence of Fe$_3$O$_4$ particles is detrimental to achieve sustained reversible capacities.

1. Introduction

Developing Li-ion batteries with high specific capacities and high current densities as power sources for many applications is of great interest [1-6]. It is now well accepted that the limitations in the rate capability of Li-ion batteries are mainly caused by slow solid-state diffusion of Li ions in the electrode materials [7,8]. Nanostructured materials are considered as active candidates to tackle the problem because of the potential advantages they offer, such as [9-11]: (i) short Li ion transport length due to small particle sizes; (ii) fast surface reaction resulting from large electrode/electrolyte interface area; (iii) good accommodation of structure strains imposed by electrochemical reactions; and (iv) possibility of operation in systems with low electronic conductivity due to short path lengths for electron transport.

However, there are two major obstacles associated with nanostructured electrodes [10]. First, the increased electrode/electrolyte interface area leads to significant undesirable electrode/electrolyte side reactions, safety concerns and poor calendar life; second, the lack of control over the synthesis process and high expense to fabricate the electrode hinder the progress towards large scale production. To address the problem of side reactions with the electrolyte, a promising approach is to choose materials which fall within the stability window of the electrolyte or at least limit the formation of the solid-electrolyte interface layer, such as Fe_3O_4 (1.6 V versus Li^+(1M)/Li) [12], $Li_{4+x}Ti_5O_{12}$ (0<x<3, 1.6V versus Li^+(1M)/Li) [10], and $Li_{0.91}TiO_2$-B (1.5-1.6 V versus Li^+(1M)/Li) [13].

Fe_3O_4 is among a group of metal oxides that demonstrate a novel reactivity mechanism, the so called "conversion reaction", as summarized in Eq. 1

$$M_xO_y + 2y\ e^- + 2y\ Li^+ \leftrightarrow x\ M^0 + y\ Li_2O \qquad\qquad (1)$$
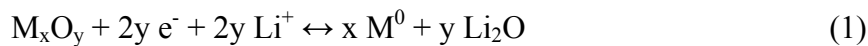
where M is a transition metal. This mechanism differs from the classical Li insertion/deinsertion process or Li-alloying reactions [1,12,18]. The use of Fe_3O_4 anode material reduces the overall cell voltage. But due to the high potential against lithium, side reactions with the electrolyte are minimized. Fe_3O_4 has a theoretical capacity around 928 mAh g^{-1} by assuming the reduction of Fe^{3+} and Fe^{2+} to Fe^0 during Li ion intercalation, which is about three times that of commonly used graphitic carbons [12,21]. At room temperature the inverse spinel exhibits electronic conductivity as high as 2×10^4 S m^{-1} [14]. So it is considered as a good candidate for nanostructured anode materials with enhanced safety, good capacity retention on cycling, and low self-discharge. In addition, magnetite is one of the cheapest common oxides and an environmentally friendly product with very low toxicity.

Efforts of studying iron oxides as Li intercalation material can be traced back to the 1980s, with more emphasis on lithiation of α-Fe_2O_3 (hematite) and spinel Fe_3O_4 in both non-aqueous electrolytes and molten salts [15,16]. However, slow kinetics of Li ion intercalation/deintercalation among bulky iron oxides prevented further development. More recently, nanostructured hematite and magnetite attracted a lot of research interest as

candidate electrode materials [1,9,12,17,18,21]. Usually, nanosized iron oxides were fabricated by various means, mixed with conducting acetylene black or Super P carbon, and pressed on current collectors such as Ni mesh or Li foil [12,17] to form working electrodes. S. Mitra et al. [18] employed polished planar Cu disks as substrates for nanosized magnetite deposits through cathodic electrodeposition.

In this paper, we report our investigation of a new non-toxic nano-engineered electrode that is expected to shorten the Li ion diffusion length. Our two-step electrode design consisted of the anodic aluminum oxide (AAO) template-assisted growth of Cu nanorods onto Cu disks as nanostructured current collectors and the electrochemical deposition of Fe_3O_4 onto the nano-architectured electrodes. Using such electrodes, we demonstrated improvement in rate capability compared to planar electrodes and good capacity retention at high rates over large number of cycles [19]. Our results suggested that the existence of nanorod current collectors provided better current collector/active materials surface contact and helped maintain short diffusion length and accommodate structure strains imposed by electrode reactions.

2. Experimental
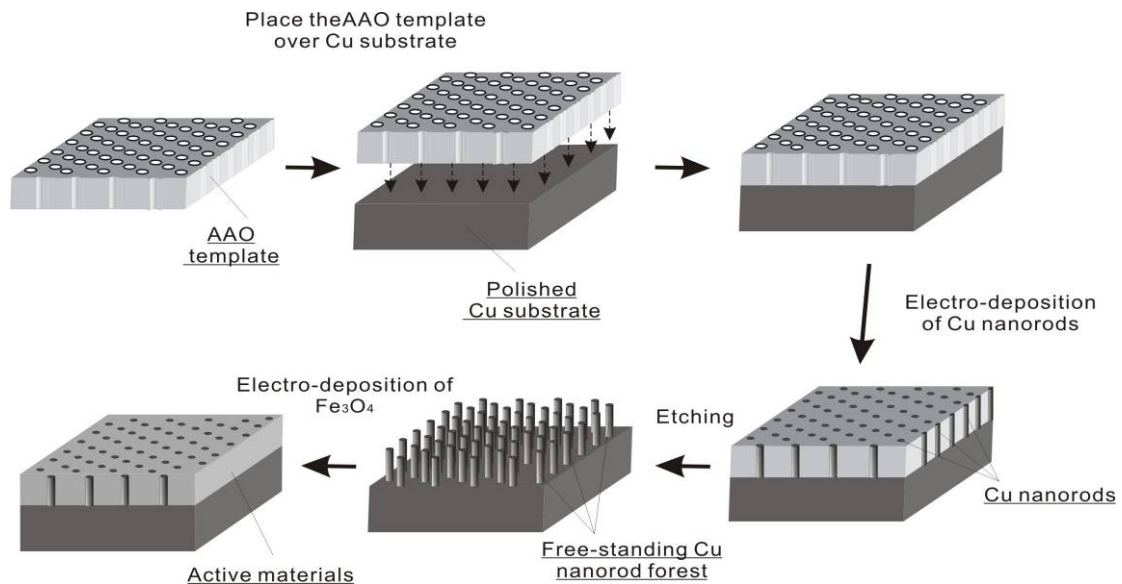
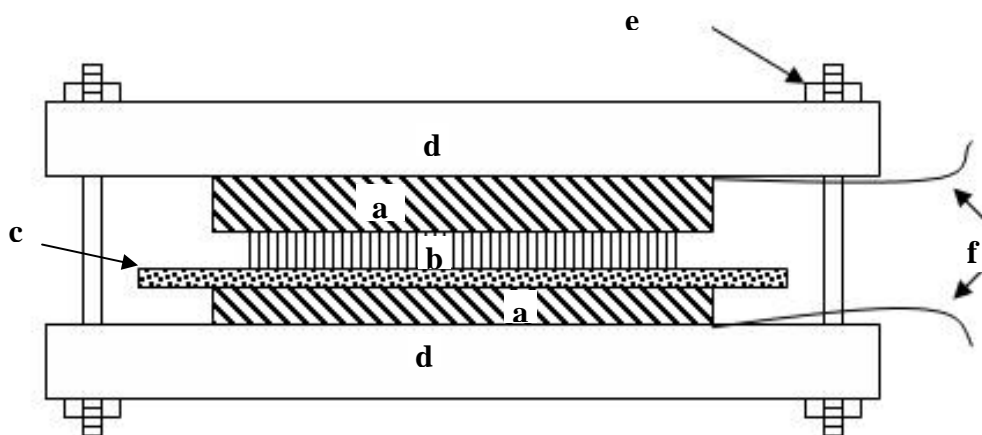**Fig. 1** Schematic of the fabrication of nanostructured electrode.

Fig. 2 Schematic of the cell for Cu nanorod electrodeposition.

(a)- copper plate, (b)- alumina template, (c)- cellulose membrane (separator), (d)- plastic

plate, (e)- bolt and nut, (f)- copper wire.

The fabrication process of Fe_3O_4 based Cu-nanostructured electrodes is schematically shown in Fig. 1. Key steps include (i) mechanical polishing of Cu substrates, (ii) fabrication of Cu nanorod arrays as current collectors, and (iii) electrochemical deposition of Fe_3O_4 onto the nanostructured current collectors. The key steps are described in more detail in the following sections.

2.1 Fabrication of Cu nanorod arrays as current collectors

Arrays of perpendicular Cu nanorods were fabricated by cathodic electrodeposition using a two electrode configuration shown in Fig. 2. Two pieces of Cu disks (1.3cm in diameter, from Yardney Lithion, Inc.) served as the cathode and the anode. Before electrodeposition, the cathode Cu disk was mechanically polished with 1.0 micron alpha alumina and 0.05 micron gamma alumina polishing slurries (Buehler micropolish), followed by rinsing with deionized (DI) water and ultrasonically cleaning in ethanol. Oxide removal was carried out in a dilute HCl solution (1:9 in vol. ratio with water). The AAO template (Whatman, Anodisc 13, Cat. No: 6809-7023) was 60-μm thick, with a maximum porosity between 25% and 50%, pore size of 200 nm, and a pore density of 10^{10} cm^{-2} [20]. A cellulose paper separator (Whatman, Cat. No: 1001042) was soaked with the electrolytic solution containing 100 g L^{-1} CuSO$_4$·5H$_2$O (Alfa Aesar), 20 g L^{-1} (NH$_4$)$_2$SO$_4$ (Alfa Aesar), and 80 mL L^{-1} Diethylenetriamine (DETA, Alfa

Aesar) [18]. The whole stack was kept under constant pressure by bolts and nuts. A Keithley Model 228A in a potentiostatic mode served as the power source.

The electrochemical depositions were carried out at 1.2 DC V at room temperature. After the electrodeposition, the cathodes were immersed in a 2M NaOH solution for 15 minutes to remove the AAO templates and cleaned in the dilute HCl solution to remove the surface oxides. The as-prepared samples are immediately used for Fe_3O_4 deposition to minimize the surface oxidation of the Cu nanorods.

2.2 Electrodeposition of Fe_3O_4

Fe_3O_4 was deposited on the Cu disks with Cu nanorod arrays by electrodeposition. The electrolyte consisted of 2 M NaOH (Alfa Aesar) and 0.09 M $Fe_2(SO_4)_3 \cdot 5H_2O$ (Alfa Aesar) complexed with 0.1 M tri-ethanol-amine (Acros Organics) at a pH value of 12.3 [18,21,22]. Electrodeposition was carried out in a two-electrode set-up at 1.5 V (DC) and 50˚C. The Cu disks with Cu nanorods served as the cathode and a graphite sheet served as the anode. After electrodeposition samples were rinsed with DI water and dried in air. Fe_3O_4 were also electrodeposited under the same conditions on mechanically polished planar Cu substrates to provide control samples.

2.3 Structure analysis and morphology characterization

The as-prepared nanostructured electrodes were examined by X-ray diffraction (XRD) using a REGAKU CN2182D5 diffractometer and scanning electron microscopy (SEM) using a JEOL JSM-840 microscope equipped with energy-dispersive X-ray spectroscopy (EDS).

2.4 Electrochemical tests

The electrochemical performance of our nanostructured electrodes was evaluated initially in coin cells. Coin/pouch half cells were constructed using metallic lithium as the counter electrodes and the nanostructured electrodes as the anodes under argon atmosphere inside a glove box. The half cells were cycled galvanostatically at a rate of C/20 and C/10, with C being defined as the full use of the capacity in 1 h. Full coin cells were fabricated

using both the nanostructured electrodes and the control samples as the anodes and the standard $LiNi_{0.8}Co_{0.2}O_2$ (Yardney Lithion, Inc.) material as the cathodes. The cathodes were prepared by coating a paste containing 89% $LiNi_{0.8}Co_{0.2}O_2$, 2% Super P, 2% KS-15 graphite, 2% Shawinigan Acetylene Black (SAB), and 5% Kynar in n-methylpyrrolidone (NMP) onto Al foil. The loading of the cathode material was 0.125 g in^{-2}. Setela of 20 μm in thickness was used as the separators. The standard electrolyte of 1M $LiPF_6$ (in ethylene carbonate (EC): dimethyl carbonate (DMC): diethyl carbonate (DEC)/1:1:1 in mass ratio) was used for both the half-cell and full-cell tests. The open circuit voltages of the fresh full cells were about 220 mV. The coin cells were cycled under constant current conditions at different rates in the range of 1/10C to 10C. The charge/discharge capacities and the capacity retention property of the anodes at different charge/discharge current densities were studied.

3. Results and discussion

3.1 Nanostructured Cu current collector fabrication

Cu nanorods were electrodeposited on the surface of the mechanically polished Cu disks through the pores of an AAO template. This template-assisted deposition approach offers multiple advantages. For example, it is convenient to obtain uniform and free-standing Cu nanorod arrays. In addition, the deposition is cost-efficient, easy to control, and easy to scale up.

The uniformity in height of the deposited Cu nanorod arrays is expected to be of critical importance to the performance of the nanostructured electrode. It is significantly affected by the flatness of the Cu substrates. Atomic force microscope (AFM) study confirmed that mechanical polishing efficiently reduced the surface roughness of Cu foil. The measured area root mean square (RMS) roughness decreased from the original 83.0 nm to 16.3 nm after polishing, which helped to ensure an intimate contact between the cathode Cu disks and the AAO templates under mechanical pressure and to obtain an even current distribution on the electrodes during electrodeposition.

The use of the porous cellulose separator soaked with the electrolytic solution provided a media for Cu ions to transfer from the anode to the cathode uniformly, which helped the Cu nanorods grow at the similar speed. Since the use of porous cellulose separator eliminated

electrolyte feeding, the process was greatly simplified and easy to control. The separator could also prevent short circuits, accommodate the mechanical constraints of the pressure applied to the stack, and eliminate undesirable electrolyte contamination.
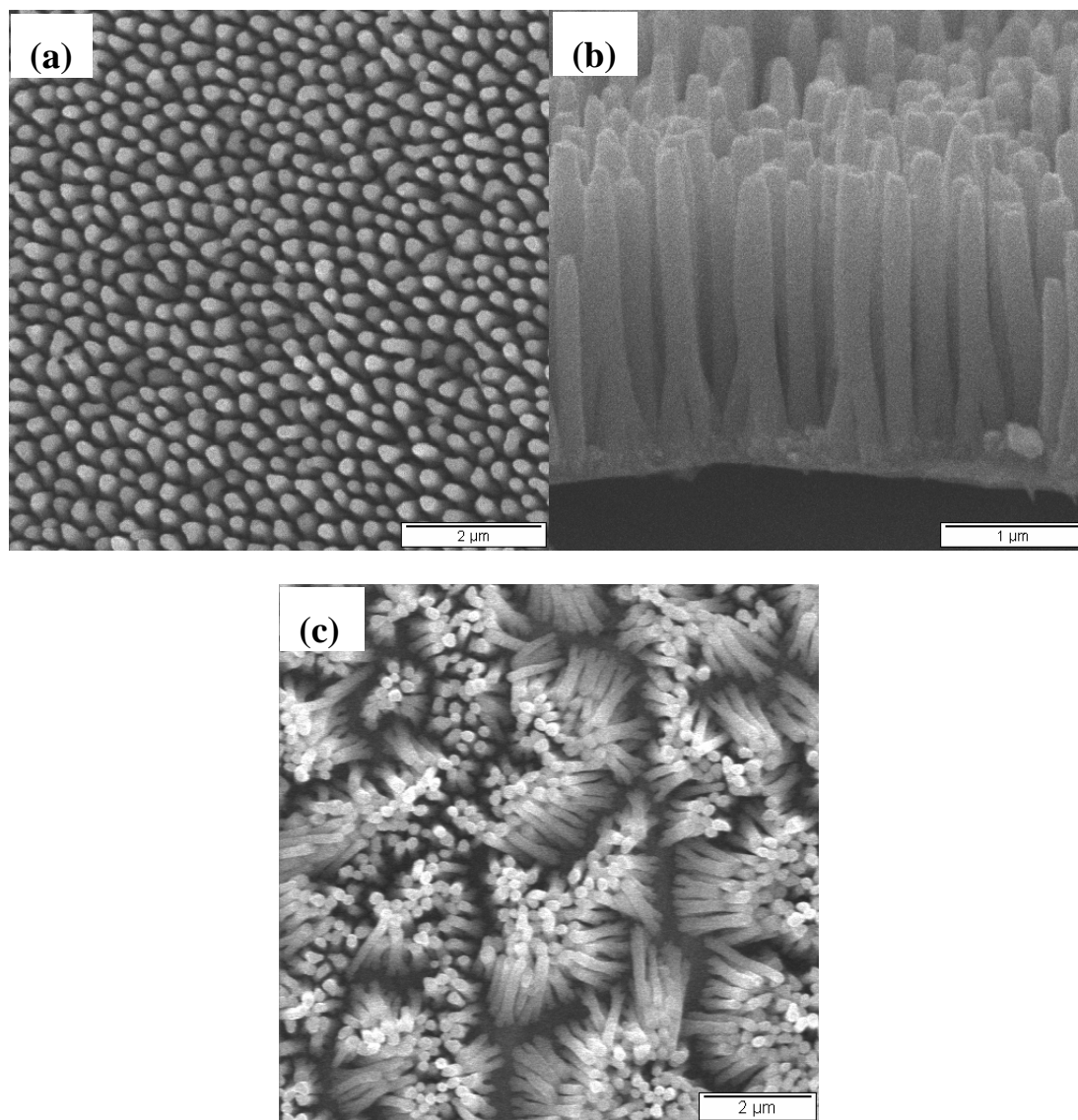

Fig. 3 SEM images of Cu nanorods grown on Cu substrate after removing the alumina template. (a) Top view and (b) cross-section view of Cu nanorod arrays after 5 min deposition; (c) aggregated Cu nanorods after 10 min deposition.

Fig. 3 shows typical SEM images of the Cu nanorod arrays with the AAO template fully removed. Fig. 3 (a) is the top-view image of the Cu nanorods by 5 minutes electrodeposition. It shows that the polished Cu substrate surface has been covered by uniform and free-standing copper nanorods with an average diameter of 200 nm for each individual nanorod. As confirmed by our previous studies [23,24], the size of Cu nanorods is defined by

the pore size of the AAO template. Fig. 3 (b) is the SEM images of the cross-section. In Fig. 3 (b), we can see that the nanorods are perpendicular to the substrate, their lengths are around 2 μm, and the inter-rod distance is less than 100 nm. The Cu nanorods tend to aggregate when the aspect ratio becomes large. For example, under the present deposition conditions, the nanorods began to aggregate when the deposition time was longer than 10 minutes as shown in Fig. 3 (c). Aggregation is detrimental to the subsequent loading of Fe_3O_4 because Fe_3O_4 particles tend to crystallize over the top of the Cu nanorod bundles instead of on the surface of individual Cu nanorods and lose the advantages provided by the nanostructrued current collectors.

3.2 Electrodeposition of Fe_3O_4
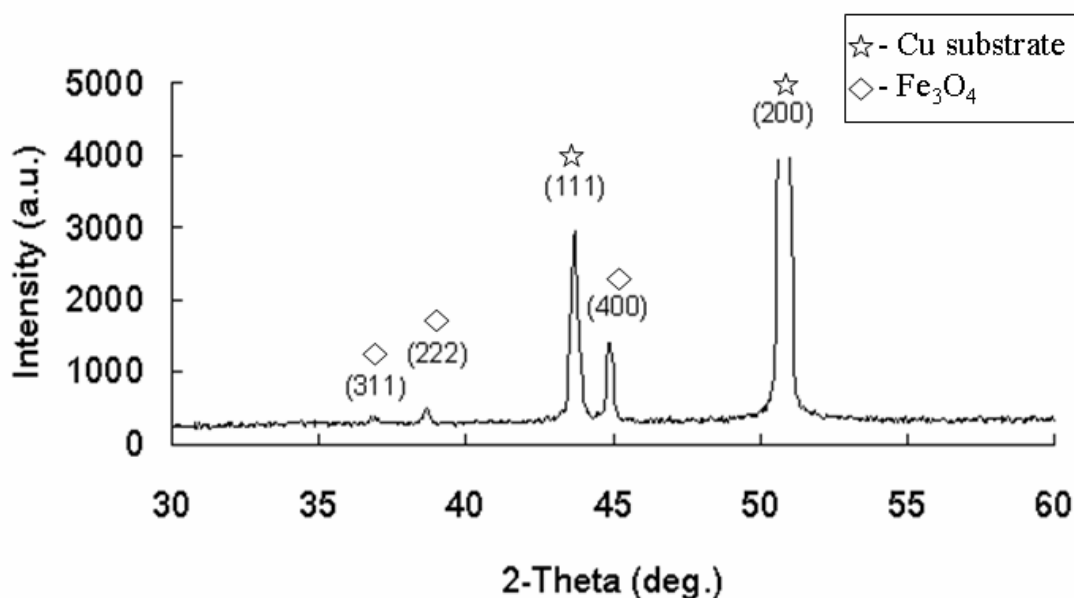
Fig. 4 XRD pattern of Fe_3O_4-Cu nanostructured electrode, star: metallic Cu, parallelogram: Fe_3O_4 deposit.

Fig. 4 is a typical XRD pattern from the as-prepared nanostructured electrodes. The two strong peaks at around 43.3˚ and 50.5˚ correspond to the Cu (111) and the Cu (200) reflections (International Centre for Diffraction Data card No. 04-0836), originating from the Cu substrate and the Cu nanorods. The Cu (200) reflection is much stronger than that of Cu (111), suggesting that the Cu substrate and the Cu nanorods are [100] textured. The three weak reflections can be assigned to (311), (222), and (400) of magnetite Fe_3O_4 phase (ICDD No.26-1136), with the (400) reflection the strongest. This indicates that the Fe_3O_4

nanoparticles are not randomly attached to the Cu nanorods, but showing preferred orientation.
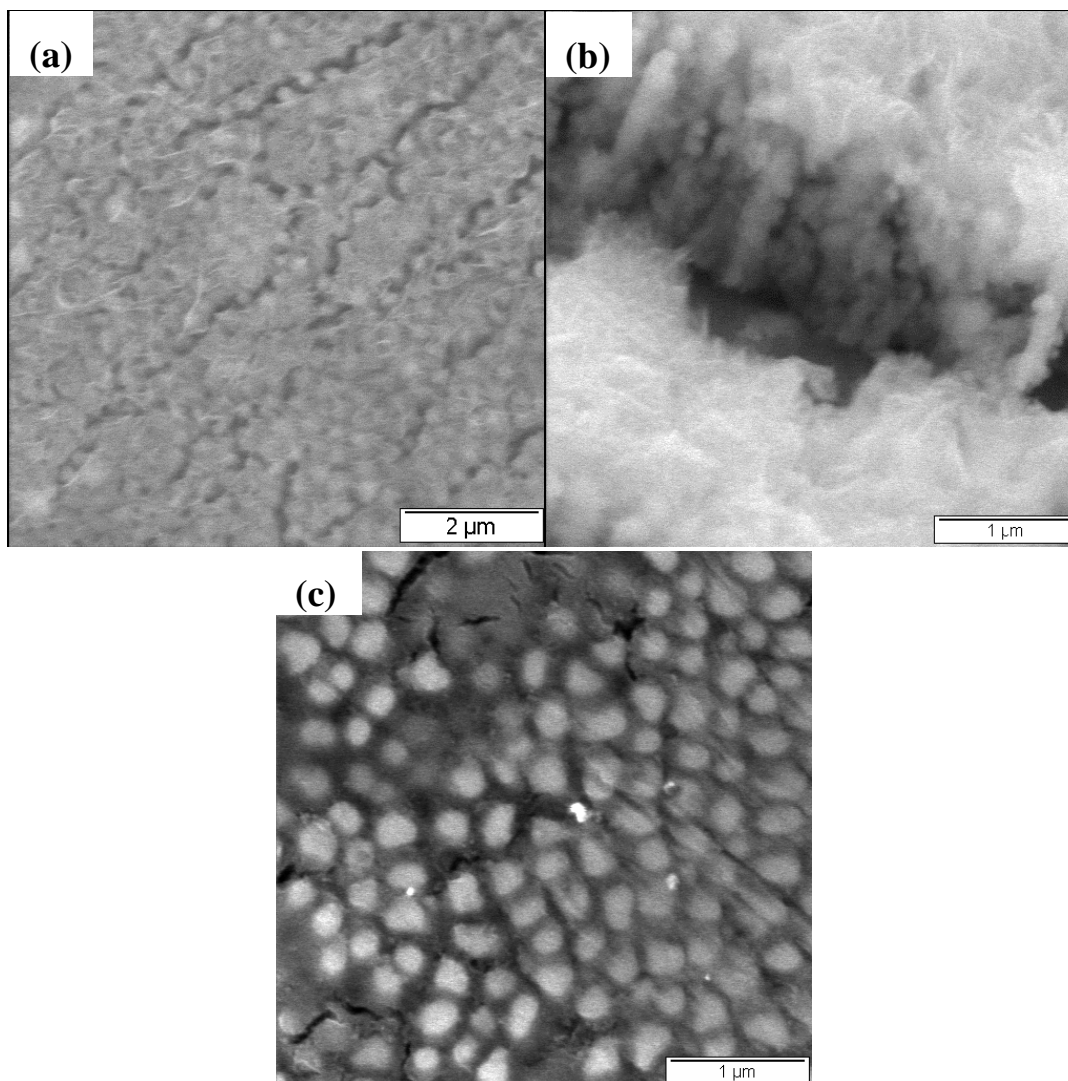

Fig. 5 SEM images of Fe_3O_4 deposit on Cu nanorods after 30 s electrodeposition: (a) top view, (b) oblique view, (c) same sample of (a) with top layer of Fe_3O_4 film removed.

Fig. 5 shows the SEM images of the nanostructured electrode after 30 s Fe_3O_4 deposition. Fig. 5 (a) and (b) clearly show that Fe_3O_4 filled up the spaces between the Cu nanorods and began to coalesce into a continuous thin layer on the top of the Cu nanorod arrays with small cracks forming in some areas. The oblique view in Fig. 5 (b) demonstrates that Fe_3O_4 was deposited on the surface of individual Cu nanorods. Clearly, Fe_3O_4 deposited between the Cu nanorods is well maintained to be nanostructured due to the small inter-rod spaces, which is crucial to gain the advantages of nanomaterials such as shortened Li ion diffusion length. Fig. 5 (c) shows the top view of the same sample after the top thin Fe_3O_4

73

layer was carefully removed by polishing. It confirms that the Fe_3O_4 has been deposited into the Cu nanorod array. The corresponding EDX spectrum (not shown) verifies the presence of the elements of Fe, O, and Cu in the area of Fig. 5 (c).
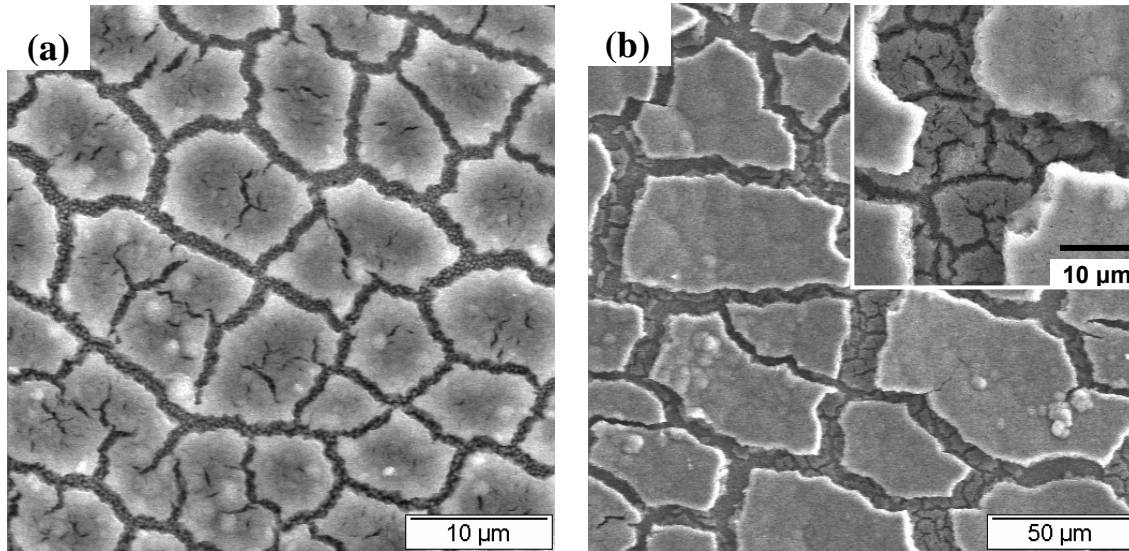

Fig. 6 SEM images of Fe_3O_4 nanoestructured electrode after electrodeposition for (a) 60 s and (b) 300 s, inset: higher magnification image of (b).

When the deposition time was increased to 60 s, the Fe_3O_4 film became thick and bulky islands with average size around 10 μm with large cracks were evident as shown in Fig. 6 (a). One possible reason for the crack generation is the different volume change of Fe_3O_4 deposit and Cu nanorod arrays during sample drying. Fig. 6 (b) indicates that long deposition time of 300 s led to the formation of even thicker and bigger Fe_3O_4 islands with size up to tens of micrometers. The inset shows that the big islands formed right above the small islands in Fig. 6 (a). These micron-sized Fe_3O_4 islands are undesirable for nanostructured electrodes because they may block the passage of electrolyte and Li ion and prevent us from taking the advantages provided by Cu nanorod currently collectors.
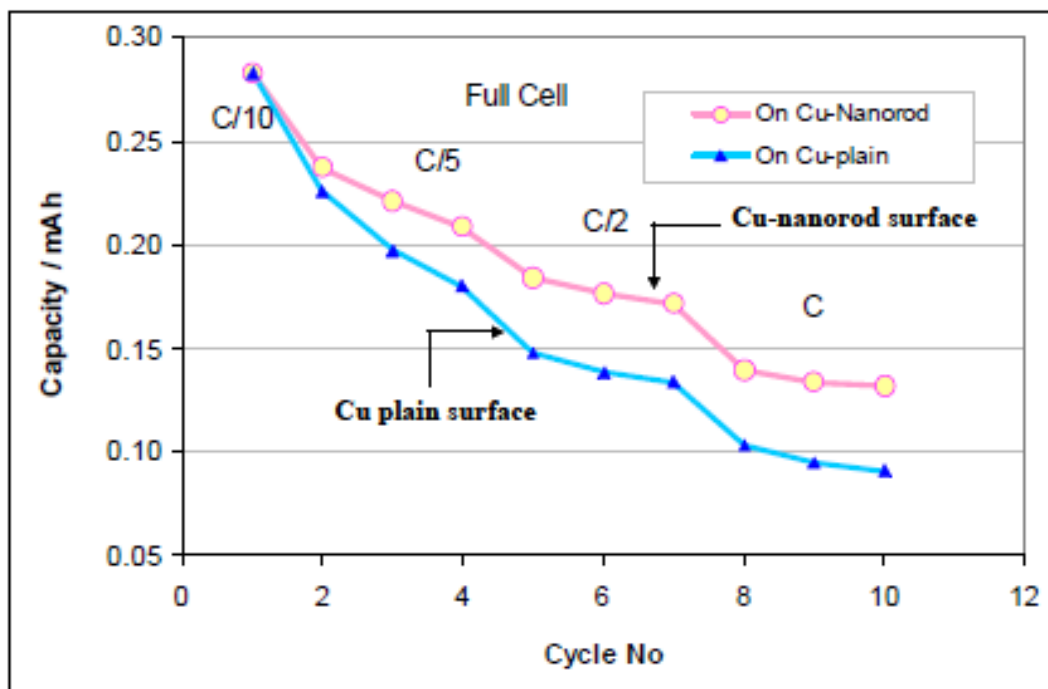
3.3 Pouch/coin cell cycling tests

Fig. 7 Full coin cells charge capacity *vs.* cycle number. The cells cycled at different rates between C/10 and C. For both electrodes, the Fe_3O_4 electrodeposition time was 120 s. Note that the geometrical surface area of the copper disk was 1.26 cm^2.

The full coin cells were cycled at various constant current rates. Fig. 7 compares the charge capacities of the coin cells with the nanostructured and the planar control electrodes at current rates between C/10 and C. For comparison, Fe_3O_4 electrodeposition conditions were kept the same and a 120 s deposition time was used for both samples. The cell with the nanostructured Fe_3O_4 electrodes demonstrated better rate capabilities at high current rates, though they exhibited similar capacities at low current rate of C/10 compared with planar Fe_3O_4. Fig. 7 stresses the benefit of having a nanostructured current collector compared to a planar one in terms of power density.
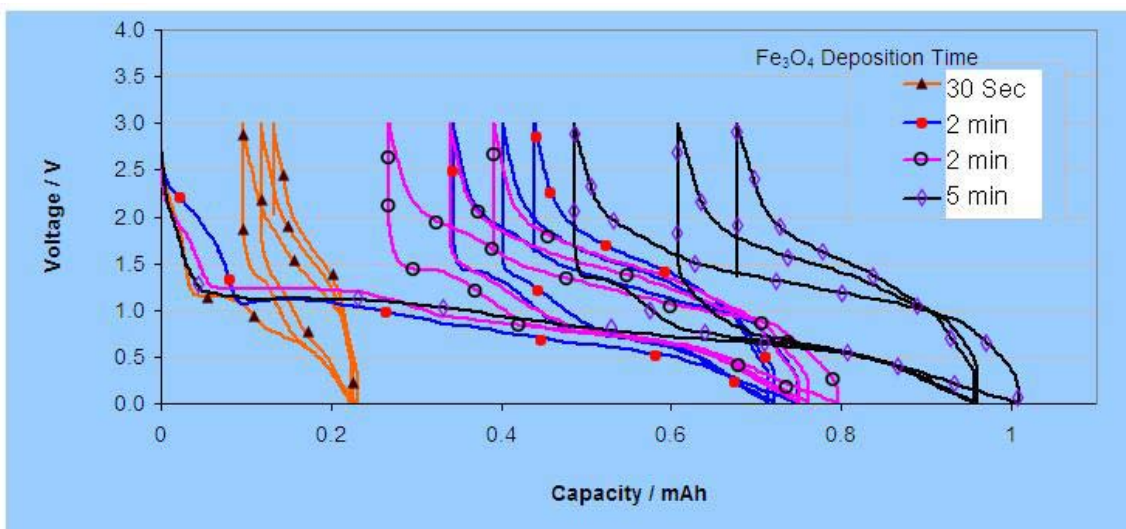
Fig. 8 Potential-capacity profiles of the as-prepared nanostructured electrodes with different Fe_3O_4 deposition time galvanostatically cycled versus Li at a rate of C/20 for the first cycle and C/10 for the second and the third. Note that the geometrical surface area of the copper disk was 1.26 cm^2.

The half-cell test results of the nanostructured electrodes with Fe_3O_4 deposition durations of 30 s, 120 s and 300 s are presented in Fig. 8. It shows that all the nanostructured electrodes behaved alike during the first several cycles, demonstrating the characteristic electrochemical signature of the conversion reactions involved in transition-metal oxide during charging and discharging [1,21]. The potential dropped rapidly to reach a well-defined plateau below 1 V corresponding to the full reduction of Fe_3O_4 into the Fe^0/Li_2O mixture [21]. On cycling, the common charge/discharge hysteretic profiles which are inherent to conversion reactions were maintained. The sample with 300 s Fe_3O_4 deposition time exhibited the largest capacity compared to the other three, which is expected since longer deposition promises more active materials. Fig. 8 also shows that the capacity retention of electrodes with longer deposition durations, i.e. 120 s and 300 s, deteriorated faster than those with shorter deposition time, i.e. 30 s, which is consistent with Tarascon's work [18,21]. The electrode Coulombic efficiency is higher for electrodes with a short Fe_3O_4 deposition time. A value of 88% was obtained after 3 cycles for a deposition time of 30 s, compared to 80% after 300 s of electrodeposition.
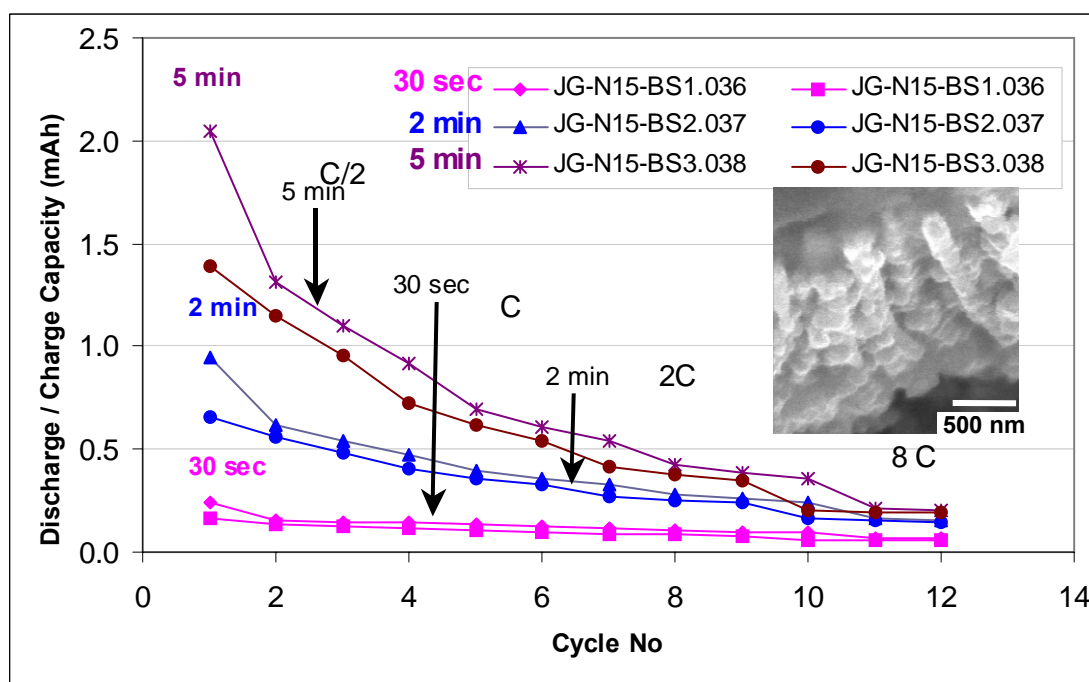
Fig. 9 The capacity retention of a Fe_3O_4 film electrodeposited onto nanostructured copper substrate for different time and cycled at a variety of rates. Inset: SEM image of the electrode with 30 sec Fe_3O_4 deposition after cycling tests.

Fig. 9 shows the charge/discharge capacity profiles of the nanostructured electrodes with different Fe_3O_4 deposition time cycled at various current rates. It is notable that the capacity of the electrode with 30 s Fe_3O_4 deposit demonstrated the best sustained reversible capacity through out the whole cycling process, indicating the electrochemical and mechanical robustness of the electrode. SEM observation after cycling tests revealed no significant morphology change of either the Fe_3O_4 deposits or the Cu nanorods (inset in Fig. 9). In contrast, the capacities of the electrode with 5-min Fe_3O_4 deposition dropped fastest with increasing cycle numbers and those of the electrode with 2-min deposition dropped intermediately.

These half-cell test results, combined with the observation in Fig. 6, strongly suggest that as the time for Fe_3O_4 deposition elapses and the polycrystalline Fe_3O_4 particles aggregate into micron-sized islands above the Cu nanorod arrays, these islands tend to block the access of electrolyte to the inter-nanorod spaces, cause loss of the advantages of nanostructured material, and are undesirable for capacity retention during charge/discharge cycling.

4. Conclusions

The current work develops a nanostructured anode material for Li-ion battery by a two-step fabrication process. This process consists of the AAO template-assisted growth of Cu nanorods onto Cu substrates as nanostructured current collectors followed by the Fe_3O_4 electrodeposition. Uniform and free-standing Cu nanorod arrays were deposited onto mechanically polished Cu disks and the active material of Fe_3O_4 was successfully grown on the surface of individual Cu nanorods. The nanostructured electrode showed superior rate capabilities compared to the planar control samples. It was also observed that the formation of micron-sized Fe_3O_4 islands led to deteriorated reversible capacity retention.

References

[1] P. Poizot, S. Laruelle, S. Grugeon, L. Dupont, J. M. Tarascon, Nature 407 (2000) 496-499.

[2] N. Li, C. R. Martin, B. Scrosati, J. Power Sources 97-98 (2001) 240-243.

[3] X. He, W. Pu, L. Wang, J. Ren, C. Jiang, C. Wan, Electrochimica Acta 11 (2007) 3651-3653.

[4] V. Subramanian, A. Karki, K. I. Gnanasekar, F. Eddy, B. Rambabu, J. Power Sources 159 (2006) 186-192.

[5] H. Wang, T. Abe, S. Maruyama, Y. Iriyama, Z. Ogumi, K. Yoshikawa, Adv. Mater. 17 (2005) 2857-2860.

[6] M. Park, Y. Kang, G. Wang, S. Dou, H. Liu, Adv. Func. Mater. 18 (2008) 455-461.

[7] J. Li, Z. Tang, Z. Zhang, Electrochem. Commun. 7 (2005) 62-67.

[8] P. G. Bruce, Chem. Commun. 19 (1997) 1817-1824.

[9] E. Hosono, S. Fujihara, I. Honma, M. Ichihara, H. Zhou, J. Electrochem. Soc. 153 (2006) A 1273-A1278.

[10] A. S. Arico, P. Bruce, B. Scrosati, J. M. Tarascon, W.V. Schalkwijk, Nature Mater. 4 (2005) 366-377.

[11] C. R. Sides, N. Li, C. J. Patrissi, B. Scrosati, C. R. Martin, MRS Bull. 26 (2002) 604-608.

[12] S. Ito, K. Nakaoka, M. Kawamura, K. Ui, K. Fujimoto, N. Koura, J. Power Sources 146 (2005) 319-322.

[13] A. R. Armstrong, G. Armstrong, J. Canales, R. Garacia, P. G. Bruce, Adv. Mater. 17 (2005) 862-865.

[14] J. M. D. Coey, A. E. Berkowitz, Li. Balcells, F. F. Putris, F. T. Parker, Appl. Phys. Lett. 72 (1998) 734-736.

[15] M. M. Thackeray, W. I. F. David, J. B. Goodenough, Mater, Res. Bull. 17 (1982) 785-793.

[16] M. M. Thackeray, J. Coetzer, Mater, Res. Bull. 16 (1981) 591-597.

[17] D. Larcher, C. Masquelier, D. Bonnin, Y. Chabre, V. Masson, J. B. Leriche, J. M. Tarascon, J. Electrochem. Soc. 150 (2003) A133-A139.

[18] S. Mitra, P. Poizot, A. Finke, J. M. Tarascon, Adv. Funt. Mater. 16 (2006) 2281-2287.

[19] J. S. Gnanaraj, J. F. DiCarlo, H. Duan, J. Liang, R. W. Thompson, 10th Power Source R&D Symposium, Williamsburg, VA, August 20-23, 2007.

[20] http://www.whatman.com

[21] P. L. Taberna, S. Mitra, P. Poizot, J. M. Tarascon, Nature Mater. 5 (2006) 567-573.

[22] H. M. Kothari, E. A. Kulp, S. J. Limmer, P. Poizot, E. W. Bohannan, J. A. Switzer, J. Mater. Res. 21 (2006) 293-301.

[23] H. Chik, J. Liang, S. G. Cloutier, N. Koukli, J. M. Xu, Appl. Phys. Lett. 84 (2004) 3376-3378.

[24] J. Liang, H. Chik, J. Xu, IEEE J. Selected Topics in Quantum Electronics 8 (2002) 998-1008.

CHAPTER IV: RESEARCH CONCLUSIONS AND FUTURE WORK

This thesis presents a series of experimental investigations covering the synthesis, integration, and characterization of functional nanomaterials. Corresponding to the research objectives in Chapter I, the following conclusions are drawn. Future work is also included at the end of each conclusion.

1. AAO template assisted nanofabrication [Paper # 1 and Appendix A]: based on a two-step anodization process to prepare AAO templates, we fabricated a variety of ordered 1-D nanostructures including metal NWs, metal NRs and CNTs of different sizes, aspect ratio, and shapes. The metal NWs and NRs are synthesized using both DC and AC electrodeposition, and the CNTs are obtained by CVD with and without metallic catalysts. Morphology study shows that the dimension of the as-prepared 1-D nanostructures is well defined by nanochannel of the template which can be further controlled by adjusting the anodization conditions such as voltage, time, and electrolyte bath. Among them, the Y-junction Co NWs and Y-junction Cu NWs synthesized by AC electrodeposition are the first example of using AC electrodeposition to fabricate Y-junction metal NWs. By structural analysis, it's interesting to find that Co NWs is a mixture of FCC and HCP structures, whereas FCC microstructure is retained for Cu NWs.

Further work includes (1) using HRTEM to study in more details the microstructure near the junction; (2) identifying the factors affecting the Co NWs by varying synthesis conditions such as pH value of electrolyte bath, voltage, frequency; (3) studying the effect of introduction of Y-junction on the mechanical property and thermal property of the metal NWs.

2. Synthesis and study of the hierarchical structures of CNFs and CMFs or GMFs [Paper # 2]: employing the CCVD technique, the possibility of growing CNFs on individual CFs and GFs to form a three-dimensional hierarchical structure is explored. CNFs grown on both CFs and GFs demonstrated coexistence of two types of morphology. One is winded fibers implying frequent orientation change. The other one is relatively straight and long fiber with graphene sheets parallel to each other. Possible reasons causing varying deposition and

precipitation rates for different catalyst surfaces include: (1) different catalytic ability for different crystal planes, (2) asymmetrical shaped catalyst particles which lead to different diffusion path lengths for the carbon atoms to traverse; (3) nonuniform carbon supply. CNFs grown on CMF substrate are thicker and more uniform than those on GMF substrates probably due to different catalyst-substrate interaction and different growth temperature. The as-grown three-dimensional carbon-carbon and carbon-glass hierarchical structures provide an effective means to connect nanoscale entities to the higher hierarchy.

Further work includes: (1) optimizing the synthesis conditions to produce the CNF and CMF or GMF hierarchical structures; (2) controlling the growth direction of the CNFs on MFs by external forces such as electric field and magnetic field; and (3) synthesis hierarchical structures of other materials such as ZnO.

3. Design and study of the electrochemical property of nanostructured electrodes [Paper # 3, # 4, and Appendix B]: both Fe_3O_4-based and TiO_2-based nanostructured electrodes are developed by a two-step fabrication process. This process consists of the AAO template-assisted growth of Cu nanorods onto Cu substrates as nanostructured current collectors followed by the loading of Fe_3O_4 or TiO_2. Uniform and free-standing Cu nanorod arrays are deposited onto mechanically polished Cu disks and the active material of Fe_3O_4 or TiO_2 is successfully grown on the surface of individual Cu nanorods. The active materials are also deposited on planar Cu substrate for comparison. The Fe_3O_4-based nanostructured electrode shows superior rate capabilities compared to the planar control samples. It is also observed that the formation of micron-sized Fe_3O_4 islands led to deteriorated reversible capacity retention. While for TiO_2-based nanostructured electrode, though large amount of TiO_2 is deposited and high specific capacity is gained with the introduction of Cu nanorods, higher degree of oxidation also occurs for the nanostructured electrodes in comparison of the planar electrodes, which affects Li ion insertion mechanism and the rate capability.

Further work includes: for Fe_3O_4-based electrode, (1) scaling up the fabrication process to make large rectangular electrodes ($4^{"} \times 6^{"}$) instead of small circle ones (Φ 13 mm) to move toward pilot testing; (2) More detailed microstructure study by SAD or XRD to clarify the Li ion insertion/deinsertion process; (3) for TiO_2-based electrode, stabilizing the

fabrication process and reducing the oxidation of Cu NR during fabrication.

APPENDIX A: AAO-ASSISTED FABRICATION OF 1 D NANOMATERIALS

1. AAO template synthesis

Based upon the information presented in Chapter II, anodized aluminum oxide (AAO) template-assisted fabrication provides an important strategy to synthesize nanomaterials. The synthesis of AAO templates with densely hexagonally packed straight nanochannels is a good starting point for this method. The nanopores self-organize into a highly ordered array of uniform pores with the pore diameter, the period, and the array size being variable over ranges that are beyond the reach of standard e-beam lithography [1-4]. The alumina nanopore array is formed by anodization of high-purity aluminum under certain carefully controlled anodization conditions. The optimized anodization parameters in different electrolytes are shown in Table A.1. Periodical porous oxide with remarkably ordered arrangements of cylindrical pores, whose diameter varies in the range of 35 nm to 300 nm, can now be realized routinely in our lab using a two-step process published previously [5-7].

Table A.1 Optimized parameters for AAO template anodization [8]

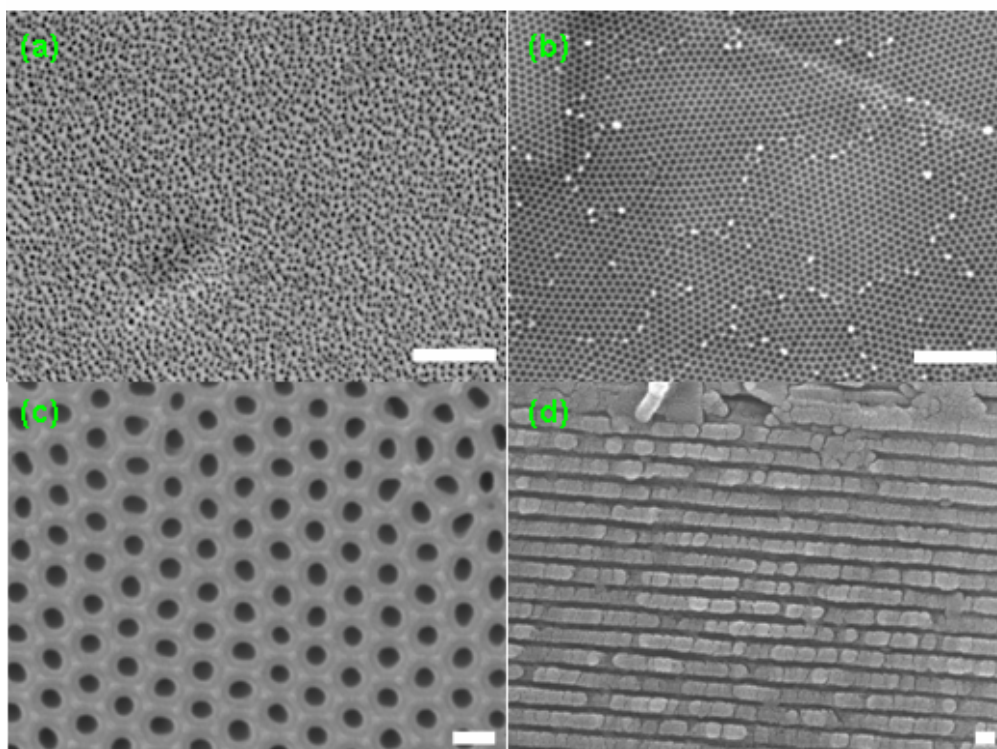| Electrolyte (acid)	Concentration	Temperature (^{o}C)	Voltage (V)	Typical resulting mean diameter (nm)
Oxalic	0.3 M	10	40	45
Phosphoric	1 M	0	160	400
Sulfuric	0.5 M	0	25	30

Fig. A.1 SEM images of AAO template during a two-step process in oxalic acid system: (a) after 1st anodization; (b) after dissolving the membrane formed in the 1st anodization; (c) top view and (d) cross-section view of the membrane after 2nd anodization. Scale bars: (a) and (b) 1 μm, (c) and (d) 100 nm.

Fig. A.1 shows SEM images of the AAO template in each step of the two-step fabrication process in an oxalic acid system. From Fig. A.1a, we can see that during the 1st anodization, porous anodic alumina forms at the aluminum surface. A hexagonal topographic structure is exposed on the Al substrate after dissolving the alumina film formed in the 1st anodization (Fig. A.1b). The nanochannels grow from the structure during the 2nd anodization and as a result the arrangement of the nanopore array mimics the hexagonal topographic structure (Fig. A .1c and d). The resultant nanoscale pores are parallel, straight, and oriented vertical to the surface (Fig. A.1e) and they are uniform in diameter (approximately 45 nm) and in spacing.

2. AAO-template assisted nanofabrication

As shown in Fig. A.2, by using the AAO membrane as a template, a number of different nanostructures including metal nanowire (NW) arrays, metal nanorod (NR) arrays and carbon nanotube (CNT) arrays have been synthesized.
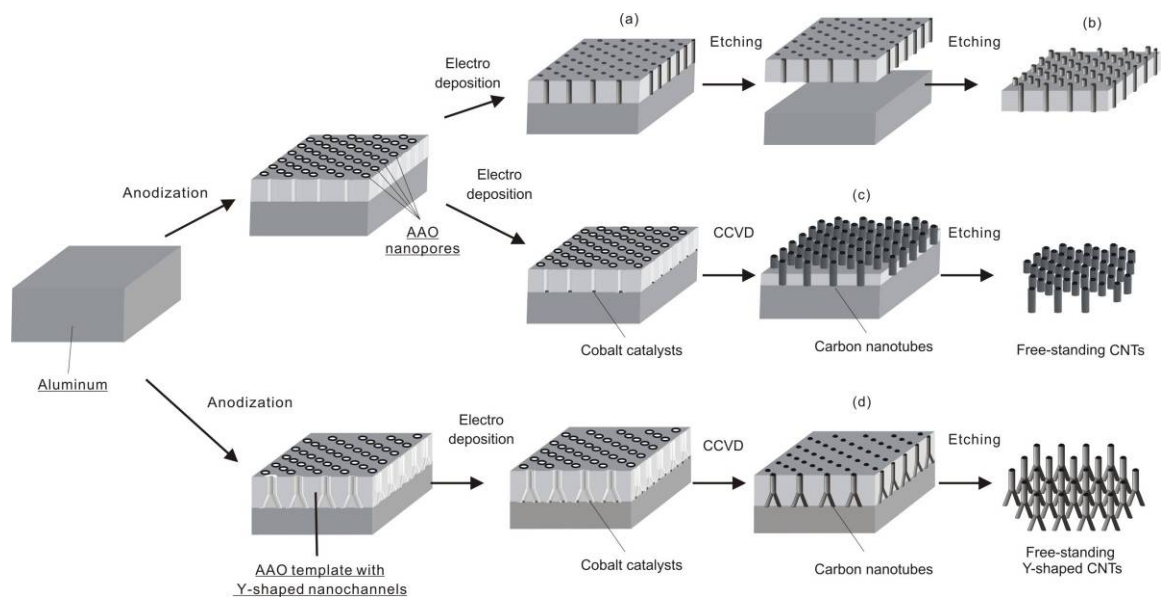

Fig. A.2 Schematic of the fabrication of ordered inorganic nanomaterial arrays: (a) metal NW arrays electrodeposited in AAO template; (b) metal NW array embedded in AAO template with tips exposed by etching; (c) CNT array grown by CCVD; (d) Y-shaped CNT array grown by CCVD.

2.1 Carbon nanotubes fabricated by AAO-assisted CVD method

2.1.1 CNTs synthesized by catalytically CVD

Fig. A.3 shows SEM images of CNTs synthesized using the fabrication process described in one of the published paper [9]. As shown in Fig. A.3a, the template is covered by a layer of junk carbon which is a by-product of CNT growth. After thermal cleaning in air at 600 $^{\circ}$C for 30 min, this layer of junk carbon can be removed and the hexagonal pattern of nanochannels underneath is shown in Fig. A.3b. The CNTs can be exposed by dry etching the AAO template (Fig. A.3c). It was found that a high filling rate is obtained under current conditions. Fig. A.3d shows that the CNTs are well embedded in the nanochannels. Fig. A.3e

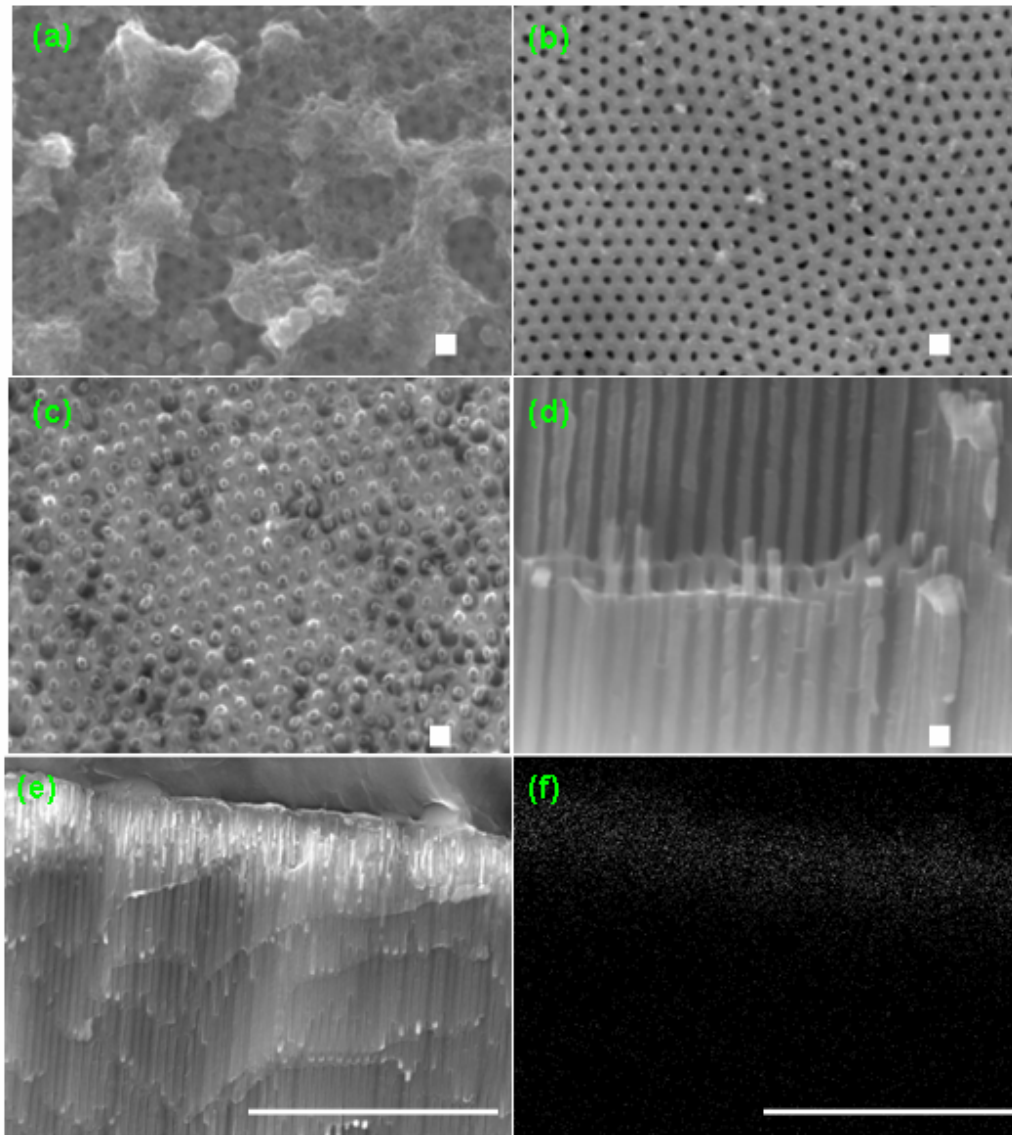and 3f indicate that the Co catalysts stay at the bottom part of the AAO template during CNT growth.

Fig. A.3 CNTs fabricated by AAO-assisted CCVD method: (a) as-prepared samples; (b) samples after thermal cleaning at 600 ^{o}C for 30 min; (c) CNTs with tips exposed by reactive ion etching (TIE); (d) cross-section view of CNTs embedded in the AAO nanochannels; (e) and (f) cross-section view and the corresponding element mapping (Co) of the bottom part of the sample. Scale bars: (a), (b), (c), and (d) 100 nm, (e) and (f) 3 μm.

As shown in Fig. A.4, the outer diameter is 44.96 $\pm$ 3.79 nm and the inner diameter is 11.80 $\pm$ 2.24 nm. Clearly, the outer diameter is close to the pore size of the AAO template. Higher magnification TEM images show that both hollow (Fig. A.4b) and bamboo-like CNTs (Fig. A.4c) can be observed in a single nanotube.
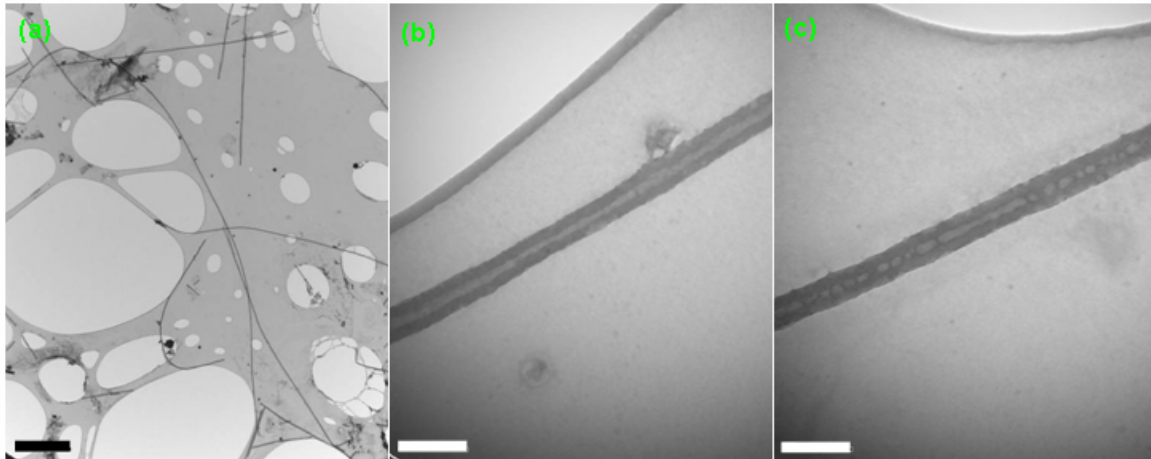
Fig. A.4 TEM images of Straight MWCNTs by AAO-assisted CCVD method. Scale bars: (a) 2 μm, (b) and (c) 100 nm.

By using the AAO template with Y-junction channels fabricated according to the process described in Chapter III Paper # 1, Y-junction CNTs are synthesized by CVD. The growth conditions are similar to those used for straight CNT growth with a few minor adjustments. The growth time is reduced to 15 min because the thickness of the template is about 5 μm. Fig. A.5 depicts TEM images of the Y-junction CNTs. The outer diameters of the stem and the branch are measured by Image J to be 49.64 ± 3.62 nm and 24.62 ± 3.94 nm, respectively, which agree well with the pore size of the nanochannels.
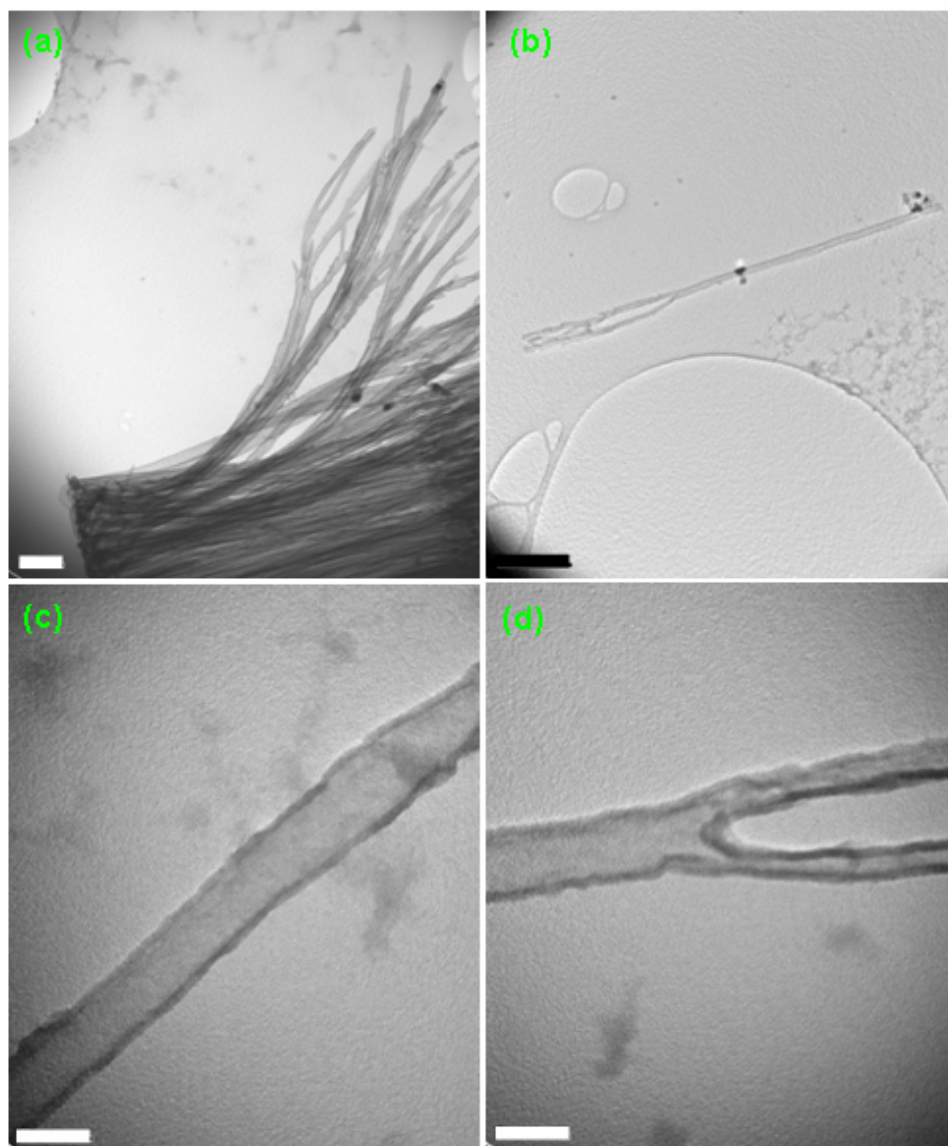
Fig. A.5 TEM images of Y-shaped MWCNTs by AAO-assisted CCVD method: (a) bundled Y-shaped MWCNTs; (b) a single Y-shaped MWCNT, (c) the stem and (d) the branching of the CNTs. Scale bars: (a) 200 nm, (b) 500 nm, (c) and (d) 50 nm.

2.1.1 CNTs synthesized by catalyst-free CVD

Fig. A.6 shows SEM images of CNTs synthesized using commercial AAO templates with a pore size of 20 nm and 200 nm. The fabrication process is similar to that described in in one of the published papers [9] except that here a commercial catalyst-free template is used. Clearly, CNTs can be grown inside both types of templates with a high filling rate, and the CNTs have open ends. Fig. A.7 exhibits SEM images of the CNTs which are synthesized using a 200 nm commercial AAO template and are partially filled with Cu by

electrodeposition. Cu rods with length about 1 um are deposited inside the CNTs, which is confirmed by the EDS.
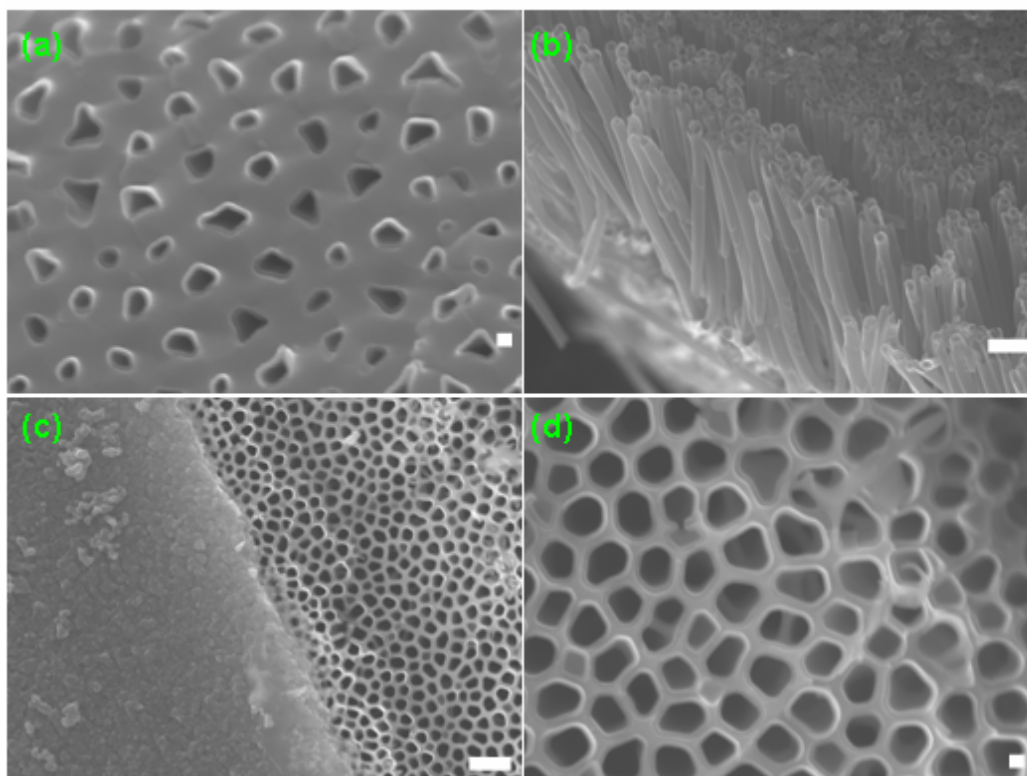

Fig. A.6 CNT fabricated by CVD using commercial AAO templates with pore size of (a), (b) 20nm and (c), (d) 200nm. Scale bars: (a) and (d) 100 nm, (b) and (c) 1 μm.
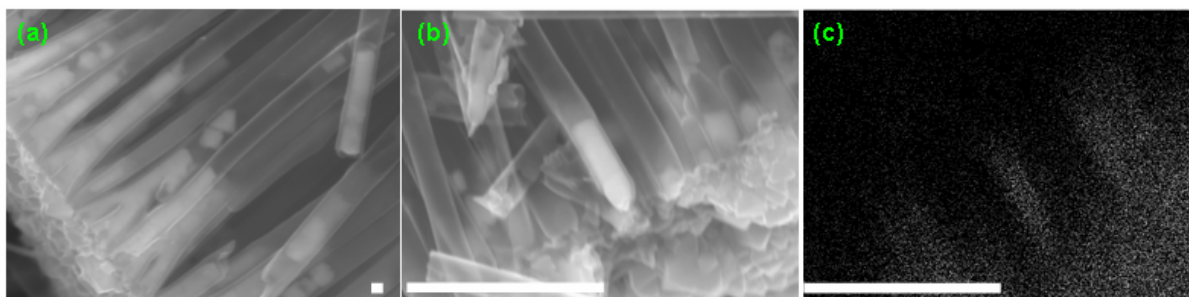

Fig. A.7 (a), (b) SEM images of CNTs partially filled with Cu and (c) Cu element mapping of area (b). Scale bars: (a) 100 nm, (b) and (c) 2 μm.

Fig. A.8 shows CNTs synthesized using homemade AAO templates. The template is separated from an Al substrate by 1 wt.% $HgCl_2$ solution, and then is subject to CNT growth at 600 ^{o}C without using any catalyst. The CNTs can easily be grown inside the template with dimension well confined by the nanochannels. The TEM image (Fig. A.8d) has less contrast compared to that of CNTs grown with Co catalysts (Fig. A.4b), which suggests poorer crystallinity of CNTs when a catalyst is not used.
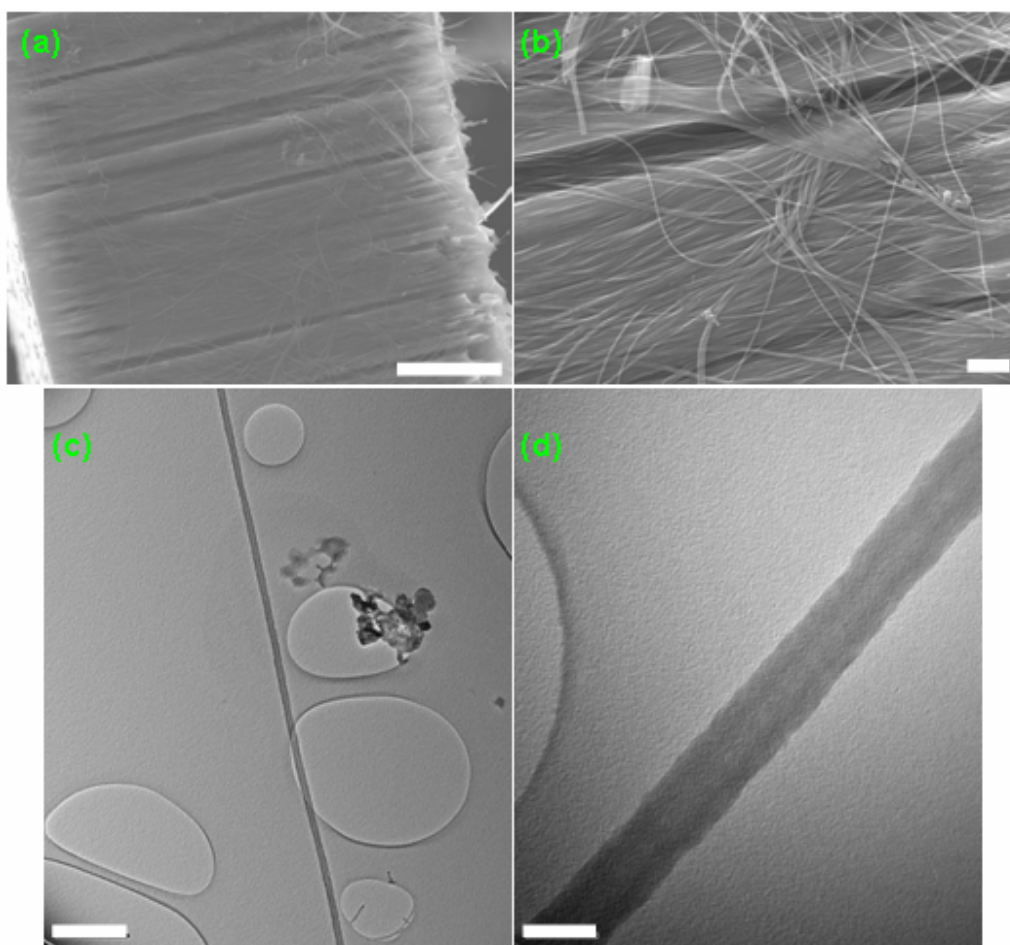
Fig. A.8 Homemade 60nm AAO template: (a), (b) cross-section view of CNTs in the AAO template; (c), (d) TEM images of the CNTs. Scale bars: (a) 10 μm, (b) 1μm, (c) 500 nm, and (d) 50 nm.

2.2 Co nanowires fabricated by AAO-assisted method

Fig. A.9 shows SEM images of Co NWs synthesized by the AC electrodeposition process described in Chapter III Paper # 1. As we can see from Fig. A.9a and b, Co NWs with diameter of 45.64 ± 9.12 nm are obtained, and the dimensions of the Co NW is defined by the nanochannels in the AAO template. TEM images shown in Fig. A.9c and d illustrate that a thin layer of oxide is formed on the surface of a single NW.
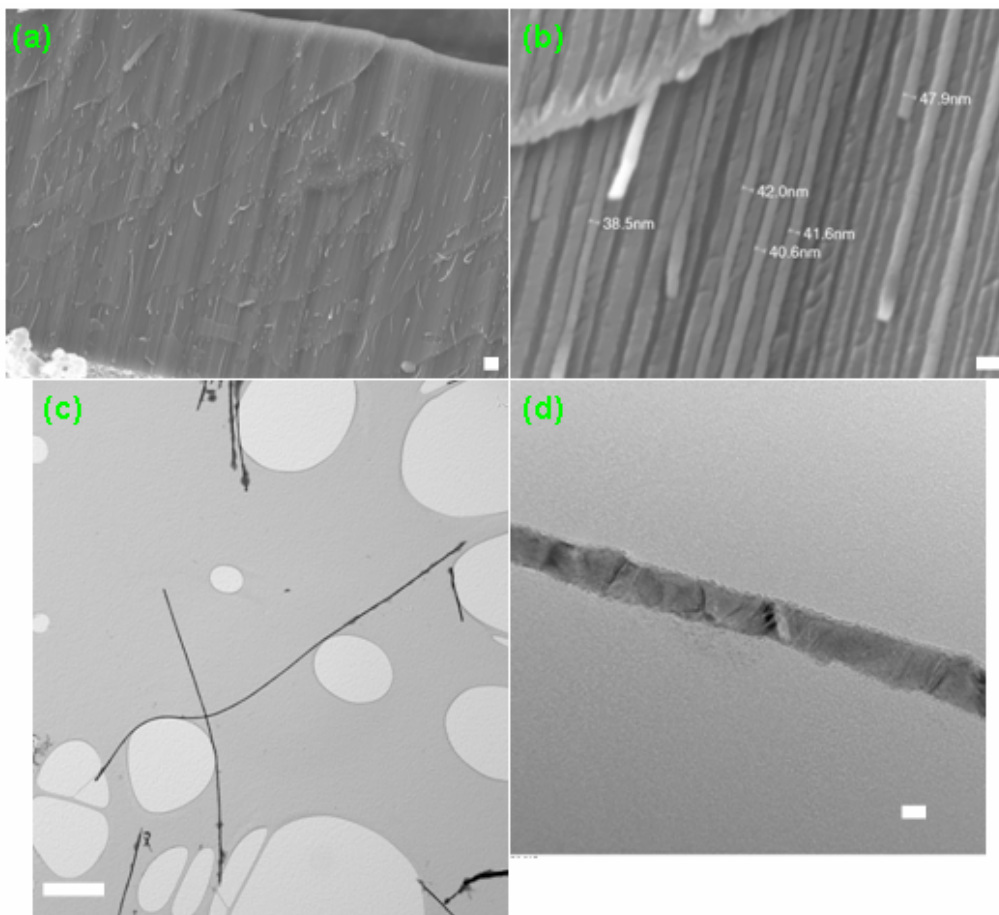
Fig. A.9 Straight Co NWs synthesized by AC electrodeposition using AAO templates: (a), (b) cross-section view of the Co NWs embedded in the AAO template; (c), (d) TEM images of Co NW after dissolving the template. Scale bars: (a) 1 μm, (b) 100 nm, (c) 2 μm, and (d) 20 nm.

2.3 Cu nanorods fabricated by AAO-assisted method

SEM images of Cu NRs fabricated by DC electrodeposition using AAO templates are shown in Fig. A.10. Details of the fabrication are presented in Chapter III Paper # 4. As shown in Fig. A.10a and b, Cu NRs can be deposited uniformly on the mechanically polished Cu substrate, and each Cu NR is dimensionally defined by the AAO template. As the template is changed from a 200 nm commercial template to a 100 nm homemade template, the Cu NRs form a hexagonal pattern and their diameters decrease accordingly.
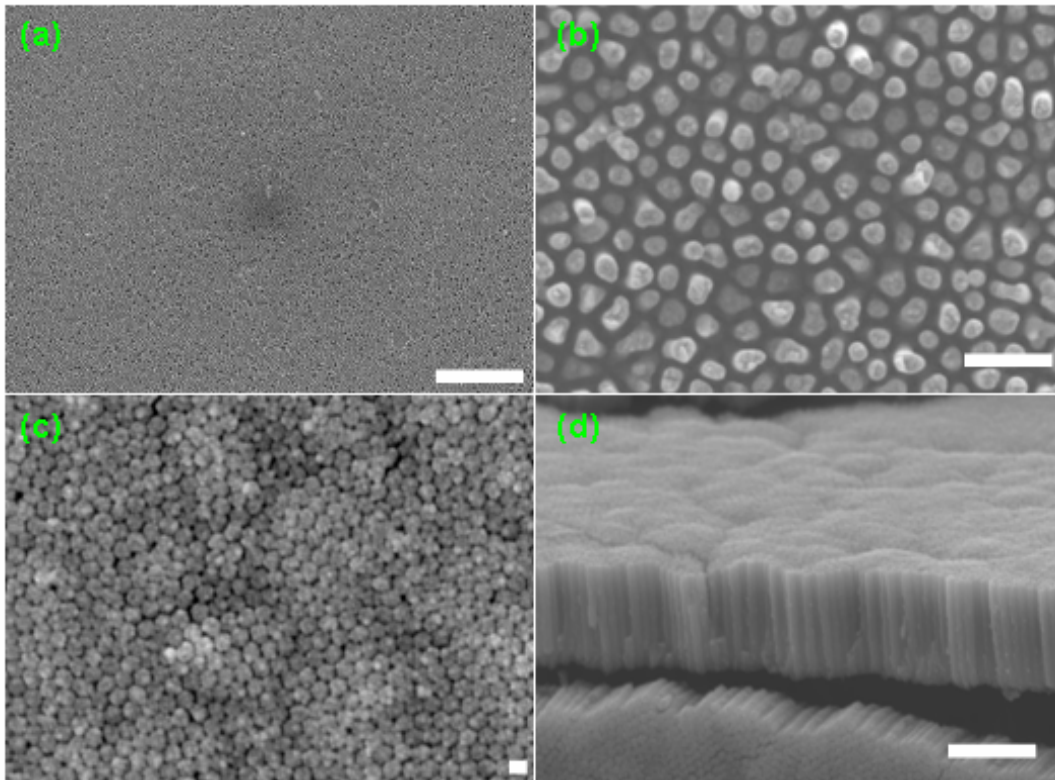
Fig. A.10 Cu NRs synthesized by electrodeposition using (a), (b) commercial AAO template and (c), (d) homemade AAO template. Scale bars: (a) 10 μm, (b) 1 μm, (c) 100 nm, and (d) 1 μm.

Reference

[1] Li, J.; Papadopoulos, C.; Xu, J. M. *Appl. Phys. Lett*. **1999**, *75*, 367.

[2] Parthasarathy, R. V.; Phani, K. L. N.; Martin, C. R. *Adv. Mater*. **1995**, *7*, 896.

[3] Kyotani, T.; Tsai, L.; Tomita, A. *Chem. Mater.* **1996**, *8*, 2109.

[4] Li, J.; Moskovits, M.; Haslett, T. L. *Chem. Mater*. **1998**, 10, 1963.

[5] Liang, J.; Chik, H.; Yin, A.; Xu, J. M. *J. Appl. Phys.* **2002**, *91*, 2544.

[6] Liang, J.; Chik, H.; Xu, J. M. *IEEE J. Sel. Top. Quantum Electron* **2002**, *8*, 998.

[7] Li, J.; Papadopoulos, C.; Xu, J. M.; Moskovits, M. *Appl. Phys. Lett*. **1999**, *75*, 367.

[8] Liang, J. *Non-lithographic fabrication of Superlattices for Nanometric electro-magnetic-optic applications*. Ph. D. dissertation. 2005.

[9] Pradhan, N. R.; Duan, H.; Liang, J.; Iannacchione, G. S. In press by Nanotechnology.

APPENDIX B: ELECTROCHEMICAL PREPARATION OF NANOSTRUCTURED TiO$_2$ AS ANODE MATERIAL FOR Li ION BATTERIES

(published in *Proc*. MRS **2008**, Boston, MA,)

ABSTRACT

TiO$_2$ is an attractive anode material for Li-ion batteries due to its high capacity, high mechanical stability during Li intercalation/deintercalation process, limited side reactions with the electrolyte, low cost, and environmental friendliness. In this study, titanium hydroxide gel films were prepared in acidic aqueous solutions of TiOSO$_4$, H$_2$O$_2$ and KNO$_3$ by potentiostatic cathodic electrosynthesis on various copper substrates, including planar Cu foil, mechanically polished planar Cu foil, and Cu nanorod arrays grown on Cu foil. Crystalline TiO$_2$ films were obtained by heat treating the electrodeposited titanium hydroxide gel films at 500 ^{o}C in argon atmosphere. The morphology and microstructure of the TiO$_2$ films were characterized by scanning electron microscope (SEM) and X-ray diffraction (XRD). SEM results showed that after deposition, each Cu nanorod has been covered by a layer of TiO$_2$ gel, forming a core-shell structure. The effects of Cu nanorod arrays on the morphology and the electrochemical property of the TiO$_2$ deposits were discussed.

INTRODUCTION

Lithium-ion (Li-ion) batteries are attractive candidates for use as power storage in many applications because of their high specific energy, energy density and cycle life. The conventional Li-ion batteries have achieved great commercial success since their invention in 1980's. However, they have been suffering from two major problems. Firstly, when the charge/discharge rate is higher than 1 C (C defined as the full use of the capacity in 1 h) or Li ions are inserted into graphite at a potential of less than 1 V versus Li$^+$/Li, lithium may be plated on the carbon electrode surface causing safety hazard [1]. Secondly, slow solid-state diffusion of Li$^+$ within the electrode materials limits the rate capability of Li-ion batteries

[2,3]. Therefore there is a vigorous research effort on using nanomaterials to improve the safety and the rate capabilities of electrodes.

TiO$_2$ is a promising anode material for next-generation Li ion batteries. Various nanoforms of TiO$_2$, including nanocrystalline anatase, amorphous TiO$_2$ and TiO$_2$ nanotubes, have been studied as high-rate Li-ion anode materials and indeed demonstrated improved property at high current densities [4-9]. Of the various polymorphs of TiO$_2$, anatase, amorphous or unique nanostructured TiO$_2$ is desirable for fast and high volume lithium insertion/desertion. It has also been shown that not only the particle size of the active materials making up the electrode but also the size of grains within these particles plays critical roles in the Li$^+$ insertion/deinsertion process [10]. However, it is not easy to control the size and size distribution of the nanoparticles or clusters. In addition, packing the nanomaterials into an electrode film with good electrical contact and sufficient mechanical support while retain the large accessible surface area to electrolyte and small diffusion length of Li$^+$ is critical to the electrochemical properties of the electrode. Therefore, not only low cost and highly controllable synthesis of nanomaterials, but also a smart design of nanostructured electrode exploring the full gain offered by using nanomaterials is demanded.

In this work, based on the same philosophy that we used to fabricate Fe$_3$O$_4$-based Cu nanostructured electrode [11], we propose to develop a novel nanoengineered TiO$_2$ anode with rapid Li$^+$ recharge characteristics. The morphology and electrochemical properties of the nanoengineered electrode will be compared to its planar counterparts.

EXPERIMENT

Electrode fabrication

The fabrication process of TiO$_2$ based Cu-nanostructured electrodes, as shown in Fig. 1, is similar to the process described in one of our previous publications [11,12]. Briefly, key steps include (i) mechanical polishing of Cu substrates, (ii) fabrication of Cu nanorod (NR) arrays as current collectors by anodized aluminum oxide (AAO) templates assisted electrodeposition, and (iii) electrochemical deposition of TiO$_2$ onto the nanostructured current collectors. Before electrodeposition, the cathode Cu disk was mechanically polished, followed by rinsing with deionized (DI) water and ultrasonically cleaning in ethanol.

Arrays of perpendicular Cu NRs were fabricated by cathodic electrodeposition in $CuSO_4 \cdot 5H_2O$, $(NH_4)_2SO_4$, and Diethylenetriamine (DETA) solution using the polished Cu foil as the cathode through template-assisted electrodeposition [12,13]. After the electrodeposition, the AAO template was removed by dipping the sample into NaOH solution. The fabricated free-standing Cu NR forest was employed as the substrate for TiO_2 electrodeposition. For comparison, in addition to Cu NR arrays, the unpolished and polished planar Cu foils were also used as substrates for TiO_2 electrodeposition in this work.

TiO_2 electrodeposition was adapted from a two-step process [14]. The first step is the formation of amorphous $TiO(OH)_2 \cdot xH_2O$ gel film by electrodeposition in $TiOSO_4$, H_2O_2 and KNO_3 solution and the second step is heat treatment of the titanium hydroxide gel films to obtain crystalline TiO_2 deposits. A conventional three-electrode system was used to deposit TiO_2 with the Cu substrates as the working electrode, Pt as the counter electrode and Ag/AgCl as the reference electrode. All potentials in this work were referred to the Ag/AgCl electrode. The deposition voltages were determined by cyclic voltammetric (CV) studies. -700 mV was chosen for deposition on planar Cu substrates and -800 mV on the Cu NR arrays. The electrodeposition time was 30 min for the planar substrates and 20 min for the nanostructured Cu substrates. After electrodeposition, the samples were heated to 500 $^{\circ}$C for 3 hours in Ar atmosphere to obtain crystalline TiO_2.
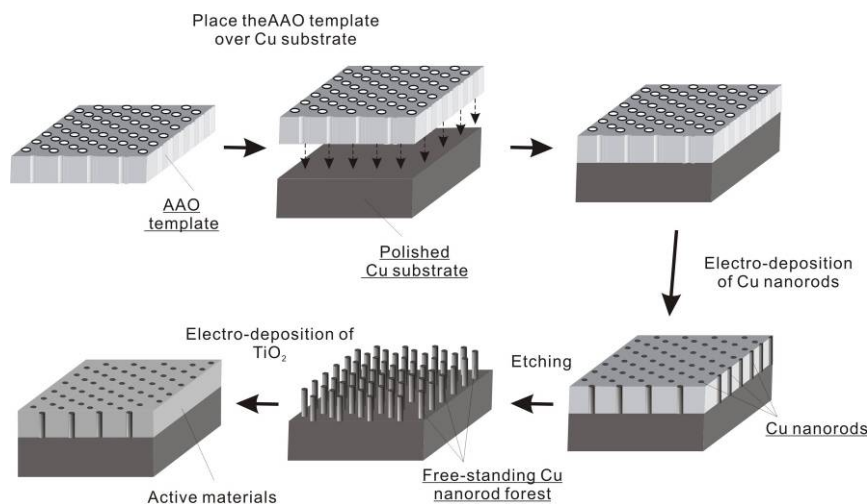

Fig. 1 Schematic of the fabrication of nanostructured electrode.

Structure analysis and morphology characterization

The as-prepared electrodes were examined by X-ray diffraction (XRD) using a REGAKU CN2182D5 diffractometer and scanning electron microscopy (SEM) using JEOL JSM-7000F microscope.

Electrochemical tests

The electrochemical performance of the electrodes was evaluated in conventional coin and pouch cells. Briefly, coin/pouch half cells were constructed using metallic lithium as the counter electrodes and the TiO_2 electrodes as the anodes under argon atmosphere inside a glove box. The half cells were cycled galvanostatically at current rates of 25 mA g^{-1} and 50 mA g^{-1}. The current rates were determined by the amount of the deposited TiO_2 and assuming its theoretical specific capacity to be 162 mAh g^{-1}. Setela of 20 μm in thickness was used as the separators. The standard electrolyte of 1M $LiPF_6$ (in ethylene carbonate (EC): dimethyl carbonate (DMC): diethyl carbonate (DEC)/1:1:1 in volume ratio) was used for the half-cell tests.

RESULTS AND DISCUSSION

Atomic force microscope (AFM) images in Fig. 2 show that the mechanical polishing effectively reduced the surface roughness, Ra from 62.8 nm down to 12.5 nm. It's obvious that the polished foil has a smoother surface with fewer valleys.

Fig. 3 shows the SEM images of the unpolished and polished Cu foils after titanium hydroxide gel deposition and after heat treatment. After the titanium hydroxide gel deposition, the Cu surface was covered with a thin layer of gel. Though the morphologies of the gel looked different for the unpolished (Fig. 3a) and polished (Fig. 3b) Cu foils, the resultant crystalline TiO_2 deposits exhibited similar morphology after heat treatment (Fig 3c and d). After heat treatment, dense TiO_2 deposits with small grains were observed for both samples. The morphology looks different from those in previous works, where conductive glasses were used as the deposition substrates [14,15]. The small cracks or holes in Fig 3a and Fig 3b may be resulted from the volume shrinkage due to the dehydration of titanium hydroxide gel and the different thermal expansion coefficients of the gel films and the Cu substrates during

96

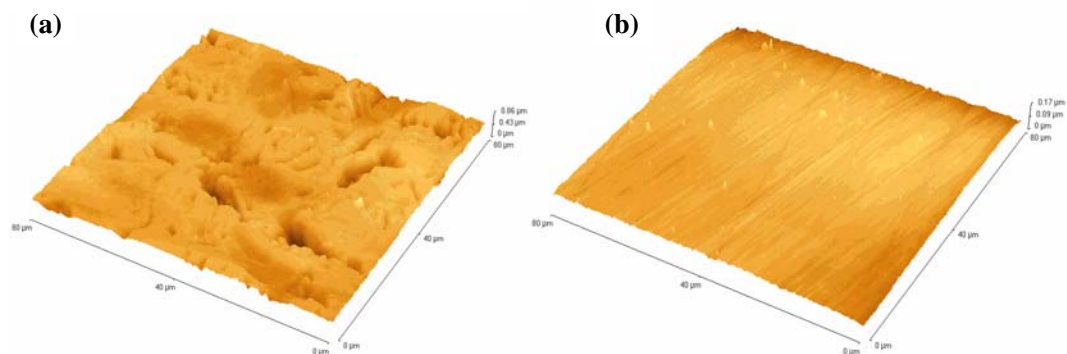drying the sample, which is common for oxide deposited on metal substrates [16-18].

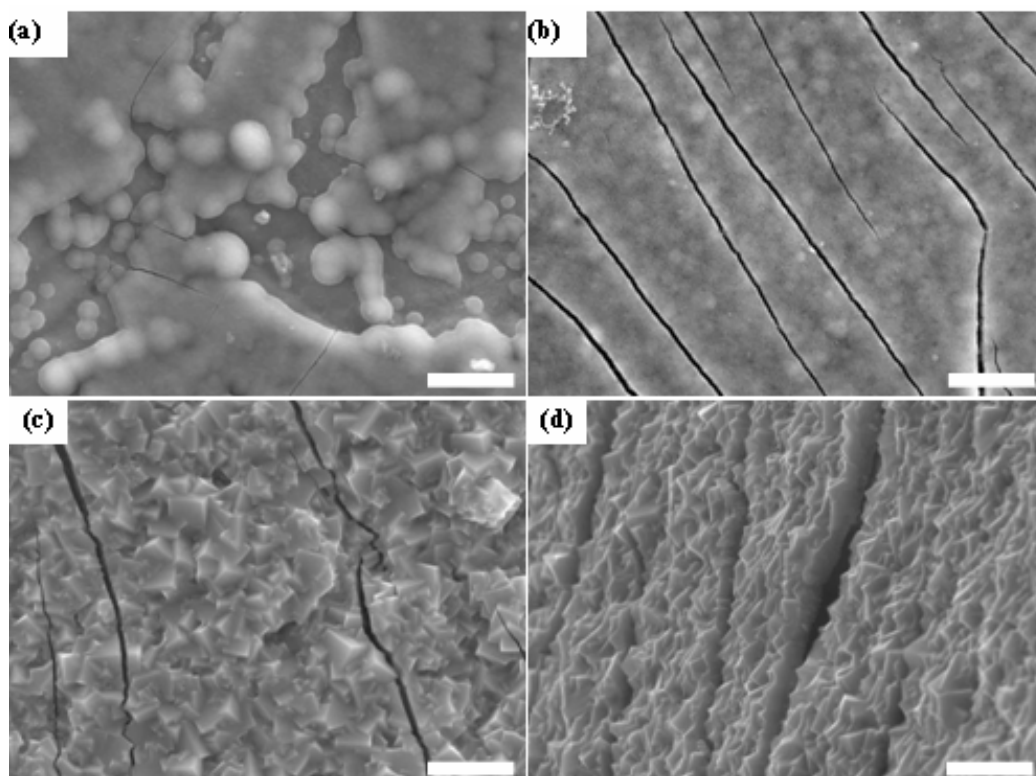**Fig. 2** AFM images of unpolished (a) and polished Cu foils (b).

Fig. 3 SEM images of unpolished and polished Cu foil after (a) (b) titanium hydroxide gel deposition, and after heat treatment (c) (d). Scale bars: (a) - (d) 1 μm.

Typical SEM images of the electrode using Cu NR arrays as the current collector are shown in Fig. 4. Fig. 4a and b are the top-view and oblique-view SEM images of free-standing Cu NR arrays obtained by the template assisted electrodeposition. The top-view image (Fig.4a) shows that the polished Cu substrate surface has been covered by uniform and free-standing copper nanorods. As confirmed by our previous studies [19,20], the size of Cu

NRs was defined by the nanopore size of the AAO template.   The oblique-view SEM image suggests that the average diameter is 200 nm, the length of the Cu NRs is around 2 μm and the inter-rod distance is less than 100 nm.

After 20-min electrodeposition, the Cu NRs were covered with $TiO(OH)_2 \cdot xH_2O$ gel film and bundled together to form islands as shown in Fig. 4c. The cross-sectional view (Fig. 4d) indicates that each Cu NR has been covered by a layer of TiO_2 gel, forming a core-shell structure. This morphology looks very different from that in Fig. 3. After heat treatment at 500 ^{o}C, the island morphology was retained (Fig. 4e), and the gel was turned into a dense layer of TiO_2 crystallites. So a greater amount of TiO_2 deposits is expected because of the large surface area introduced by the Cu NRs.
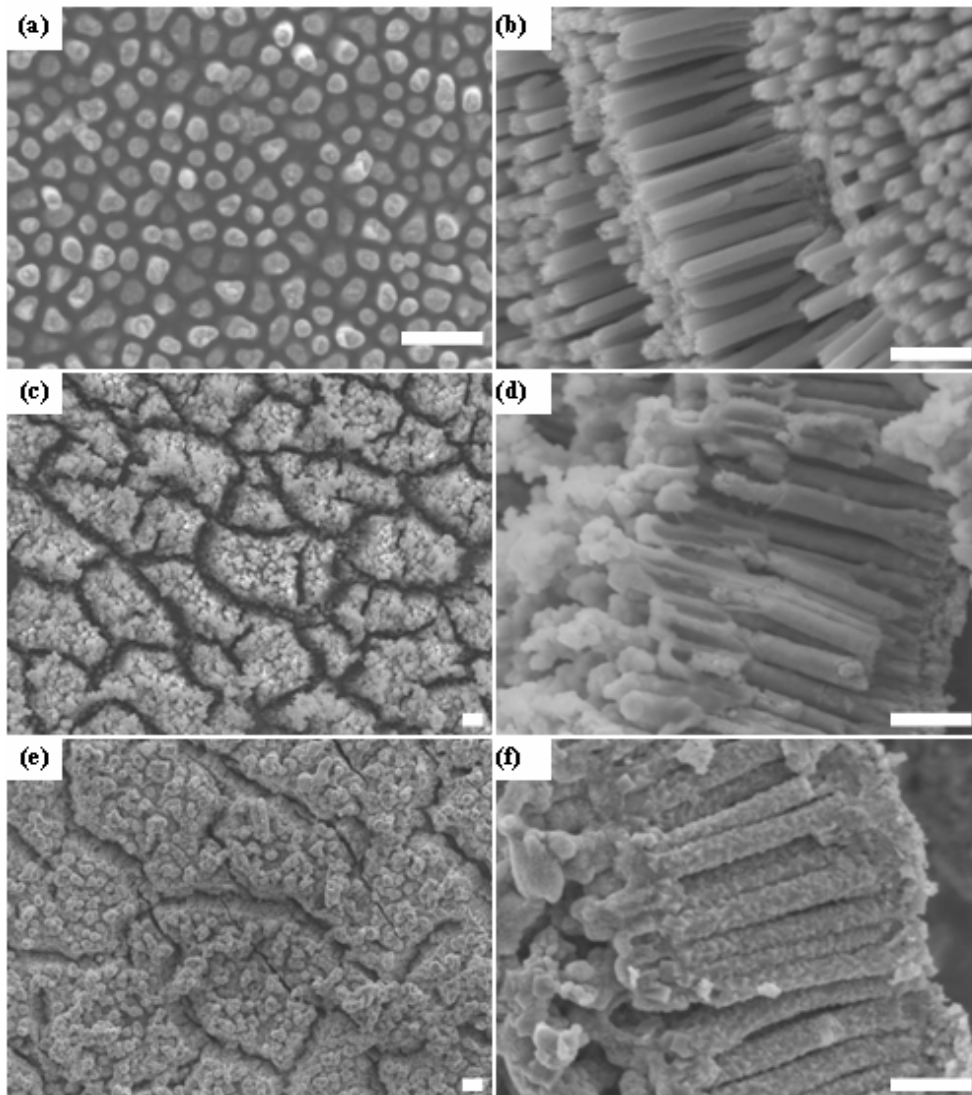

Fig. 4 SEM images of Cu nanorods before (a) (b), after (c) (d) titanium hydroxide gel deposition, and after heat treatment (e) (f). Scale bars: (a) - (f) 1 μm.

XRD was used to characterize the microstructure of the as-fabricated electrodes. Fig. 5 displays typical XRD patterns of TiO_2 deposited on polished Cu foil and on Cu NR arrays. The XRD pattern of Cu foil without TiO_2 deposits is also presented for comparison. Fig. 5 suggests that for (b) and (c), in addition to the Cu peaks from the substrate and TiO_2 peaks from the TiO_2 deposits, there are also peaks for the phase of Cu_2O which probably formed during the heat treatment. Moreover, the intensities of the TiO_2 peaks near 25.29 and 48.05 increased when the substrate was changed from polished Cu foil to the Cu NR arrays, which implies greater load of TiO_2 for the nanostructured electrode. While the intensities of the Cu_2O peaks near 29.56, 36.42, 42.30, and 61.35 were negligible for planar Cu foil with TiO_2 deposits, suggesting minimal oxidation of the sample during heat treatment.
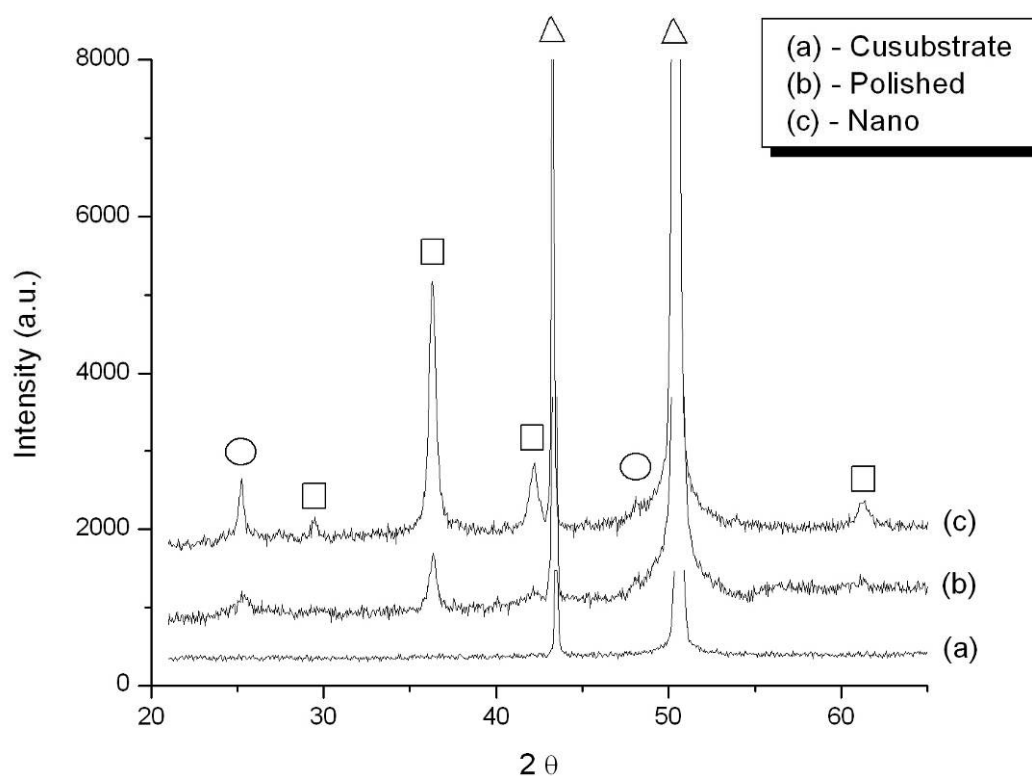

Fig. 5 XRD patterns for TiO_2-based electrodes: Cu foil without TiO_2 deposition (a), polished planar Cu foil with TiO_2 deposits (b), and Cu NR arrays with TiO_2 deposits (c). Note: sphere – TiO_2, square – Cu_2O, triangle – Cu.

The capacity and rate capability of the electrode were tested by galvanostatic charge/discharge tests. Fig. 6 displays the initial discharge curves of the nanostructured and planar electrode with unpolished Cu foil at the current rate of 25 mA g^{-1}. Both samples give

similar voltage-capacity curves with, during the first discharge, the capacity of the nanostructured electrode more than two times that of the planar Cu electrode, 650 mAh g^{-1} vs 250 mAh g^{-1}. This can be attributed to the greater amount of the active materials on the nanostructured electrode with Cu NRs compared to its planar counterparts. However, these discharge curves don't demonstrate clear potential plateaus at/near 1.75 V for discharging which are characteristic of Li insertion into anatase [21-23]. Instead, they exhibited more of the characteristics of copper oxide using as electrode for Li ion batteries [24-27].   Followed by an abrupt drop in the potential down to 1.25 V, there is a pseudo-plateau in the voltage range of 1.25 to 0.5 V. below 0.5 V, the potential tends to decrease gradually as the discharge depth increases.
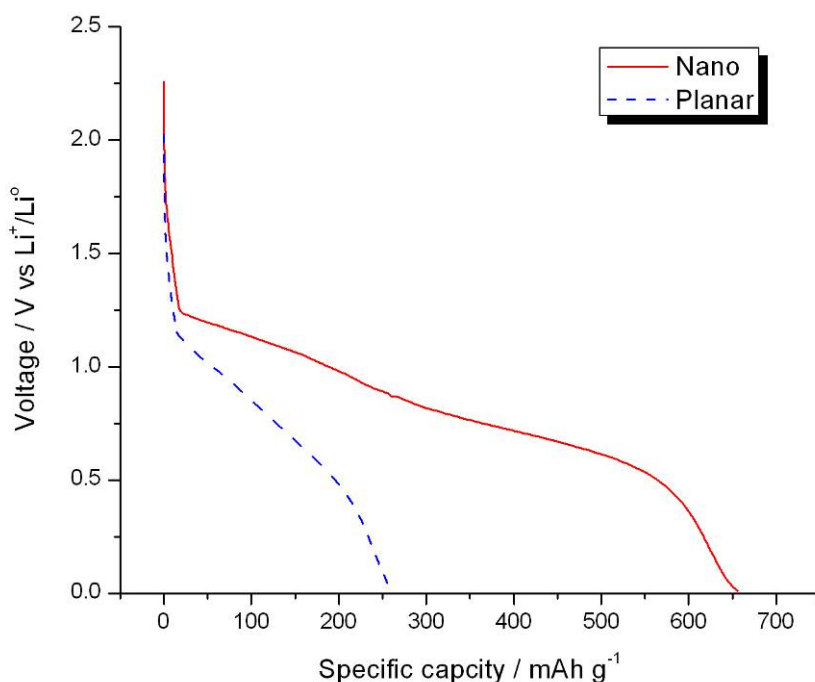

Fig. 6 Potential-capacity profiles of the nanostructured electrode and the planar electrode galvanostatically cycled versus Li for the first cycle.

Fig. 7 compares the cycle performance of the three types of electrodes. For the first two cycles, a current rate of 25 mA g^{-1} was used, and the current rate was increased to 50 mA g^{-1} for the following cycle. Obviously, the nanostructured electrode demonstrates higher capacity per unit electrode area than the polished and unpolished planar Cu electrodes, which is consistent with the potential-capacity results in Fig. 6, and there is slight difference between

the latter two in terms of capacity. Fig. 7 also shows that all the capacity decayed fast with the cycling, which is not expected for an anatase-based electrode for Li ion batteries. [21,28,29] For the nanostrucutred electrode in particular, its capacity decays from 350 mAh g^{-1} on the first cycle to 184 mAh g^{-1} on the second one and to about 100 mAh g^{-1} on the eighth cycle. Clearly, the introduction of copper oxide in the heat treatment is affecting the rate capability of the electrodes. More work is in progress to optimize the nanostructured electrodes to improve the rate capability and test the electrode life time through large number of cycle tests.
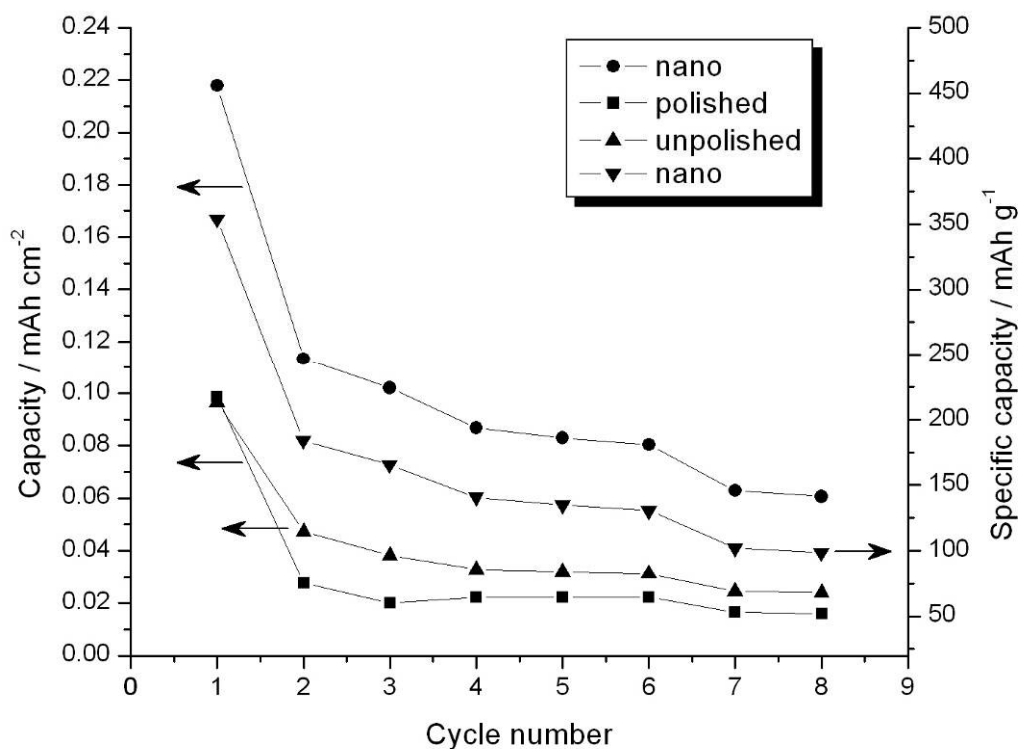

Fig. 7 Comparison of the cycle performance of TiO_2-based electrodes on different substrates.

CONCLUSIONS

A novel design of TiO_2-based nanoengineered electrodes for Li ion batteries was proposed. The nanostructured electrodes were manufactured by adopting two-step process consisting of the template-assisted growth of Cu nanorods onto Cu foils as nanostructured current collectors and the electrodeposition of TiO_2. The TiO_2 was also deposited on polished and unpolished planar Cu substrates for comparison. SEM results show that each of the Cu

nanorod has been covered with a dense layer of TiO_2 thin film. XRD is used to confirm the crystalline TiO_2 phase and the XRD results show that larger amount of TiO_2 was deposited with the introduction of Cu nanorods, which is favorable to gain a high specific capacity. However, higher degree of oxidation was also occurred for the nanostructured electrodes, which will affect Li ion insertion mechanism and the rate capability.

ACKNOWLEDGMENTS

REFERENCES

[1] P.G. Bruce, B. Scrosati, and J.M. Tarascon, Angew. Chem. Int. Ed. **47,** 2930 (2008).

[2] J. Li, Z. Tang, and Z. Zhang, Electrochem. Comm. **7,** 62 (2005).

[3] P.G. Bruce, Chem. Commun. **19,** 1817 (1997).

[4] V. Subramanian, A. Karki, K.I. Gnanasekar, F.P. Eddy and B. Rambabu, J. Power Sources **159,** 186 (2006).

[5] M. Hibino, K. Abe, M. Mochizuki and M. Miyayama, J. Power Sources **126,** 139 (2004).

[6] M. Wagemaker, A.P.M. Kentgens and F.M. Mulder, Nature **418,** 397 (2002).

[7] Y.K. Zhou, L. Cao, F. B. Zhang and H.L. Li, J. Electrochemical Society **150,** A1246 (2003).

[8] A. Guerfi, P. Charest, K. Kinoshita, M. Perrier and K. Zaghib, J. Power Sources **126,** 163 (2004).

[9] A.R. Armstrong, G. Armstrong, J. Canales and P.G. Bruce, J. Power Sources **146,** 501 (2005).

[10] J.O. Besenhard, J. Yang, and M. Winter, J. Power Sources **68,** 87 (1997).

[11] H. Duan, J. Gnanaraj, X. Chen, B. Li, and J. Liang, J. Power Sources **185,** 512 (2008).

[12] J.S. Gnanaraj, J.F. DiCarlo, H. Duan, J. Liang, R.W. Thompson, 10th Power Source R&D Symposium, Williamsburg, VA, 2007.

[13] X. Chen, H. Duan, Z. Zhou, J. Liang, J. Gnanaraj, Nanotechnology **19,** 365306 (2008).

[14] S. Karuppuchamy, K. Nonomura, T. Yoshida, T. Sugiura, and H. Minoura, Solid State Ionics **151,** 19 (2002).

[15] B.R. Sankapal, S.D Sartale, M.C. Lux-Steiner, and A. Ennaoui, C.R. Chimie **9,** 702 (2006).

[16] J. Georgieva, S. Armyanov, E. Valova, I. Poulios, S. Sotiropoulos, Electrochem. Acta. **51,**

2076 (2006).

[17] I. Zhitomirski, L. Gal-Or, A. Khon and M.D. Spang, J. Mater. Sci. **32**, 803 (1997).

[18] I. Zhitomirski and L. Gal-Or, J. Eur. Ceram. Soc. **16**, 819 (1996).

[19] J. Liang, H. Chik, and J. Xu, IEEE J. Sel. Top. Quantum Electron. **8**, 998 (2002).

[20] H. Chik, J. Liang, S.G. Cloutier, N. Koukli, and J.M. Xu, Appl. Phys. Lett. **84**, 3376 (2004).

[21] X. Gao, H. Zhu, G. Pan, S. Ye, Y. Lan, F. Wu, and D. Song. J. Phys. Chem. B **108**, 2868 (2004).

[22] S.Y. Huang, L. Kavan, I. Exnar and M. Gratzel, J. Electrochem. Soc. **142**, L142 (1995).

[23] F. Bonino, L. Busani, M. Lazzari, M. Manstretta, B. Rivolta and B.Scrosati, J. Power Sources **6**, 261 (1981).

[24] S. Grugeon, S. Laruelle, R. Herrera-Urbina, L. Dupont, P. Poizot, and J-M. Tarascon, J. Electrochem. Soc. **148**, A285 (2001).

[25] J. Morales, L. Sanchez, F. Martin, J.R. Ramos-Barrado and M. Sanchez. Thin Solid Films **474**, 133 (2005).

[26] X. P. Gao, J. L. Bao, G. L. Pan, H. Y. Zhu, P. X. Huang, F. Wu and D. Y. Song. J. Phys. Chem. B **108**, 5547 (2004).

[27] X. Zhang, D. Zhang, X. Ni, J. Song and H. Zheng. J. Nanopart. Res. **10**, 839 (2008).

[28] H. Furukawa, M. Hibino and I. Honma. J. Electrochem. Soc. **151**, A527 (2004).

[29] V. Subramanian, A. Karki, K.I. Gnanasekar, F.P. Eddy and B. Rambabu. J. Power Sources **159**, 186 (2006).